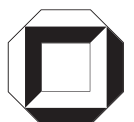


Dissertationsreihe am Institut für Hydromechanik  
der Universität Karlsruhe (TH)  
Heft 2005/4

# Gas Transfer at the Air-Water Interface in a Turbulent Flow Environment

Herlina





Herlina

**Gas Transfer at the Air-Water Interface  
in a Turbulent Flow Environment**

Dissertationsreihe am Institut für Hydromechanik  
der Universität Karlsruhe (TH)  
Heft 2005/4

# **Gas Transfer at the Air-Water Interface in a Turbulent Flow Environment**

von  
Herlina



---

universitätsverlag karlsruhe

Dissertation, genehmigt von der  
Fakultät für Bauingenieur-, Geo- und Umweltwissenschaften  
der Universität Fridericiana zu Karlsruhe (TH), 2005  
Referenten: Prof. Gerhard H. Jirka, Ph.D.  
Prof.em. Dr.-Ing. Dr.-Ing. E.h. Erich J. Plate  
Prof. Dr. Bernd Jähne

## **Impressum**

Universitätsverlag Karlsruhe  
c/o Universitätsbibliothek  
Straße am Forum 2  
D-76131 Karlsruhe  
www.uvka.de



Dieses Werk ist unter folgender Creative Commons-Lizenz  
lizenziert: <http://creativecommons.org/licenses/by-nc-nd/2.0/de/>

Universitätsverlag Karlsruhe 2005  
Print on Demand

ISSN 1439-4111  
ISBN 3-937300-74-0

# Gas Transfer at the Air-Water Interface in a Turbulent Flow Environment

Zur Erlangung des akademischen Grades eines

DOKTOR-INGENIEURS

von der Fakultät für Bauingenieur-, Geo- und Umweltwissenschaften  
der Universität Fridericiana zu Karlsruhe (TH)

genehmigte

DISSERTATION

von

Herlina, M.Eng.

aus Jakarta, Indonesien

Tag der mündlichen Prüfung: 6. Juli 2005

Hauptreferent: Prof. Gerhard H. Jirka, Ph.D.

Korreferent: Prof.em. Dr.-Ing. Dr.-Ing. E.h. Erich J. Plate

Korreferent: Prof. Dr. Bernd Jähne

Karlsruhe 2005





# Gas Transfer at the Air-Water Interface in a Turbulent Flow Environment

## Abstract

The gas transfer process across the air-water interface in a bottom-shear-induced turbulent environment was investigated to gain improved fundamental understanding of the physical mechanisms that control the process. For this purpose, it is necessary to reveal the hydrodynamics of the flow field as well as the molecular diffusion and the turbulent transport contributions to the total flux. Therefore, detailed laboratory experiments were conducted to obtain these information.

The experiments were performed in a grid-stirred tank using a combined Particle Image Velocimetry - Laser Induced Fluorescence (PIV-LIF) technique that has been developed for these near surface gas transfer measurements. The turbulence characteristics of the velocity near the interface were acquired from the PIV measurements and showed generally good agreement with the theoretical profiles from Hunt & Graham (1978). The LIF technique enabled visualization of the planar concentration fields which provided more insight into the gas transfer mechanisms. The high data resolution allowed detailed quantification of the concentration distribution within the thin aqueous boundary layer. The mean and turbulent fluctuation characteristics of the concentration could be elucidated and the molecular diffusion contribution to the total flux across the interface could be determined. With the combined PIV-LIF technique, which enables simultaneous and spatially synoptic measurements of 2D velocity and concentration fields, the turbulent mass flux term  $cw$  and also the total mass flux across the air-water interface could be quantified directly. For the first time, a particular trend can be inferred from the measured mean  $cw$  profiles. It could also be shown that the contribution of the turbulent mass flux to the total gas flux is significant. The co-spectra indicated different behavior for the cases with lower and higher turbulent Reynolds numbers.

The interrelated interpretation of the obtained results suggest that the gas transfer process is controlled by a spectrum of different eddy sizes and the gas transfer at different turbulence levels can be associated to certain eddy sizes. For high turbulence levels the gas transfer should be asymptotic to the small eddy model, whereas for low turbulence level to the large eddy model. The new results of turbulent mass flux should aid as an excellent database in refining numerical models and developing more accurate models for the prediction of the transfer velocity.



# Gasaustausch an der Grenzfläche Wasser-Luft eines turbulenten Wasserkörpers

## Kurzfassung

Der Gasaustausch an der Grenzfläche Wasser-Luft ist ein wichtiges Prozesselement, insbesondere für die Aufrechterhaltung der Wasserqualität in fließenden und stehenden Gewässern, als auch für die Geophysik in Bezug auf globale und regionale geochemische Stoffkreisläufe mit spezieller Relevanz für Treibhausgase wie Kohlendioxyd.

Um die physikalischen Mechanismen zum Gasaustauschprozess an der Grenzfläche Wasser-Luft detailliert zu analysieren und zu quantifizieren, wurden Experimente in einem, durch oszillierende Gitter angeregten, turbulenten Wasserkörper durchgeführt. Für diese Zielsetzung, ist es notwendig die Hydrodynamik sowie den Massenfluss durch molekulare Diffusion und turbulenten Transport zu erfassen.

Die Experimente wurden in einem Rüttelgittertank mittels kombinierter Particle-Image-Velocimetry und Laser-Induced-Fluorescence (PIV-LIF) Technik durchgeführt, welche speziell für die Messung des Gasaustausch nahe der Oberfläche entwickelt wurde. Die Turbulenzcharakteristik nahe der Oberfläche wurde durch PIV Messungen ermittelt und zeigte gute Übereinstimmung mit dem theoretisch ermittelten Profil von Hunt & Graham (1978). Die LIF-Technik ermöglicht die Visualisierung von Konzentrationsfeldern, und damit einen guten Einblick in den Mechanismus des Gasaustauschs. Durch die hohe Auflösung der LIF ist es möglich den Konzentrationsverlauf innerhalb der dünnen Grenzschicht (100-1000  $\mu\text{m}$ ) zu erfassen. Auf diese Weise wurden die mittleren Konzentrationsfelder sowie die Schwankungsgrößen des Konzentrationsverlaufs ermittelt, was die Berechnung des Beitrags der molekularen Diffusion zum Gesamtmassenfluss ermöglicht. Unter Verwendung der kombinierten PIV-LIF Technik, welche die simultane Messung planarer Konzentrations- und Geschwindigkeitsfelder ermöglicht, können der turbulente sowie der Gesamtmassenfluss direkt quantifiziert werden. Erstmals, konnte ein bestimmter Trend für den gemessenen Massenflussprofil ermittelt werden. Es konnte auch gezeigt werden dass der Beitrag des turbulenten Massenfluss zum Gesamtmassenfluss signifikant ist. Die Kreuzkorrelationsspektren der Geschwindigkeits- und Konzentrationsschwankungen zeigten verschiedene Verhältnisse für hohe und niedrige Turbulenzintensitäten.

Die Interpretation der Ergebnisse deuten darauf hin, dass der Gasaustauschprozess von einem breiten Spektrum verschiedener Wirbelgrößen kontrolliert wird und, dass der Prozess mit verschiedenen Turbulenzintensitäten zu bestimmten Wirbelgrößen zugeordnet werden kann. Für große Turbulenzintensitäten sollte der Gasaustauschprozess sich

asymptotisch dem Kleinwirbelmodell Lamont & Scott (1970) annähern, während für niedrigere Turbulenzintensitäten das Großwirbelmodell Fortescue & Pearson (1967) passen sollte. Die neuen Ergebnisse des turbulenten Massenflusses stellen eine verlässliche Datenbasis für numerische Simulationen zur Verfügung ermöglichen die Entwicklung neuer bzw. verbesserter Modelle zur Vorhersage der Gasaustauschraten.

# Acknowledgements

I would like to express my sincere gratitude and appreciation to my advisor, Professor Gerhard H. Jirka, for his guidance, encouragement and support during my research. I also wish to thank my co-referees Professor Bernd Jähne and Emeritus Professor Erich J. Plate, for their valuable advice.

I wish to thank all my colleagues at the Institute for Hydromechanics for their support during my work. In particular, I am very grateful to Dr-Ing. Volker Weitbrecht for his constructive discussion, Gregor Kühn for his help in the establishment of the experimental setup, Tobias Bleninger, Meike Bücken-Gittel and Hanne Mayer for their support. I'm also grateful for their friendship that have made my study in Karlsruhe a lot more cheerful and enjoyable. I would also like to express my gratitude to Dr-Ing. Cornelia Lang for her support and advices both in academic as well as administration matters, especially during the first year of my study. Last but not least, I also wish to appreciate the aid of fellow students which are involved in this research.

I am deeply grateful to my parents, my husband Ikhwan, my children Fahrie and Taqiya for their loving support and constant encouragement throughout the time that this work was in progress. I am also indebted to Arifah and her family for looking after my son.

The financial support from the "Deutsche Forschungsgemeinschaft" (DFG) for funding this project through project grant No. Ji 18/7 is gratefully acknowledged.



# Contents

<b>1. Introduction</b> .....	1
1.1 Background .....	1
1.2 Scope and Objective .....	2
1.3 Methodology .....	5
1.4 Outline .....	6
<b>2. Literature Review</b> .....	8
2.1 Fundamental concepts .....	8
2.1.1 Governing equations .....	8
2.1.2 Transfer velocity $K_L$ .....	9
2.1.3 Liquid-side resistance .....	10
2.2 Gas transfer models .....	10
2.2.1 Conceptual models .....	11
2.2.2 Hydrodynamic models .....	13
2.2.3 Eddy diffusivity models .....	14
2.3 Review of gas transfer studies .....	15
2.3.1 Buoyant-convective-induced turbulence .....	15
2.3.2 Wind-shear-induced turbulence .....	15
2.3.3 Bottom-shear-induced turbulence .....	16
2.3.4 Combined wind-shear and bottom-shear-induced turbulence .....	20
2.3.5 Film-free and film-covered interfaces .....	21
2.4 Investigations on grid-stirred turbulence .....	22
2.5 Eddy-correlation method .....	26
<b>3. Experimental Setup, Measurement Techniques and Program</b> .....	27
3.1 Experimental setup .....	27
3.2 Measurement techniques .....	29
3.2.1 Particle Image Velocimetry (PIV) .....	30
3.2.2 Laser Induced Fluorescence (LIF) .....	33
3.2.3 Bulk concentration measurements .....	38

3.3	Image Processing (LIF interpretation) .....	38
3.4	Verification of the LIF setup and image processing .....	41
3.5	Experimental Program and Procedure .....	42
3.5.1	Velocity measurements in the bulk (Vb-series) .....	43
3.5.2	Concentration measurements near the interface (C-series) .....	46
3.5.3	Simultaneous concentration and velocity measurements (CV-series) ..	48
3.5.4	Bulk concentration measurements (Cb-series) .....	50
<b>4.</b>	<b>Evaluation of turbulence characteristics in the present grid-stirred tank</b>	<b>52</b>
4.1	Velocity fluctuations .....	52
4.2	Integral length scales .....	58
4.3	Turbulent kinetic energy .....	60
4.4	Spectra .....	61
4.5	Summary of evaluation .....	65
<b>5.</b>	<b>Results and Discussion</b> .....	<b>67</b>
5.1	Qualitative observations of instantaneous concentration fields .....	67
5.2	Quantitative results : Mean and turbulence characteristics of concentration	73
5.2.1	Mean and fluctuation profiles .....	73
5.2.2	Boundary layer thickness .....	78
5.2.3	Normalized mean profiles .....	84
5.2.4	Normalized fluctuation profiles .....	86
5.3	Velocity fluctuations near the interface .....	90
5.4	Oxygen transfer velocity ( $K_L$ ) .....	93
5.5	Turbulent mass flux .....	97
5.5.1	Instantaneous turbulent mass flux .....	97
5.5.2	Mean profile of turbulent mass flux .....	103
5.6	Total mean flux .....	105
5.7	Spectra .....	106
5.7.1	Spectra of near surface velocity fluctuation .....	106
5.7.2	Spectra of concentration fluctuation .....	111
5.7.3	Co-spectra of velocity fluctuation and concentration fluctuation .....	111
5.8	Implications of the present results on mechanisms and models of gas transfer	116
5.8.1	Dominant eddy size .....	116
5.8.2	Contribution of the turbulent mass flux .....	117
<b>6.</b>	<b>Conclusions and Recommendations</b> .....	<b>119</b>
6.1	Conclusions .....	119



6.2 Recommendations for further studies ..... 123

**References** ..... 124

# List of Figures

1.1	Schematic illustration of the dominant turbulence generation mechanisms driving interfacial gas transfer in the water environment. Type <b>C</b> represents the source of turbulence that is investigated in this study. ....	3
1.2	Schematic diagram of gas transfer process near the interface enhanced by bottom-shear-induced turbulence. a) depicts the turbulence generated at the bottom which diffuses towards the interface; b) depicts the oxygen transfer process at the interface with its limited boundary layer at the water side. .	4
2.1	Schematic illustration showing estimation of hydrodynamic layers (Brumley and Jirka, 1988), with $\eta$ is the Kolmogorov sublayer and $Sc$ the Schmidt number. The parameters $L_\infty$ and $Re_T$ are the integral length scale and the turbulent Reynolds number, respectively, which definition's are explained in Section 2.4. ....	18
3.1	Grid-stirred tank : (a) schematic illustration of the tank with coordinate system, (b) photograph showing the tank equipped with the oscillating grid .....	28
3.2	Principle of PIV technique .....	30
3.3	Experimental setup showing the configuration of the tank and PIV system .....	32
3.4	Experimental setup showing configuration of tank and LIF system .....	36
3.5	Absorption and fluorescence spectra of PBA (Vaughan and Weber, 1970).....	37
3.6	Example of a vertical intensity profile from a raw image.....	39
3.7	Example of vertical intensity profile after filtering .....	39
3.8	Example of vertical intensity profile after rearranged to the reference level where $z = 0$ is the detected water surface .....	40
3.9	Example of a vertical intensity profile after the Lambert-Beer and optical blurring effect corrections ..	40
3.10	Example of a vertical intensity profile after converted into concentration .....	41
3.11	Relation of fluorescence intensity measured with the CCD camera to the absolute oxygen concentration measured with the oxygen probe. The fluorescence intensity is represented in a normalized form $F/F_o$ in which $F_o$ is the intensity when no oxygen is present .....	42
3.12	Schematic illustration of the experimental setup in the Vb-series .....	44
3.13	Plan view of the camera positions in the Vb-series.....	45
3.14	Schematic illustration of the experimental setup in the C-series .....	47
3.15	Schematic illustration of the experimental setup in the CV-series .....	49
3.16	Schematic illustration of the experimental setup in the Cb-series .....	50
4.1	Coordinate convention used for the discussion of the bulk turbulence measurements .....	53
4.2	Example of two successive instantaneous vector fields (selected from Vb5) .....	53
4.3	Distribution of velocity fluctuation at selected elevations from Vb4. (a) horizontal fluctuations (b) vertical fluctuations .....	55
4.4	Temporally and spatially averaged turbulence velocities showing the decay of turbulence intensity with distance from the grid as a function of different turbulence conditions. (a) horizontal components $u'$ (b) vertical components $w'$ .....	56
4.5	Temporally and spatially averaged turbulence velocities at the centre and near the side wall of the tank. (a)horizontal fluctuations $u'$ ; and (b)vertical fluctuations $w'$ .....	57
4.6	Correlation-coefficients as a function of $\zeta$ at selected $z_{cs}$ levels from Exp. Vb4 : (a)longitudinal (b)transversal .....	58

4.7	Variation of the longitudinal and transversal integral length scales of the velocity fluctuations with distance from the centre of the grid. . . . .	59
4.8	Variation of the longitudinal and transversal integral length scales of the velocity fluctuations with distance from the centre of the grid. . . . .	60
4.9	Measured turbulent kinetic energy $k$ . . . . .	62
4.10	Spectra of velocity fluctuations at different $z_{cs}$ levels for $Re_T = 260$ , water surface is at $z_{cs} = 280$ mm. (a) horizontal component; and (b) vertical component . . . . .	63
4.11	Spectra of velocity fluctuations at different $z_{cs}$ levels for $Re_T = 780$ , water surface is at $z_{cs} = 280$ mm. (a) horizontal component; and (b) vertical component . . . . .	64
5.1	Schematic illustration of the coordinate system used in discussing the results of the gas transfer measurements . . . . .	68
5.2	A sequence of oxygen concentration contour maps visualizing a peeling process associated to a surface renewal event, $z = 0$ is the water surface, time interval between shown images is 0.25 s. . . . .	69
5.3	A sequence of oxygen concentration contour maps visualizing a small eddy structure approaching the boundary, $z = 0$ is the water surface, time interval between shown images is 0.75 s. . . . .	70
5.4	Typical instantaneous image with no grid movements . . . . .	71
5.5	Instantaneous concentration profiles measured with $Re_T = 780$ (C5) extracted from Figure 5.2 at $x = 248$ mm which is approximately at the centre of the recorded image. . . . .	72
5.6	Illustration of the LIF area used in the statistical analysis . . . . .	74
5.7	Mean concentration profiles obtained from (a) the stand-alone LIF measurements (C-series) and (b) the simultaneous PIV-LIF measurements (CV-series). Only every seventh data point is shown in the graph to avoid congestion. . . . .	75
5.8	Concentration fluctuation profiles, data obtained with (a) stand-alone LIF (C-series) and (b) simultaneous PIV-LIF (CV-series) Only every seventh data point is shown in the graph to avoid congestion. The unconnected data points extremely close to the surface are data points that are probably biased due to the optical blurring correction procedure in the image processing. . . . .	76
5.9	Comparison of concentration profiles obtained using the stand-alone LIF and the simultaneous PIV-LIF for $Re_T = 380$ . (a) mean profiles (b) fluctuation profiles. Only every seventh data point is shown for clarity. . . . .	77
5.10	Illustration of the boundary layer thickness defined based on the steepest gradient at the water surface ( $\delta_g$ ) . . . . .	79
5.11	Instantaneous concentration images and the boundary layer, showing the boundary layer thickness variation in space and time . . . . .	79
5.12	Time-series of local boundary layer thickness. (a) $Re_T = 260$ and (b) with $Re_T = 780$ . The magnitude of the boundary layer thickness is smaller when the turbulence intensity is higher. . . . .	80
5.13	Measured boundary layer thickness . . . . .	81
5.14	Measured boundary layer thickness $\delta_e$ plotted against the square root of the interfacial turbulent kinetic energy $\sqrt{k_s}$ . . . . .	82
5.15	Outer diffusive sublayer vs boundary layer thickness . . . . .	83
5.16	Normalized mean concentration profiles plotted against the depth normalized with $\delta_e$ . Only every seventh data point is shown in the graph to avoid congestion. . . . .	85
5.17	Normalized mean concentration profiles with stand-alone LIF and with simultaneous PIV-LIF. Only every seventh data point is shown in the graph to avoid congestion. . . . .	87
5.18	Normalized fluctuation concentration profiles. Only every seventh data point is shown in the graph to avoid congestion. The unconnected data points extremely close to the surface are data points that are probably biased due to the optical blurring correction procedure in the image processing. . . . .	88
5.19	Turbulence fluctuations near the interface (from CV-series) (a) horizontal fluctuation (b) vertical fluctuation . . . . .	91
5.20	Normalized turbulence fluctuations near the interface (from CV-series) (a) horizontal fluctuation (b) vertical fluctuation . . . . .	92
5.21	Bulk concentration measurements (Cb-series) : Time histories of oxygen concentration as well as temperature in the bulk region for all five grid conditions . . . . .	94
5.22	Bulk measurement in the form of Eq. 5.14 to determine the reaeration coefficient, $K_2$ . . . . .	95

VI List of Figures

5.23 Variation of the normalized transfer velocity  $K_L$  with the turbulent Reynolds number  $Re_T$  . . . . . 96

5.24 Sequence of oxygen contour map and vector map from the simultaneous PIV-LIF measurements, taken from CV2. The shown sequence was taken within 3.5 seconds and the time interval between the shown is 0.5 s. . . . . 98

5.25 Sequence of oxygen contour map and vector map from the simultaneous PIV-LIF measurements, taken from CV3. The shown sequence was taken within 3.5 seconds and the time interval between the shown is 0.5 s. . . . . 99

5.26 Time history of the simultaneously measured  $c$  and  $w$  and their normalized cross-correlation at selected points with  $Re_T = 260$  (CV1) (a)  $x = 253.7$  mm,  $z = 0.5$  mm (b)  $x = 253.7$  mm,  $z = 4.2$ mm. . . . . 101

5.27 Time history of the simultaneously measured  $c$  and  $w$  and their normalized cross-correlation at selected points with  $Re_T = 780$  (CV5) (a)  $x = 253.7$  mm,  $z = 0.5$  mm (b)  $x = 253.7$  mm,  $z = 4.2$ mm. . . . . 102

5.28 Variation of measured turbulent mass flux (a)with depth and (b) with normalized depth . . . . . 104

5.29 Variation of measured molecular diffusive transport, turbulent mass flux and the resulting total mass flux with depth. All values are normalized with the absolute total mean flux  $\bar{j}$  (as listed in Table 5.3) determined from the bulk measurements. . . . . 107

5.30 Spectra of near surface velocity fluctuation for  $Re_T = 260$ . (a) horizontal component; and (b) vertical component . . . . . 108

5.31 Spectra of near surface velocity fluctuation for  $Re_T = 390$ . (a) horizontal component; and (b) vertical component . . . . . 108

5.32 Spectra of near surface velocity fluctuation for  $Re_T = 520$ . (a) horizontal component; and (b) vertical component . . . . . 109

5.33 Spectra of near surface velocity fluctuation for  $Re_T = 650$ . (a) horizontal component; and (b) vertical component . . . . . 109

5.34 Spectra of near surface velocity fluctuation for  $Re_T = 780$ . (a) horizontal component; and (b) vertical component . . . . . 110

5.35 Spectra of concentration fluctuation  $c$ . . . . . 112

5.36 Spectra of turbulent mass flux  $cw$  . . . . . 114

5.37 Spectra of vertical velocity fluctuations, concentration fluctuations and turbulent mass flux at approximately  $z/\delta_e = 1$  . . . . . 115

# List of Tables

2.1	Variation of the coefficients in Eqs. 2.14 and 2.15(source : Asher & Pankow (1986) . . . . .	22
3.1	Typical experimental parameters for the gas transfer measurements (C-series, CV-series, and Cb-series). For the calculation of $Re_T$ , the viscosity $\nu$ was taken as the viscosity at the reference temperature $20^\circ\text{C}$ . . . . .	43
3.2	Experimental parameters for the Vb-Series . . . . .	43
3.3	Experimental conditions in the C-Series . . . . .	46
3.4	Estimated hydrodynamic thickness (in mm) based on Brumley and Jirka (1987) . . . . .	47
3.5	Experimental conditions in the CV-Series . . . . .	49
3.6	Experimental conditions in the Cb-Series . . . . .	51
5.1	Measured boundary layer thickness . . . . .	81
5.2	$K_L$ values with varying turbulence intensities. $K_{L,t}$ is the absolute transfer velocity coefficient determined from the bulk measurement. $K_{L,\delta_e} = D/\delta_e$ is the estimated transfer velocity using the film model . . . . .	96
5.3	Total mean flux values determined from the bulk measurements( $\bar{j} = K_L(C_s - C_b)$ ) . . . . .	100

# List of Symbols

$C$	instantaneous oxygen concentration
$C_b$	oxygen concentration in the bulk region
$C_{orr}$	cross-correlation function
$C_s$	saturated oxygen concentration
$c$	fluctuation component of concentration
$\bar{c}$	mean component of concentration
$c'$	root mean square of concentration fluctuation
$D$	molecular diffusivity
$D_t$	turbulent diffusivity
$E_c$	spectrum of concentration fluctuation
$E_{cw}$	co-spectrum of concentration and velocity
$E_T$	total diffusivity
$E_u$	spectrum of horizontal velocity fluctuation
$E_w$	spectrum of vertical velocity fluctuation
$F$	fluorescence intensity
$f$	frequency of grid oscillation
$F_b$	fluorescence intensity in the bulk region
$F_i$	fluorescence intensity at the interface
$f_s$	sampling frequency
$h, H$	water depth
$H_c$	Henry's constant
$I$	image intensity
$j$	gas flux
$k$	turbulent kinetic energy
$k_d$	sum of rates of radiationless deactivation
$k_f$	rate of light emission
$k_g$	gas transfer coefficient for the gas phase
$k_L$	gas transfer coefficient for the liquid phase
$K_L$	gas transfer coefficient, transfer velocity
$L$	turbulent integral length scale
$L_\infty$	far-field integral length scale
$L_u$	longitudinal integral length scale
$L_w$	transversal integral length scale
$M$	mesh spacing, mesh size of grid
$p$	pressure
$Q$	quencher concentration
$R$	cross-correlation functions
$r$	renewal rate
$R_u/R_w$	auto correlation functions
$R_{uu,x}$	longitudinal cross-correlation coefficient
$R_{ww,x}$	transversal cross-correlation coefficient
$Re_T$	turbulent Reynolds number
$S$	stroke or amplitude of the grid oscillation
$Sc$	Schmidt number ( $Sc = \nu/D$ )

$T$	renewal time, temperature
$t$	time
$U, V, W$	instantaneous velocity in x,y,z direction, respectively
$u, v, w$	fluctuation component of velocity in x,y,z direction, respectively
$\bar{u}, \bar{v}, \bar{w}$	mean component of velocity in x,y,z direction, respectively
$u', v', w'$	root mean square of velocity fluctuation in x,y,z direction, respectively
$u'_{\infty}$	far-field velocity fluctuations
$u_*$	bottom shear velocity
$u_*\alpha$	characteristic velocity scale
$z$	depth from the water surface
$z_{cs}$	distance from a virtual origin towards the water surface
$z_s$	distance from the center of grid to the water surface
$\delta$	boundary layer thickness
$\epsilon$	turbulent energy dissipation rate
$\nu$	kinematic viscosity of water
$\tau$	lifetime of an excited molecule
$\zeta_x$	distance of the lags in x-direction





# 1. Introduction

## 1.1 Background

Gas transfer across the air-water interface plays an important role in geophysical processes and in environmental engineering. The problem areas range from natural geochemical cycling of materials to anthropogenic water quality (e.g. reaeration) problems in rivers, lakes and coastal waters to applications in industrial facilities. Volatilization, stripping, absorption, and aeration are terms that are often used to describe the transfer of chemicals across the gas-liquid phase. Volatilization and stripping refer to the transfer of gas toward the air phase whereas absorption and aeration toward the liquid phase. Absorption is generally used in reference to the mitigation of soil and groundwater pollution and the transfer of global warming gases such as PCB's and PAH's across the surface of oceans and large lakes (Gulliver (1990)). Aeration and reaeration are common terms referring to the oxygen transfer into water bodies.

Examples of gas transfer processes widely applied in man-made facilities include stripping of  $H_2S$  in drinking water treatment to remove taste and odor, stripping of carbon dioxide ( $CO_2$ ) from some ground waters as well as from industrial process waters and absorption of oxygen ( $O_2$ ) into treated water in wastewater treatment plants.

The importance of gas transfer in nature has recently been highlighted by the ocean's role for being the largest sink of fossil fuel-produced  $CO_2$  by taking up 30-40 % of the  $CO_2$  (Donelan & Wanninkhof (2002)). Another important gas transfer process in nature is the oxygen absorption into natural water bodies. Oxygen is a fundamental parameter for natural water bodies to sustain aquatic life and to take up organic pollutant loadings. This reaeration process is thus, very critical to the aquatic habitat because it recovers the deficit of dissolved oxygen in polluted rivers, lakes and estuaries. The given examples show that improved knowledge of the gas transfer process across the air-water interface is an essential factor for the water quality assessment and management.

The flow conditions in nature are typically turbulent and it is well known that turbulence plays an important role in the gas transfer process besides molecular diffusion. The turbulent eddies and their related vorticity at the air-water interface enhance the transfer rate and are usually the dominant driving mechanisms for the gas flux to occur. Many researchers have tried to study the gas transfer process related to turbulence. Gases that

are environmentally important such as  $O_2$ ,  $N_2$ ,  $CO_2$ ,  $CO$  have typically low solubility. For such gases, a boundary layer of ten to hundreds  $\mu\text{m}$  thin on the liquid side controls the gas transfer process. This makes measurements at the interface very difficult. Therefore, some researchers tried to explain the physical mechanism of the process using conceptual models starting from the simplest film-model (Lewis & Whitman (1924)) to more elaborated one (Higbie (1935) and Danckwerts (1951)). The conceptual models proposed by Higbie (1935) and Danckwerts (1951) shows that the transfer velocity  $K_L$  is related to the square root of the molecular diffusivity  $D$  and a renewal rate  $r$ . The term  $r$  was an unknown parameter that must be determined experimentally for individual turbulent conditions. Some researchers such as Fortescue & Pearson (1967) and Lamont & Scott (1970) tried to relate the unknown term  $r$  to measurable hydrodynamic parameters of the flow. With this approach, Fortescue & Pearson (1967) proposed the large eddy model whereas Lamont & Scott (1970) suggested the small eddy model (detailed discussion on the existing gas transfer models are presented in Chapter 2). Many other researchers tried to relate empirically the transfer rate with measured flow conditions such as slope of a channel, velocity, etc. (e.g. Churchill (1961), Gulliver & Halverson (1989) and Moog & Jirka (2002)). A number of experimental and numerical investigations have been performed in the past, the significant experimental and numerical works of past studies are summarized in Chapter 2. However, despite the intensive research efforts, there is still lack of knowledge in order to develop a general quantitative model that provides a precise prediction of the transfer velocity in different environmental conditions. Currently, the actual physical mechanism controlling the process is still unclear. The questions of the eddy size that contributes more to the gas transfer process as well as the contribution of the turbulent mass flux are still open. Detailed and reliable experimental data is required in order to answer these open questions and so gaining improved fundamental knowledge of the gas transfer process. The improved knowledge should aid in developing more accurate models for the prediction of the transfer velocity which in practical engineering would help to improve the management of the quality of natural water resources as well as man-made reservoirs.

## 1.2 Scope and Objective

The main sources of turbulence generation in the environment can be classified into three major types, namely surface-shear-induced turbulence (e.g. wind shear on the ocean or lakes, cross current flows), bottom-shear-induced turbulence (as occurring in windless rivers, in open channel flows, in stirred grids mixing tanks) and buoyant-convective tur-

bulence (e.g. turbulence in lakes due to surface cooling). A schematic illustration of the turbulence sources and their interaction is given in Figure 1.1.

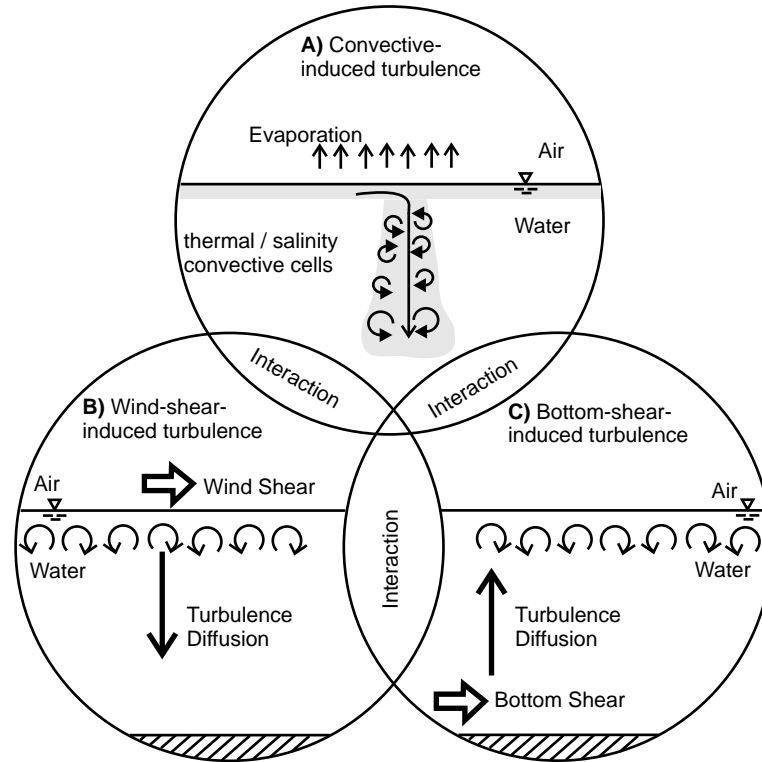


**Figure 1.1.** Schematic illustration of the dominant turbulence generation mechanisms driving interfacial gas transfer in the water environment. Type C represents the source of turbulence that is investigated in this study.

Most studies have focused on the interaction between gas transfer process and wind shear-induced turbulence (see Section 2.3). The wind shear is indeed the dominant driving mechanism for gas transfer in oceans, rivers and lakes with strong wind speeds (3-8 m/s see MacIntyre & Romero (1999)). However, in streams or rivers in the absence of strong wind, the transfer process is dominated by bottom-shear-induced turbulence (represented by C in Figure 1.1). For this type of turbulence source, the turbulence is generated below the surface and then diffuses to the interface. The present study is mainly motivated by the reaeration problem in polluted rivers and thus focuses on bottom-shear-induced turbulence. A schematic diagram illustrating the problem under investigation is shown in Figure 1.2

The objective of this study is to gain more fundamental understanding of the physical mechanisms that control the oxygen absorption process in water environment dominated by bottom-shear-induced turbulence (e.g. in natural streams under windless conditions) through detailed laboratory experiments. From the literature review in Chapter 2, it turns out that most previous studies focused on the quantification of the transfer velocity coef-

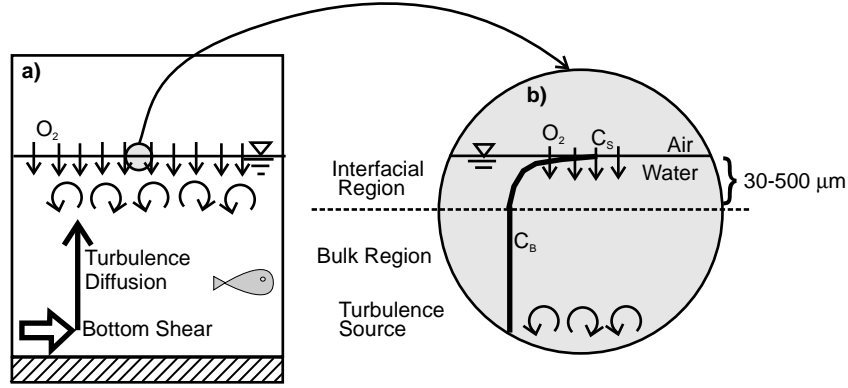


**Figure 1.2.** Schematic diagram of gas transfer process near the interface enhanced by bottom-shear-induced turbulence. a) depicts the turbulence generated at the bottom which diffuses towards the interface; b) depicts the oxygen transfer process at the interface with its limited boundary layer at the water side.

ficient  $K_L$  by trying to relate  $K_L$  to measurable parameters. As mentioned in Section 1.1, the actual physical mechanism controlling the process is still unclear. The quantification of  $K_L$  alone does not suffice in order to fully understand the actual mechanisms controlling the gas transfer process. For that purpose, it is necessary to elucidate the hydrodynamics of the flow field as well as both the molecular diffusion and the turbulent transport contributions. Therefore, detailed laboratory experiments with advanced non-intrusive optical measurement techniques were conducted in order to achieve this goal.

The results of this study focusing on oxygen transfer should not only be applicable for oxygen but also for other gases with low solubility (such as  $\text{CO}_2$ ,  $\text{NO}$ , etc.) and can be used for developing improved models for prediction and management of the quality of our rivers.

The specific goals of this study are

- to simulate the turbulence near the water surface as occurring in natural windless streams in a well-controlled laboratory facility,
- to gain more insight of the physical mechanism controlling the gas exchange process through visualization and quantification of both concentration and velocity fields using the non-intrusive Laser Induced Fluorescence (LIF) and Particle Image Velocimetry (PIV) technique, respectively,
- to elucidate the abrupt concentration changes ( $\partial C/\partial z$ ) in the region approximately 1 mm below the water surface using the data obtained by the LIF measurements,
- to determine the contribution of the turbulent mass flux ( $cw$ ) using the data obtained with the aid of simultaneous PIV-LIF measurements,
- to quantify the thickness of the concentration boundary layer,

- to measure the oxygen fluxes  $j$  at the air-water interface by using the eddy-correlation method and by performing mean oxygen bulk measurements for relatively long time, and
- to provide an experimental database for verifying theoretical models and numerical simulations.

### 1.3 Methodology

The process of oxygen absorption from the air side into the water body in a bottom-shear-induced turbulent environment was investigated experimentally. All experiments were performed in a tank equipped with a vertically oscillating grid to simulate the bottom-shear induced turbulence.

As mentioned in Section 1.1, a boundary layer of ten to hundreds  $\mu\text{m}$  thick on the liquid side controls the  $\text{O}_2$  gas transfer process. Employing intrusive measurement sensors would of course disturb the actual process. Thus, it is essential to apply non-intrusive measurements technique such as optical measurement technique. Here, a Particle Image Velocimetry (PIV) and a Laser Induced Fluorescence (LIF) were employed to measure 2D velocity and concentration fields near the interface, respectively.

Besides being non-intrusive, both the PIV and LIF techniques deliver instantaneous field information with high data density that is an advantage for elucidating the profiles near the boundary with its limited thickness. Moreover, 2D visualization with good temporal resolution (see e.g. Münsterer & Jähne (1998)) of the dissolved oxygen distribution as well as the flow-field would be of great interest to give more insight into the actual process. One other major advantage of these two techniques is that they can be coupled providing a simultaneous measurements of velocity and concentration which allows the direct measurement of turbulent mass flux. The possibility of coupling optical measurement techniques in order to quantify the turbulent mass fluxes has been shown by Law & Wang (2000) and Law & Herlina (2002) for investigating mixing processes of buoyant jets and wall jets.

The basic principle of the LIF technique is as follows. When a dissolvable fluorescent dye is introduced into the flow-field and the flow field illuminated with a laser light, the dye will fluoresce. The intensity of the emitted fluorescent light is a function of the dye concentration. Thus, the concentration level of the solute (dye tracer) can be determined by measuring the fluorescent intensity. Choosing the right fluorescent dye as tracer depends on the specific problem investigated. After intensive literature review on the different possibilities of LIF tracers and methods, it was chosen to employ the LIF technique based on the oxygen quenching phenomenon that has been developed by Vaughan & Weber (1970)

using Pyrene butyric acid (PBA) as dye tracer. One main reason why the LIF-quenching method was chosen was because it provided a concentration measurement technique that does not involve any chemical reactions. The absorbance of the PBA solution is independent of external parameters like pH value. Another advantage of this method is that PBA does not show any absorption in the spectral range of visual light so that a possible combination with other imaging techniques is easier. Detailed descriptions on the measurement techniques are given in Chapter 3.

Attempts to measure the turbulent mass fluxes across the interface under homogeneous isotropic turbulence generated far away from the interface have been made by Chu & Jirka (1992) and Atmane & George (2002). Their results were unsatisfactory most probably because of the intrusive measurement technique. Moreover, their data points were discrete and not exactly simultaneous. With the application of the combined PIV-LIF technique in this study, it was possible for the first time to obtain directly planar turbulent gas fluxes information across the air-water interface without disturbing the thin boundary layer with any intrusive measurement devices.

## 1.4 Outline

Description of the gas transfer problem with the relevant background as well as the objective, scope and methodology of the present study have been presented in the Sections above. Chapter 2 covers the literature review on gas transfer processes including a summary of the theoretical background, models of gas transfer, previous experimental investigations on gas transfer and previous investigations on grid-stirred tank. In Chapter 3, the experimental setup and employed measurements techniques are presented. A description of the construction of the tank and the oscillating grid used to simulate the bottom-shear-induced turbulence is given. The principle of the PIV and LIF techniques as well as the description of the individual components of the measuring systems are described in detail. The experiments performed in this study can be categorized into four series. The first series (Vb-series) was conducted to acquire velocity vector fields in the bulk region in order to evaluate the performance of the grid-stirred tank itself. The actual gas transfer measurements were performed in the other three experimental series (C, CV and Cb-series) and were all performed with varying turbulence intensities. The main gas transfer experiments, in which the turbulent mass flux ( $cw$ ) across the water surface was measured directly, were conducted in the CV-series by measuring the concentration and velocity fields simultaneously. Two different tracers were required for the simultaneous measurements, namely PBA solution for the concentration measurements (LIF technique) and seeding particles for the velocity measurements (PIV technique). The

C-series were conducted to measure the concentration solely with no interference from the PIV seeding particles (i.e. employing the LIF system as a stand-alone system first). The results from the C-series could latter be compared with those obtained from the simultaneous PIV-LIF measurements to ensure the minimum effect of the PIV seeding particles in the LIF images. In the last series (Cb-series), the time histories of oxygen concentration increase in the bulk region were obtained. The experimental program and procedures of all experimental series are described in Section 3.5. Before performing the gas transfer measurements in the grid-stirred tank, velocity measurements were first conducted in order to evaluate the performance of the grid-stirred tank itself. The results showed that the present grid-stirred tank was a well-controlled system that could generate turbulence with known reproducible scales. The results of the evaluation are presented in Chapter 4. Finally, the results as well as the analysis of the gas transfer measurements near the air-water interface conducted in the grid-stirred tank are presented and discussed in Chapter 5. Qualitative observations of the instantaneous velocity and concentration fields as well as their quantitative statistical results are presented. A discussion on the implications of the present results to the latest state of the art is given at the end of Chapter 5. In the last chapter, a conclusion of the present study and recommendation for future works are given.

## 2. Literature Review

### 2.1 Fundamental concepts

Transfer across the air-water interface of gases with low solubility (such as O<sub>2</sub>, CO, CO<sub>2</sub>, NO) is controlled by resistance on the liquid side (Section 2.1.2). Here, the interaction of molecular diffusion and turbulent transport governs the process. Generally, the latter is much more effective. The water surface prevents an eddy from approaching closer than roughly its length scale which leads to attenuation of the vertical velocity fluctuations. At the water surface any turbulent transport has to vanish as turbulent structures can not penetrate the air-water boundary. Therefore, in the immediate vicinity of the boundary, molecular diffusion is the only transport mechanism. The layer in which molecular diffusion exceeds the turbulent transport is termed as aqueous mass boundary layer. For slightly soluble gases the aqueous boundary layer has a thickness of ten to hundreds of  $\mu\text{m}$ .

#### 2.1.1 Governing equations

The mass flux due to molecular diffusion is described by Fick's law that states that the mass flux of a solute is proportional to the concentration gradient of the solute

$$j = -D\nabla C \quad (2.1)$$

with  $j$  denotes the mass flux,  $C$  the concentration of the transported solute and  $D$  the proportionality coefficient known as the molecular diffusivity. The minus sign in Eq. 2.1 indicates that the flux of the transported solute is from high concentration to low concentration.

Combined with the concept of mass conservation and advection, the unsteady diffusive transport results as

$$\frac{dC}{dt} = \frac{\partial C}{\partial t} + q \cdot \nabla C = -\nabla \cdot j = D\nabla^2 C \quad (2.2)$$

where  $t$  is the time, and  $q=(U,V,W)$  the instantaneous velocity vectors in  $x,y$ , and  $z$  directions. The instantaneous  $U,V,W$  and  $C$  term can be divided into two parts the time



average part and the turbulent part, known as Reynolds decomposition

$$\begin{aligned}
 U &= \bar{u} + u \\
 V &= \bar{v} + v \\
 W &= \bar{w} + w \\
 C &= \bar{c} + c
 \end{aligned}
 \tag{2.3}$$

where the overbar denotes the time average and  $u$ ,  $v$ ,  $w$  and  $c$  the fluctuating parts. Substituting Eq. 2.3 into Eq. 2.2 and time averaging over a sufficiently long period (i.e. long enough compared to a typical time constant of the system) yields

$$\frac{d\bar{c}}{dt} + \bar{q}\nabla\bar{c} = -\nabla\bar{j} = -\nabla(\bar{q}\bar{c} - D\nabla\bar{c})
 \tag{2.4}$$

Assuming that the process is horizontally homogeneous, the above differential equation can be written as

$$\bar{j} = -\left(D\frac{\partial\bar{c}}{\partial z} - \bar{c}\bar{w}\right)
 \tag{2.5}$$

where  $z$  denotes the vertical direction. The first term on the right hand side describes the molecular diffusion process and the second term the turbulent mass transport in the vertical direction. The turbulent mass transport term  $\bar{c}\bar{w}$  is a correlation term combining information from the fluctuating turbulent part of velocity and concentration which is typically not known and has to be modelled.

### 2.1.2 Transfer velocity $K_L$

The gas transfer rate is commonly parameterized by the transfer velocity  $K_L$ . The linearity of the diffusion equation (Eq. 2.2) allows the definition of  $K_L$  based on the empirical argument that the amount transferred is proportional to the concentration difference and the interfacial area. Therefore,  $K_L$  is defined as

$$K_L = \frac{j}{\Delta c} = \frac{j}{C_s - C_b}
 \tag{2.6}$$

where  $C_b$  is the dissolved gas concentration in the bulk region and  $C_s$  is the equilibrium gas concentration given by Henry's law. Henry's law states that at thermodynamic equilibrium in a two phase system, the saturated concentration  $C_s$  of a dissolved gas in the liquid phase is proportional to the partial pressure  $p$  of the gas in the gas phase

$$p = H_c C_s
 \tag{2.7}$$

with  $H_c$  denotes Henry's constant which is affected by the concentration of other solutes in the system and temperature. Liss (1983) showed that for gases with low solubility in water, the presence of dissolved solids (such as in sea water) can significantly influence the value of  $H_c$ , whereas by other gases the effects are negligible.

### 2.1.3 Liquid-side resistance

Lewis & Whitman (1924) proposed a simple gas transfer model to estimate the relative importance of gas-phase and liquid-phase resistances between different gases with varying solubility. Since then, their model has also been used for prediction of the transfer velocity as will be discussed in Section 2.2.1.

Lewis & Whitman (1924) simplified the concentration profile in a two-phase system by assuming two surface films, one on the liquid side and the other on the gas side. Each of the surface films has a corresponding gas transfer coefficient, namely  $k_L$  and  $k_g$  for the liquid and gas phase, respectively. The overall transfer velocity  $K_L$  is related to the individual gas transfer coefficients, in the following resistance-in-series model

$$\frac{1}{K_L} = \frac{1}{k_L} + \frac{1}{H_c k_g} \quad (2.8)$$

When the ratio of  $k_L/H_c k_g$  is small then the resistance on the liquid side controls the transfer process, whereas resistance on the air side controls the transfer when the ratio is large.

Generally, gases which are environmentally important (e.g. O<sub>2</sub>, N<sub>2</sub>, CO<sub>2</sub>, CO) have a low solubility. Such gases have a high Henry constant  $H_c$  and thus the transfer of such gases at an air-water interface is controlled by the hydrodynamic conditions on the liquid side.

## 2.2 Gas transfer models

Eq. 2.6 shows that the turbulent mass transport given by the correlation term  $cw$  from Eq. 2.5 represents part of the transfer velocity in the term  $K_L$  defined by Eq. 2.6. The quantification of  $K_L$  alone does not suffice in order to gain fundamental understanding of the actual mechanisms controlling the gas transfer process. For that purpose, it is necessary to elucidate the two terms on the right hand side in Eq. 2.5.

For gases with low solubility, including oxygen, a boundary layer with a thickness of only ten to hundreds  $\mu\text{m}$  on the liquid side controls the gas transfer process. This makes measurements of concentration profiles and turbulent intensities at the interface very difficult. The turbulent mass flux term (i.e. correlation term  $\overline{cw}$ ) in Eq. 2.5 is even more

difficult to quantify because simultaneous measurements of velocity and concentration is required. Therefore, in the past, many researchers tried to explain the physical mechanism of the process using conceptual gas transfer models.

An important step in formulating a model is to define the assumptions. Based on the assumptions taken, the gas transfer models can be generalized into *conceptual* models, *hydrodynamic* models and *eddy diffusivity* models. The main differences between these three model types and the most important corresponding model formulations are described in the following.

### 2.2.1 Conceptual models

”Conceptual models are simple solutions of the vertically one-dimensional diffusion equation without any explicit advective flow field. The effect of turbulence is incorporated through initial conditions and boundary conditions, which are characterized by time and spatial scales” (Brumley & Jirka 1988).

**Film model.** The very first conceptual model was the ”film model” by Lewis & Whitman (1924). They assumed a stagnant film on each side of the interface where only molecular diffusion takes place. This leads to a linear concentration profile within the stagnant films and the following relation could be deduced

$$K_L = \frac{D}{\delta} \quad (2.9)$$

with  $K_L$  the transfer velocity,  $D$  the molecular diffusivity and  $\delta$  the thickness of the stagnant film. It is clear that this model oversimplifies the actual mechanism. However, it should be noted that the essence of Lewis & Whitman (1924) model was not a physically stagnant film but rather a region in which molecular diffusion is the controlling factor in the transport process. Lewis & Whitman’s (1924) actual purpose of proposing the ”film model” was to estimate the relative importance of gas-phase and liquid-phase resistances between different gases with varying solubility. The linear assumption was thus sufficient for that purpose. The model allowed to show that for gases with low solubility the resistance of the gas-side film is negligible compared to the liquid side. In most literature, however, the ”film model” has often been used to explain the actual mechanism of gas transfer. For practical use, the thickness  $\delta$  in Eq. 2.9 gives an estimate on the lower bound of the boundary layer thickness, although it may underestimate the actual value by a factor of ten (Lee 1977).

**Penetration model.** It is clear that the ”film model” oversimplifies the actual mechanism and indeed a number of experiments (see e.g. McCready & Hanratty (1986)) found that the functional dependence between  $K_L$  and  $D$  was never linear. This led Higbie

(1935) to develop a "penetration model" which is based on a so called surface renewal effect. His idea was that the turbulence in the bulk region of the fluid would bring up fresh packages of liquid to the surface, where gas transfer takes place for a certain renewal time  $T$ . With his assumption, Higbie was able to show that

$$K_L \approx \sqrt{\frac{D}{\pi T}} \quad (2.10)$$

**Surface renewal model.** Danckwerts (1951) modified Higbie's penetration model by allowing the constant renewal time  $T$  to follow an exponential probability distribution of surface renewal rate  $r$ , so that

$$K_L \approx \sqrt{Dr} \quad (2.11)$$

where  $1/r$  may be thought as the mean time between surface renewal events.

**Film-renewal model.** O'Connor & Dobbins (1956) combined the Lewis-Whitman model with the Danckwert's model. They proposed that the interfacial liquid film maintains its existence in the statistical sense but the liquid content of the film is continuously replaced by the liquid from the bulk region. Their assumption lead to

$$K_L \approx \sqrt{Dr} \coth \left[ \frac{\delta}{\sqrt{D/r}} \right] \quad (2.12)$$

The above equation is asymptotic to the film model for small  $r$  and the surface renewal model for large values of  $r$ .

**Random eddy model.** Harriott (1962) proposed the random eddy model. He suggested that turbulent eddies approaching the interface also enhance the gas transfer process although they do not reach the interfacial layer. The eddies have a random lifetime and will arrive within a random distance from the interface. From this distance up to the surface, the transport process is solely due to molecular diffusion. Further, Harriot assumed that the random lifetime and random distance can be represented by an independent gamma distribution and derived the following relation

$$K_L \approx \frac{\sqrt{Dr}}{1 + \delta/\sqrt{D/r}} \quad (2.13)$$

**Surface divergence model.** Brumley & Jirka (1988) proposed a surface divergence model. They used the divergence of the horizontal velocity in the surface plane (i.e. surface divergence) to interpret the gas transfer mechanism directly below the water surface. They suggested that within a layer in the immediate vicinity of the interface, the gas transfer is completely due to molecular diffusion. The fluctuations of the surface divergence induce

the transport of the dissolved gas from this layer across the irrotational Kolmogorov sublayer to the depth in which ordinary rotational mixing can take over. They used Hunt & Graham (1978) irrotational source layer theory in order to estimate the Lagrangian time spectrum of the surface divergence and showed that the lower frequency eddies contributes more to the interfacial gas transfer as compared to the higher frequency eddies.

The above conceptual models have shown that  $K_L$  depends on the square root of the diffusivity. However, the hydrodynamics affecting the gas transfer process are still hidden in the  $r$  term. The random function  $r$  in Eq. 2.11 was still an unknown term that must be determined experimentally for individual turbulence conditions.

### 2.2.2 Hydrodynamic models

Some researchers elaborated the conceptual models by trying to explicitly relate the  $r$  term to measurable turbulent parameters (the hydrodynamic behavior). In hydrodynamic models, the advective diffusion equation is solved under the imposed assumption of a simple, single scale flow pattern, usually the steady cylindrical roll cell.

**Large Eddy Model.** A first attempt was made by Fortescue & Pearson (1967). They elaborated the surface renewal model by introducing the "large eddy model". They assumed that the largest turbulent eddies dominate the gas transfer process and therefore  $r$  in Eq. 2.11 can be estimated by  $u'_L/L$ . They numerically solved the advective diffusion equation of a roll cell and obtained the following relation

$$K_L = a\sqrt{\frac{D \cdot u'_L}{L}} \quad (2.14)$$

with  $u'_L$  is the root mean square turbulent fluctuation,  $L$  the turbulent integral length scale and  $a$  a constant that has a value of 1.46.

**Small Eddy Model.** Lamont & Scott (1970) and Banerjee & Scott (1968), on the other hand, suggested that small eddies are the dominant mechanism controlling the transfer process and the term  $r$  could be approximated by  $(\epsilon/\nu)^{1/2}$  with  $\epsilon$  is the turbulent energy dissipation rate near the interface and  $\nu$  the kinematic viscosity. This yields

$$K_L = b\sqrt{D} \left[ \frac{\epsilon}{\nu} \right]^{1/4} \quad (2.15)$$

Lamont & Scott (1970) obtained a value of 0.4 for the coefficient  $b$ .

**Two Regime Model.** The measurements in the laboratory and field showed good agreement with both large eddy and small eddy models. Theofanus et al. (1976) tried to interpret the results as being dependent on the range of the intensity level of the turbulence

involved and (see also Theofanus (1984)). They proposed a two-regime model in which the large eddy model is relevant at low turbulent Reynolds numbers  $Re_T$  and the small eddy model at high  $Re_T$ . By fitting the open-channel flow data from Brown (1970), they obtained the following

$$K_L = 0.73u'Sc^{-0.5}Re_T^{-0.5} \quad \text{for } Re_T < 500 \quad (2.16)$$

$$K_L = 0.25u'Sc^{-0.5}Re_T^{-0.25} \quad \text{for } Re_T > 500 \quad (2.17)$$

where  $Sc$  is the Schmidt number ( $Sc = \nu/D$ ).

Various experiments (e.g. Theofanus (1984), Asher & Pankow (1986), Chu & Jirka (1992)) agreed with these hydrodynamic models. However, there is still no general agreement on the power dependence of the Reynolds number. Experiments also show a large discrepancy of the coefficients in Eqs. 2.14 to 2.17 which could be due to the differences in the turbulent scales definitions in different experimental facilities.

### 2.2.3 Eddy diffusivity models

In contrast to the above mentioned models where only one scale of turbulence is assumed to dominate the transport process, eddy diffusivity models are true multi scale models in which the dominating scales are assumed to vary with depth. "Using eddy diffusivity closure to relate the transport to the mean concentration gradient, they provide a single description for the entire turbulent field and so avoid the need for any artificial, sharp boundaries or sudden renewal events" (Brumley & Jirka 1988). The eddy diffusivity models generally assume that the total diffusivity  $E_T$  is the sum of the molecular diffusivity  $D$  and the turbulent diffusivity  $D_t$

$$E_T = D + D_t \quad (2.18)$$

in which  $D_t$  varies with depth following a power dependence  $D_t = \alpha z^n$ , where  $\alpha$  is a constant and the  $n$  exponent should range between 2 and  $\infty$  for proper  $D$  dependence. Integrating  $1/E_T$  to infinite depth yields

$$K_L = (n/\pi)\sin(\pi/n)\alpha^{1/n}D^{1-1/n} \quad (2.19)$$

Son & Hanratty (1967) showed that  $D_t$  follows a power dependence  $n = 2$  near a gas-liquid interface. With their result, the transfer velocity is proportional to the square root of  $D$  which is the same result as for the surface renewal model. On the other extreme (i.e. when  $n = \infty$ ), the eddy diffusivity model leads to the same result as the film model.

## 2.3 Review of gas transfer studies

The main sources of turbulence generation in the environment are surface-shear-induced turbulence, bottom-shear-induced turbulence and buoyant convection turbulence (Section 1.2, Figure 1.1). Many researchers have investigated the interaction between gas transfer problem with these different turbulent conditions. In the following sections, the studies focusing on buoyant-convection-induced turbulence and wind-shear-induced turbulence are summarized briefly whereas a summary of the studies about the effect of bottom-shear-induced turbulence, which is the focus of this study, is given in more detail. In addition, significant works on the combined effect of wind-shear and bottom-shear-induced turbulence as well as the effect of the cleanliness of the interface are briefly summarized. At the end of this chapter, previous investigations on grid-stirred turbulence and a short review on measurements using the eddy-correlation method are described.

### 2.3.1 Buoyant-convective-induced turbulence

Buoyant-convective-induced turbulence (penetrative convection) is likely to be the most important source of vertical mixing in lakes with little wind exposure. Convective instability has been investigated in laboratory (Deardorff & Lilly (1969), Kastaros & Tillman (1977), in the upper oceanic boundary layer (Shay & Gregg (1984), Shay & Gregg (1986)) and in lakes (Imberger (1985); Brubaker (1987); Sander et al. (2000); Jonas et al. (2003)). None of these investigations have related the problem with gas exchange. Soloviev & Schlüssel (1994) tried to model the gas transfer process over a wide range of wind speeds and considered also the effect of convection. However, their model was based on oceanic condition so they still assumed surface shear effect due to calm wind. Only recently, Lee (2002) and Schladow et al. (2002) looked at the interaction between gas exchange under convective instability. They visualized the oxygen absorption across the air-water interface using an LIF technique in a water tank and were able to observe the process in which water with low oxygen concentration contacted the air and oxygen was transferred from the air by diffusion. Eugster et al. (2003) performed CO<sub>2</sub> gas flux measurements in lakes under convection using the eddy-covariance method. Their results indicate the importance of convective mixing to the process of gas transfer across the water surface.

### 2.3.2 Wind-shear-induced turbulence

Wind-shear-induced turbulence is very effective in enhancing the gas exchange process near the air-water interface because wind-shear is generated at the water surface which is directly in the vicinity of the interfacial region where the primary resistance of gas exchange is located. Wind speeds above 3 m/s are in particular effective since they induce

appreciable wave growth and can lead to wave breaking. Many researchers, among others Liss & Slater (1974), Broecker & Peng (1982), Jähne et al. (1979), Jähne & et al. (1987), Merlivat & Memery (1983), and Jähne & Haussecker (1998), studied the correlation between surface friction velocity  $u_{s*}$  and  $K_L$ . However, their results showed a lot of discrepancy. Detailed measurements near the water surface with wind-shear-induced turbulence were conducted by Wolff et al. (1990), Wolff & Hanratty (1994), Duke & Hanratty (1995), Banner & Peirson (1995), Münsterer et al. (1995), Münsterer (1996), Peirson & (1997), Münsterer & Jähne (1998) and Woodrow & Duke (2001). They could estimate the boundary layer thickness but the actual mechanisms was still unclear. Detailed measurements by Woodrow & Duke (2002) using LIF technique allowed the estimation of the local  $K_L$  variation along the interface. They observed detached layers containing high concentration of oxygen when waves were present. They also found that  $K_L$  values fluctuated more compared to flat interface. Besides experimental studies, several researchers (O'Connor (1983), Kerman (1984), Kitaigorodskii & (1984) and Cohen (1983)) attempted to predict the gas transfer velocity  $K_L$  through theoretical models based on rigid wall analogy of the turbulent boundary layer with modifications for a free surface. These models are characterized by a smooth surface at low wind speeds and a rough surface at high wind speeds. There are still uncertainties for determining the transition region between high and low wind speeds. Field measurements were also performed in natural streams to investigate the influence of wind-shear on gas transfer (Jirka & Brutsaert (1984), Frexes et al. (1984), Yotsukura et al. (1984)). In several studies, the interaction between eddy structures and the gas transfer has been examined. Takehara & Etoh (2002), for example, visualized the concentration fields of  $\text{CO}_2$  under wavy interfaces conditions using an LIF-Fluorescein method and indicated that both large and small 3D eddy structures played a role in the gas transfer process with wavy interface. With the help of Direct Numerical Simulation (DNS), Kunugi & Satake (2002) showed that low speed streaks and vortices were responsible for the transport of  $\text{CO}_2$  from the interface into the bulk region.

### 2.3.3 Bottom-shear-induced turbulence

In streams with weak wind speeds, the dominant driving mechanism for gas transfer is bottom-shear induced turbulence. Many studies attempted to find a practical relation between  $K_L$  and measurable flow properties (stream parameters), such as the mean velocity, slope or water depth. The relations are either entirely empirical (e.g. Churchill (1961), Thackston & Krenkel (1969), Gulliver & Halverson (1989)) or semi-empirical derived from gas transfer models with one or two empirically fitted coefficients (e.g. O'Connor & Dobbins (1956)).



Plate & Friedrich (1984) investigated the reaeration of open channel flow with varying turbulence conditions, namely bottom-generated turbulence, surface-generated turbulence and the combination of bottom and surface-generated turbulence. They proposed a relation of  $K_L$  as a function of the root mean square value of the horizontal component of the velocity near the surface (see also Section 2.3.4).

Numerous experiments (Jirka (1991), Moog & Jirka (1995*a*), Moog & Jirka (1995*b*), Moog & Jirka (1998), Moog & Jirka (1999*b*) and Moog & Jirka (2002)) have been performed to relate the gas exchange processes in open channel flow with different macro-roughness elements. They found that the results agree with the small eddy model for small roughness elements. For flows with macro-roughness, the small eddy model is only valid when the turbulence intensity in the turbulence dissipation rate expression is scaled using macro-scales (i.e. mean velocity instead of friction velocity). They argued that in this case the turbulence generation is dominated by bed particle wakes rather than the interaction between the Reynolds shear stress and the mean shear.

The various measurements in laboratory and field showed good agreement with both large eddy and small eddy models. As mentioned in Section 2.2.2, Theofanus et al. (1976) tried to interpret these results with respect to the dominating eddy size in the gas transfer process. They suggested that for high levels of turbulence the small eddy model is more relevant, whereas for low levels the large eddy model works better.

The existing models were at that time not supported by near-surface hydrodynamic measurements. Brumley & Jirka (1987) were among the first who performed detailed near-surface hydrodynamic measurements in relation to the gas transfer problems affected by bottom-shear-induced turbulence. They chose to employ a grid-stirred tank to simulate the near surface turbulence such as occurring in natural streams. Since then, other researchers, such as Chu (1993), McKenna & McGillis (2002) and Atmane & George (2002), also performed near surface hydrodynamic and gas transfer measurements in agitated tanks to investigate the gas transfer process in water environment dominated by bottom-shear-induced turbulence. The results of these works are discussed in the following.

In 1987, Brumley & Jirka published detailed near surface hydrodynamic measurements in a grid stirred tank. Detailed mapping of the vertical and horizontal turbulence structure with the aid of a rotating split-film velocimeter were performed. They proposed a surface divergence model as explained in Section 2.2.1. On the basis of the Hunt & Graham (1978) theory, they were able to define different hydrodynamic layers near the free surface that could be inferred based on their measurements as well as from scaling arguments. Their estimation of the hydrodynamic layers are illustrated in Figure 2.1. They suggested that a purely kinematic effect of the surface is expected to extend over one integral length scale  $L_\infty$  from the surface, which corresponds to the surface influenced layer. The viscous

sublayer is the scale for viscous effects near the surface. According to Hunt (1984), the viscous sublayer should be of the order of  $L_\infty Re_T^{-1/2}$ , in which  $L_\infty$  and  $Re_T$  are the integral length scale and the turbulent Reynolds number, respectively, which definition's for the grid-stirred tank case are explained in Section 2.4. The Kolmogorov sublayer  $\eta = 2L_\infty Re_T^{-3/4}$  is the scale of the smallest eddies in isotropic turbulence. The outer diffusive sublayer can be thought of as the boundary layer arising from the largest eddies. The outer diffusive layer is estimated to be of the order of  $2L_\infty Re_T^{-1/2} Sc^{-1/2}$ , with  $Sc$  is the Schmidt number. On the other hand, the Batchelor sublayer may be thought of representing the boundary layer caused by the smallest eddies and is of order  $\eta Sc^{-1/2}$ .

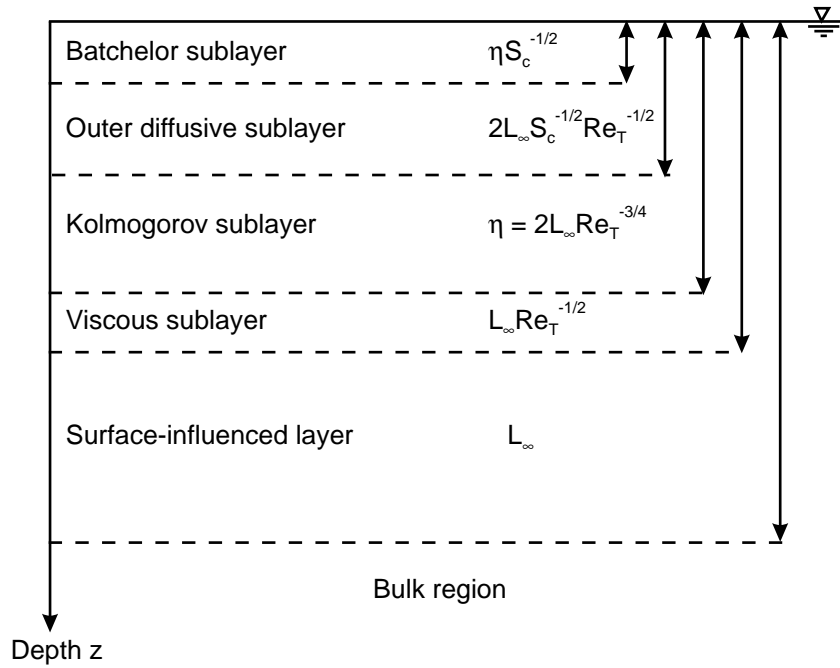


**Figure 2.1.** Schematic illustration showing estimation of hydrodynamic layers (Brumley and Jirka, 1988), with  $\eta$  is the Kolmogorov sublayer and  $Sc$  the Schmidt number. The parameters  $L_\infty$  and  $Re_T$  are the integral length scale and the turbulent Reynolds number, respectively, which definition's are explained in Section 2.4.

Jirka & Ho (1990) measured the fluctuating  $O_2$  concentrations near the air-water interface with a polarographic microprobe in the same grid-stirred tank used by Brumley & Jirka (1987). The measurements were performed at submergences from 0.1 to 0.5 mm with a precision of 50  $\mu\text{m}$ . The turbulent fluctuations (rms) seemed to reach much deeper than the measured layer. The obtained boundary layer thickness was comparable to the Lewis-Whitman film thickness. Therefore, they interpreted that in the diffusive sublayer near the surface, whose thickness is of course controlled by the turbulence conditions, molecular diffusion appear to be the dominant transport mechanism.

Chu & Jirka (1992) measured near surface liquid turbulence and oxygen concentration fluctuations in a laboratory grid stirred tank with turbulent Reynolds number  $Re_T$  in the range of 80 - 660. Hydrodynamic turbulence was measured with a rotating split-film anemometer which allowed horizontal and vertical velocity fluctuation measurements. The  $O_2$  concentrations measurements were conducted using a polarographic microprobe. They observed that the thickness of the gas boundary layer closely agrees in trend and magnitude with the Lewis-Whitman's film thickness as determined from the bulk concentration change (i.e.  $\delta = D/K_L$ ). The functional dependence on the turbulent Reynolds number was consistent with a large eddy domination. Similar measurements were conducted by Atmane & George (2002) in a micro-jet agitated tank. Their results also supported the large eddy model from Fortescue & Pearson (1967). Both Chu & Jirka (1992) and Atmane & George (2002) attempted to measure directly the turbulent mass flux *cw* quantity (Section 2.5).

George et al. (1995) performed gas transfer and hydrodynamic measurements in performed in an agitated vessel in which turbulence is produced by up flowing liquid micro jets. They showed that the square root of the interfacial turbulent kinetic energy can be chosen as a characteristic velocity that is well related to the mass transfer velocity  $K_L$ . Their conclusion supported the results from Grisenti & George (1991).

Prinos et al. (1995) performed both numerical and experimental investigations to study the gas exchange process in a jet-agitated vessel. They found that the mean and the fluctuation concentration profiles were comparable to those obtained by Chu (1993) except that there was no damping observed in their fluctuation profiles directly below the water surface. They formulated two possibilities regarding this discrepancy. First, there was a possibility that their measurements did not include the interfacial region in which the damping occurs. The second possibility is that the measurements did cover the interfacial region and in their case no such damping was present. For the second possibility, using concentration and velocity spectra, they argued with the following assumption. "When the interface is agitated enough (hence when horizontal eddies can develop freely), an intermittent interfacial renewal occurs which leads to low frequency concentration fluctuations and an increase in mass transfer."

McKenna & McGillis (2002) conducted gas transfer measurements and free-surface hydrodynamic measurements in a tank with oscillating grid-stirred turbulence. Their measurements were performed under varying degrees of interfacial contamination and turbulent Reynolds number  $Re_T$  ranging from 282 to 974. They found that bulk turbulence estimates parameterized by  $Re_T$  was unable to provide a unique relationship to the transfer velocity  $K_L$ . This was apparently because the bulk turbulence away from the interface is mostly unaffected by the presence of surface films, whereas the gas transfer

process is determined by the physics of the near surface where the dominant effects of surface contamination manifest themselves. On the other hand, the surface divergence provided a relationship to  $K_L$  that accounted for the interfacial contamination and was independent of the flow regime.

Tamburrino & Gulliver (2002) also investigated the interaction between free-surface turbulence and mass transfer in open-channel flow. Their measurements were performed in a moving-bed flume facility. Based on their free-surface measurements combined with the mass-transfer measurements of Gulliver & Halverson (1989) in the same flume facility and Lau (1975) in a different facility, they proposed the following relation

$$K^+ \sqrt{Sc} = 0.24 \sqrt{S_{\beta max}^+} \quad (2.20)$$

in which  $K^+$  is the dimensionless liquid-film coefficient,  $Sc$  is the Schmidt number and  $S_{\beta max}^+$  is the dimensionless maximum value of the surface divergence  $\beta$  spectrum. The terms  $K^+$  and  $S_{\beta max}^+$  are normalized with the shear velocity  $u_*$  and the kinematic viscosity  $\nu$ . Their results and also that from McKenna & McGillis (2002) indicate that the free-surface divergence is an important process involved in interfacial gas transport as had been proposed by Brumley & Jirka (1988). However, measuring the surface divergence directly in the field is not always practical. It is still more convenient to relate the transfer velocity to easy predicted or measurable parameters.

### 2.3.4 Combined wind-shear and bottom-shear-induced turbulence

Of course in nature, there may be a strong interaction between wind shear and bottom shear induced turbulence. Several researchers have investigated the interaction between these two types of turbulence generation source (e.g. Eloubaidy (1969), Mattingly (1977), Jirka & Chu (1993), Jirka (1994), Chu (1993), Nakayama (2000), Chu & Jirka (2003)).

As mentioned earlier in Section 2.3.3, Plate & Friedrich (1984) investigated the reaeration of open channel flow for three different cases (bottom-generated turbulence, surface-generated turbulence and the combination of bottom and surface-generated turbulence) and proposed a relation of  $K_L$  as a function of the root mean square value of the horizontal component of the velocity near the surface  $\sigma_u$ . Good correlations are found for each cases. However, large discrepancies exist for the different cases. In order to generalize their results, they proposed a "dissipation velocity"  $u_\epsilon$  to correlate  $\sigma_u$  with mean flow parameters. The dissipation velocity  $u_\epsilon$  included the effects of bottom-shear induced and wind shear induced turbulence. Based on the experimental results of Eloubaidy & Plate (1972) and Mattingly (1977), they found consistent correlation between  $K_L$  and  $u_\epsilon$  for the bottom-shear dominated and the wind-dominated regimes.

Brutsaert & Jirka (1984) formulated a criterion to determine whether the bottom-shear or the wind-shear the dominant factor for gas transfer process is. Banerjee (1990) introduced a non-dimensional shear criterion, which is the ratio of the turbulent energy production rate to the dissipation rate, that appears to account for the onset of streaky structures and their breakdown into ejections and bursts. In line with Rashidi et al. (1991), they suggested that at low interfacial shear rates, the mass transfer is dominated by the ejection generated at the bottom boundary, whereas at high interfacial shear rates, streaks and bursts similar to the ones observed near the bottom are formed at the interface and  $K_L$  scales with the surface shear velocity.

### 2.3.5 Film-free and film-covered interfaces

Besides turbulence, another important factor affecting the gas transfer across the air-water interface is the cleanliness of the interface.  $K_L$  will vary depending on the surface conditions because the damping effect of the turbulent velocity fluctuations by the surface is different between a clean and a dirty gas-liquid interface. A clean surface allows horizontal turbulence velocity fluctuations to persist up to the actual liquid surface because no large shear stresses are created at the interface. However, the vertical turbulence velocity fluctuations are damped due to the surface tension and gravity. When a gas-liquid interface is covered, for example by organic matters or chemical surfactants, greater tangential stress occurs and therefore increases the damping of the turbulence fluctuations in the interfacial region. For severely contaminated interfaces, the hydrodynamical relations is thus similar to those for solid-liquid interfacial transport (Davies, 1972). It has to be noted that the surface renewal models (e.g. Danckwerts (1951), Fortescue & Pearson (1967)) are only valid for clean interfaces. The film model (Lewis & Whitman (1924)), on the other hand, should be more suitable to describe the solid-liquid transfer process.

Asher & Pankow (1986) investigated in detail the film effect by measuring the transfer velocity  $K_L$  of  $\text{CO}_2$  in water with various surface conditions using a non-intrusive Laser Induced Fluorescence (LIF) technique based on the pH-dependent fluorescence emissions of aqueous fluorescein dyes. The different surface conditions were created by various liquid surface cleaning procedures and deliberately formed organic monolayers. They compared their results with the relations proposed by Fortescue & Pearson (1967) and Lamont & Scott (1970) given in Eqs. 2.14 and 2.15, respectively. Their results agreed well with both relationships. However, the values of the coefficients  $a$  and  $b$  in Eqs. 2.14 and 2.15 varied with the surface conditions as summarized in the following table

Asher and Pankow also compared their results with the fully-covered model as proposed by Davies (1972) but found no agreement. Thus, it seems that a severely contaminated surface does not behave exactly like a solid-liquid interface with respect to mass transfer.

Surface condition	$a$	$b$
Rayoon and vacuum cleaned (clean)	3.20 (for $> 20\text{cm/s}$ )	1.40 (for $> 20\text{cm/s}$ )
Lens paper cleaned	1.40 (for $> 25 \text{ cm/s}$ )	0.65 (for $> 20\text{cm/s}$ )
1-OD monolayer covered (dirty)	0.45	0.21

**Table 2.1.** Variation of the coefficients in Eqs. 2.14 and 2.15(source : Asher & Pankow (1986))

The experimental results from Asher & Pankow (1986) showed that the transfer velocity is indeed very sensitive to the cleanliness of the interface. In addition, Brumley & Jirka (1988) noted that the usage of normal tap water could also lead to a contaminated surface.

## 2.4 Investigations on grid-stirred turbulence

As mentioned in 1.3, a grid stirred tank system was employed in the current study to simulate bottom-shear-induced turbulence. This type of turbulence generation was chosen because it generates near homogenous turbulence with almost zero-mean velocity. In comparison with open channel flows, the absence of advection in the tank reduces the intricacy in performing measurements since no mean flow is present. Many researchers who investigated mixing phenomena have used oscillating grids to imitate the natural turbulence in the laboratory. The pioneers were among others Cromwell (1960) and Turner (1968). The results of Brumley & Jirka (1987) showed that the grid stirred tank is also suitable for investigation in the area of gas transfer which allows direct data comparison with the results obtained in the present study. The most important experimental works on this type of turbulence generation mechanism are presented in the following paragraphs.

Thompson & Turner (1975) studied in depth the characteristics of the turbulence generated by oscillating grids with square and round bars. They measured the horizontal velocity fluctuations above the oscillating grid using a rotating hot-film probe. They explained that the flow produced can be discussed in terms of three consecutive processes as follows

1. There is generation of a quasi steady jet flow very close to each grid bar. The form and intensity of the motion in this region depends on the cross-section of the bars and on the amplitude and possibly viscosity.
2. The jets interact and break down to provided turbulence which is advected by the jets.
3. This turbulence decays with further distance away from the grid.

Further, they observed that the jet flows remain distinct up to two mesh lengths away from the grid and then merge into a pattern which is influenced by the shape of the the tank and by small differences in the strength of the flow from different parts of the grid.

On the basis of their measurements, they suggested that the turbulence characteristics generated in this way depends highly on the precise grid forms and amplitude of oscillation. They found that the turbulence fluctuations depend linearly on the frequency of the oscillating grid and that the longitudinal integral length scale  $L_u$  varies linearly with the distance from a virtual origin that was located approximately at the mid position of the grid  $z_{cs}$ .

$$L_u = 0.1z_{cs} \quad (2.21)$$

Hopfinger & Toly (1976) showed that it is possible to generate nearly isotropic turbulence with the aid of an oscillating grid of appropriate geometry without producing a mean flow. They found that the solidity of the mesh should be less than 40%. If the solidity is too high, the wakes or jets are unstable and merge into larger jets which affects the length scale and the turbulence fluctuation values. Their argument was as follows when the solidity of the oscillating plate is high for example 60 %, the velocity in the holes exceeds the velocity of the plate so that the turbulence will originate predominantly in these jets. In the case of grids which have solidity less than 40 %, the pockets of turbulence are aligned with the bars and very probably have the structure of wakes on either side, the final turbulence is a result of wake interaction.

Hopfinger & Toly (1976) measured the horizontal and vertical velocity fluctuations using a rotating hot film probe and showed that the vertical distribution of the turbulence in such a grid-stirred tank can be related to the grid parameters, namely the frequency of the grid oscillation  $f$ , the stroke or amplitude of the grid's oscillation  $S$  and the mesh size or centre to centre mesh spacing  $M$ . Their relation is

$$u' = cfS^{1.5}M^{0.5}z_{cs}^{-1} \quad (2.22)$$

with  $z_{cs}$  is the distance from a virtual origin (near the centre of the stroke) towards the water surface and  $c$  is a constant. Based on their data, Hopfinger & Toly (1976) proposed a value of 0.25 for  $c$ . They found that the degree of anisotropy of the vertical fluctuations  $w'$  to the horizontal fluctuations  $u'$  was in the range of 1.1 to 1.3 at distances farther than 7 cm from the grid. Using auto-covariance of the velocity signals, they confirmed the finding of Thompson & Turner (1975) that the longitudinal integral length scale increases linearly with a coefficient of 0.1 from the virtual origin.

Of course Eq. 2.22 is valid only when no horizontal boundary exists and therefore this equation would not hold near a free surface. The measurements from Brumley & Jirka (1987) showed that within a distance of 10% of  $z_s$  from the surface, the profiles do not follow the Hopfinger-Toly profile anymore, with  $z_s$  is the distance from the centre of the grid to the water surface. They addressed this layer as the surface influenced layer which

extended approximately one far-field integral length scale  $L_\infty$  from the surface (Section 2.3.3, Figure 2.1)

$$L_\infty = 0.1z_s \quad (2.23)$$

Hunt & Graham (1978) developed a theory to calculate the grid-generated turbulence near a solid wall for wind tunnel measurements. In their theory, the surface-influenced layer (source layer) is thought as the superposition of a homogeneous turbulent field with an irrotational velocity field to cancel out the vertical velocity fluctuations that would otherwise occur at the surface. Hunt (1984) claimed that the solution of Hunt & Graham (1978) theory can be directly applied to a flat gas-liquid interface. Brumley & Jirka (1987) fitted Hunt & Graham (1978) results for the horizontal velocity fluctuation with

$$\frac{u'^2}{u_\infty'^2} = 1.5 - \frac{1}{2} \left\{ (2\lambda_1 Z_+^{2/3})^{-p_2} \exp(-g^{1/2} Z_+) + [1 + 2\lambda_3 Z_+^{-7/6} \exp(-g^{1/2} Z_+)]^{-p_2} \right\}^{-1/p_2} \quad (2.24)$$

the vertical velocity fluctuation by

$$\frac{w'^2}{w_\infty'^2} = \left[ (\lambda_2 Z_+^{2/3})^{-p_1} \exp(-g^{1/2} Z_+) + 1 \right]^{-1/p_1} \quad (2.25)$$

the longitudinal length scale  $L_u$  by

$$\frac{L_u}{L_\infty} = \left( \frac{u'^2}{u_\infty'^2} \right)^{-1} \quad (2.26)$$

and the transversal length scale  $L_w$  by

$$\frac{2L_w}{L_\infty} = \left[ \left( \frac{2\pi\Psi}{\lambda_2} Z_+ \right)^{-p_2} \exp(-g^{1/2} Z_+) + 1 \right]^{-1/p_3} \quad (2.27)$$

with  $\lambda_1 = 2.67$ ,  $\lambda_2 = 1.4$ ,  $\lambda_3 = 0.522$ ,  $p_1 = 1.54$ ,  $p_2 = 0.575$ ,  $p_3 = 0.63$ ,  $\Psi = 0.88$  (see Hunt & Graham (1978)) and  $Z_+ =$  the non-dimensional distance  $z/L_\infty$  from the interface. The value of  $g = 0.558$  is an empirical fit but based on detailed theoretical calculations (see Brumley & Jirka (1987)).

Brumley & Jirka (1987) combined the fitted Hunt & Graham (1978) relation with the one from Hopfinger & Toly (1976). The vertical velocity fluctuations were well predicted by the combined profile. On the other hand, the horizontal fluctuations were less well predicted (further discussion in Section 5.3). In their study, the longitudinal and transverse integral length scales were obtained from the zero intercept of the power spectra divided



by four times the square of the turbulence intensities. The integral length scales showed good agreement with the Hunt & Graham prediction.

In order to characterize the different turbulence levels for the gas transfer process, Brumley & Jirka (1987) used  $2L_\infty$  and the far-field velocity fluctuations  $u'_\infty$  estimated using the Hopfinger & Toly relation at the water surface as the length and velocity scales, respectively. The factor 2 in the length scale arises because the length scale for isotropic turbulence is theoretically twice as large as the longitudinal integral length scale  $L_\infty$  (Tennekes & Lumley 1972). The Reynolds number  $Re_T$  can thus be defined by

$$Re_T = \frac{u'_\infty 2L_\infty}{\nu} \quad (2.28)$$

with  $\nu$  is the kinematic viscosity.

The above mentioned investigations were performed with invasive measurement technique (hot film probe). The effect of this intrusion is unclear. Some non-intrusive measurements have been performed by, among others, McDougal (1979), Brunk et al. (1996) and Lyn (1997) using Laser Doppler Velocimetry (LDV), Acoustic Doppler Velocimetry (ADV) and Particle Image Velocimetry (PIV), respectively. Recently, Cheng & Law (2001) performed detailed investigation on the characteristics of turbulence generated by oscillating grid using the non-intrusive PIV technique. Their results agreed well with the turbulence decay relation proposed by Hopfinger & Toly (1976). The simultaneous planar measurements allowed them to compute the spatial correlation of velocity fluctuations. They found that the ratio of the length scale is almost proportional to the distance from the grid. The proportionality coefficients for the longitudinal correlation coefficient ranged from 0.1 to 0.2, which was comparable to previous works, while those from the transverse correlation coefficient are in the range of 0.06 to 0.17. In addition, they showed that the statistical results in their experiments are only consistent and approach constant values when the number of samples exceeds approximately 400. They observed that significant horizontal variations of the velocity fluctuation occur near the grid and that the fluctuations achieve homogeneity only around three mesh sizes away from the grid midplane.

Orlins & Gulliver (2002) performed velocity measurements on the water surface in a grid-stirred tank. Their measurements were similar to that conducted by McKenna & McGillis (2002), only their measurement window was significantly larger. They used a special surface PIV technique in order to obtain the velocity fields on the surface. Based on the calculated vorticity and divergence, they were able to show that the velocities and vorticity fields varied relatively slowly with time and space whereas the divergence changed more rapidly. The velocity spectra showed that the dominant gradient increased from -2 to -3 with increasing grid frequency. They compared their results with the results obtained in an open-channel experiment (Kumar et al. (1998)) and found very good

agreement. This implies that the application of a grid-stirred tank is suitable for the simulation of bottom-shear induced turbulence.

## 2.5 Eddy-correlation method

The instantaneous and mean turbulent mass fluxes ( $cw$  and  $\overline{cw}$ ) can be determined directly through simultaneous measurements of gas concentration fluctuations and velocity fluctuations near the surface region. This technique of measurements is called the eddy-correlation method. Jones & Smith (1977) and Francey & Garratt (1978) were among the first who measured CO<sub>2</sub> fluxes between ocean and atmosphere using the eddy-correlation method. McGillis et al. (2001) performed direct air-sea CO<sub>2</sub> flux measurements through the correlation of the fluctuation of CO<sub>2</sub> with the turbulent velocity fluctuation in the atmospheric layer. For strong winds (more than 11 m/s), they found that the eddy-correlation method obtained 1 order higher than indirect method such as radiocarbon and radon (Broecker & Peng (1982)).

Chu & Jirka (1992) were the first who applied the eddy-correlation method to measure the turbulent mass flux across the interface under homogeneous isotropic turbulence conditions generated far away from the interface. They simultaneously measured near surface liquid turbulence and oxygen concentration fluctuations in a grid stirred tank. Unfortunately, they could not find any particular trend of the mean turbulent mass flux ( $\overline{cw}$ ) distribution. Recently, Atmane & George (2002) performed similar eddy-correlation measurements as Chu & Jirka (1992), only that the near surface velocities were measured using a non-intrusive LDV technique. Like Chu & Jirka (1992), no trend for the  $\overline{cw}$  in the vertical direction could be found but they discussed the physical meaning of the separated positive and negative components of the turbulent mass flux.

Both Chu & Jirka (1992) and Atmane & George (2002) used invasive measurement technique (polarographic oxygen microprobe) which may be the reason why no particular trend for  $\overline{cw}$  could be detected since the actual mechanism of gas exchange within the limited boundary layer was disturbed.

### 3. Experimental Setup, Measurement Techniques and Program

The aim of this study is to gain more understanding of the physical mechanisms that control the oxygen absorption process into the liquid phase in a bottom-shear-induced turbulent environment. For that purpose, it is necessary to resolve in time and space both the molecular diffusive transport ( $D\partial C/\partial z$ ) and turbulent transport ( $cw$ ) terms in Eq. 2.5. The gas boundary layer in which transition takes place between the saturation concentration  $C_s$  at the interface and the concentration  $C_b$  in the bulk region has a thickness of only a fraction of millimeter for typical environmental turbulence conditions. Therefore, it is important to elucidate the concentration and velocity fields within this thin aqueous boundary layer in the vicinity of the air-water interface. The application of non-intrusive measurement devices, such as optical measurement techniques, is thus essential. In order to measure the turbulent mass flux ( $cw$ ) directly, the velocity and concentration must be measured simultaneously. In this study, a combined Particle Image Velocimetry (PIV) and Laser Induced Fluorescence (LIF) technique that enables simultaneous and spatially synoptic measurements of two-dimensional velocity and concentration fields was employed.

The different components of the present experimental setup and measurement techniques as well as the verification of the techniques are described in detail in this chapter. All experiments were performed in the Environmental Fluid Mechanics Laboratory of the Institute for Hydromechanics, University of Karlsruhe, Germany.

#### 3.1 Experimental setup

A grid-stirred tank system was employed to generate bottom-shear-induced turbulence with known reproducible scales (i.e. well-controlled conditions). In such a system, the turbulence is generated away from the surface and decays as it diffuses towards the interface. Despite the differences of turbulence generation, the interaction between the interface and the turbulence has similar characteristics as that occurring at the water surface in rivers (see e.g. Tamburrino & Soval (1999)).

This type of turbulence generation was chosen because it is characterized by almost zero-mean velocity and homogenous turbulence (Hopfinger & Toly 1976). In comparison

with open-channel flows, the zero-mean velocity in the tank reduces the intricacy in performing measurements since no mean flow is present. In addition, many researchers such as Brumley & Jirka (1987), Thompson & Turner (1975), Chu (1990), showed that the grid-stirred tank is suitable for investigation in the area of gas transfer and direct data comparison with the present results is possible.

A schematic illustration and a photograph of the present experimental setup is shown in Fig. 3.1. The dimensions of the tank were similar to that constructed by Brumley & Jirka (1987). It was made of perspex with a  $50 \times 50 \text{ cm}^2$  bottom and a depth of 65 cm. Glass windows were installed at the side walls to enhance optical access for laser techniques (PIV and LIF).

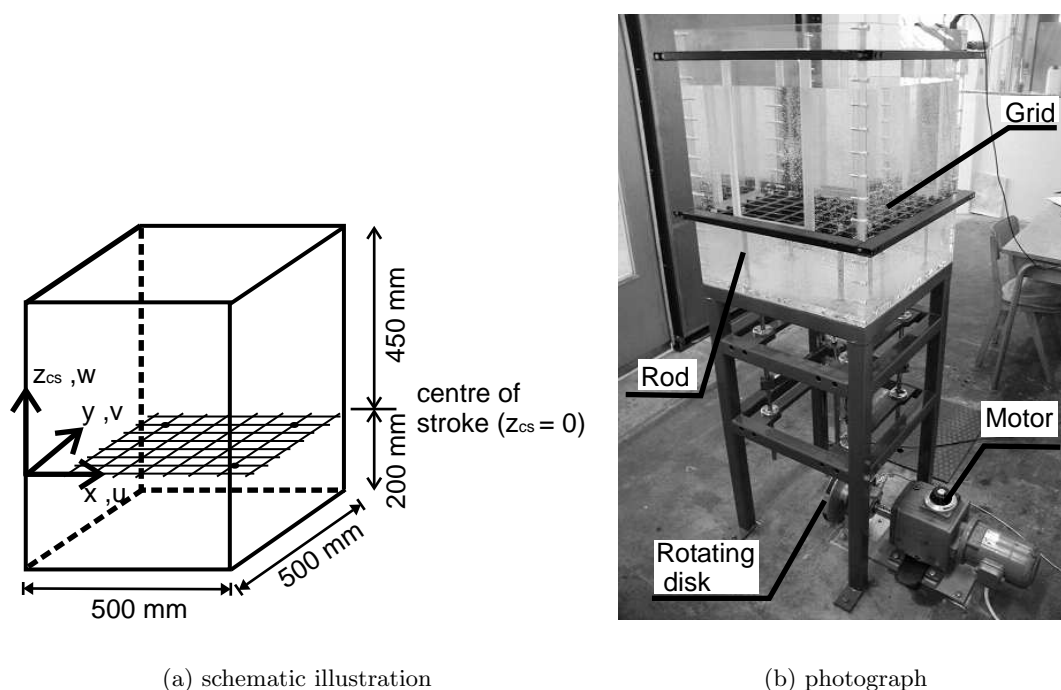


**Figure 3.1.** Grid-stirred tank : (a) schematic illustration of the tank with coordinate system, (b) photograph showing the tank equipped with the oscillating grid

A vertically oscillating grid was installed near the bottom of the tank to generate the turbulence. It consisted of an aluminium plate perforated to form a  $7 \text{ bar} \times 7 \text{ bar}$  grid. The centre to centre mesh size  $M$  was 62.5 mm, the hole size was  $50 \times 50 \text{ mm}^2$ , resulting in a mesh solidity of 36 %. This solidity was considered to be optimal to avoid secondary motions and inhomogeneity (Hopfinger & Toly 1976). It is important to ensure that the grid was installed exactly horizontal to minimize presence of secondary motions.

A motor was employed to oscillate the grid vertically with the help of a rotating disk that was mounted in front of the motor. A rod, screwed on to the rotating disk, connected

the disk with the oscillating grid. Different magnitudes of the grid's stroke were possible by adjusting the distance between the position of the screwed rod on the disk and the centre of the rotating disk. This driving system could be operated with frequencies ranging from 1.5 Hz to 10 Hz and strokes between 5 mm to 100 mm.

Four steel rods that enter the tank through the bottom were installed to connect the grid to the driving motor that was anchored at the floor. The sealing system installed at the four rods has a lifetime of about 15 hours operation (when operated with less than 4 Hz).

Figure 3.4, shows four additional steel rods that are mounted above the grid, which extend up to above the water surface. These rods were additionally installed in order to avoid large fluctuations of the water surface caused by the displaced water volume when the grid moves up and down. With the four extension rods, the water depth could be maintained constant but small surface waves were still present, especially near the extension rods. The effect was not significant for turbulence measurements in the bulk region but not negligible for detailed near surface measurements. Therefore, stationary sleeves were mounted to the lid of the tank to cover the upper extension rods to minimize the surface waves caused by the up and down motion of the rods.

In order to optimize the performance of the grid-stirred tank, it was observed in preliminary experiments that it is important to take precaution when turning on and off the motor. Measurements should start not earlier than 20 minutes after turning on the motor. This is necessary to allow the flow to establish a statistically stable condition.

## 3.2 Measurement techniques

Basically, three types of measurements were performed namely,

- velocity field measurements in the bulk region and near the water surface
- measurements of the oxygen concentration field near the water surface
- measurements of the oxygen concentration in the bulk region

Concurrently to the three main measurements, the temperature of the water and the air pressure were also monitored. This was important since the Henry's constant  $H_c$  (and thus the gas concentration at equilibrium  $C_s$ ) is affected by temperature and air pressure of the system (see Section 2.1.2).

The velocity and oxygen concentration fields at the water surface were measured simultaneously using the PIV and LIF techniques, respectively. A review on both measurement techniques as well as the description of the different components of all measurement setups are given in the following sections.

The whole optical system for PIV and LIF (except for the LIF laser) is positioned on a traverse system which can be moved vertically in 0.2 mm steps.

### 3.2.1 Particle Image Velocimetry (PIV)

**Principle of PIV.** Horizontal and vertical velocity vectors of the flow field were obtained using the Particle Image (PIV) technique. This technique enables the measurements of instantaneous and planar velocity fields. Figure 3.2 illustrates the principle of the PIV technique.

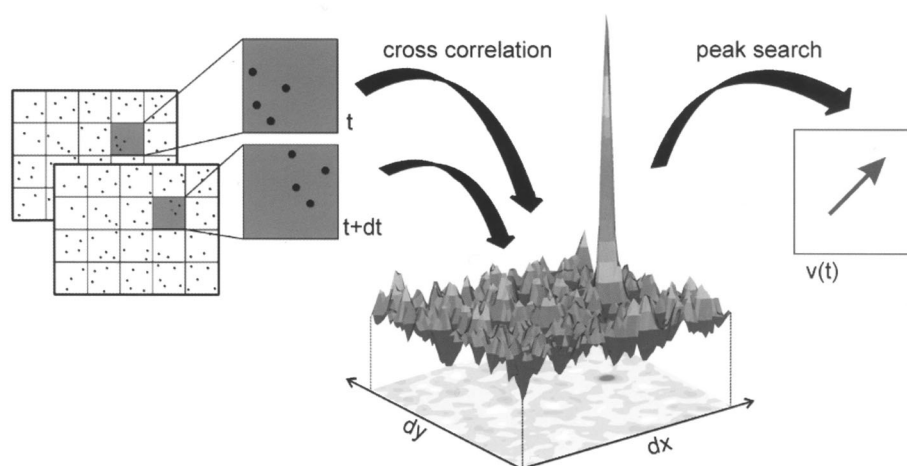


**Figure 3.2.** Principle of PIV technique (source : LaVision)

The basic principle of PIV is based on the well-known kinematic equation (i.e. distance divided by time). In PIV, the movements of seeding particles which are introduced into the flow field are followed. The positions of the particles are captured (recorded) in images (frames) with a known time interval. The distance travelled by the particles are determined by performing auto-correlation or cross-correlation depending on the illumination technique. Auto-correlation is performed when a frame is illuminated two times. The movements of the particles can be acquired but not the direction. On the other hand, if two frames are individually illuminated then cross-correlation is performed to measure the movements of the particles. With this latter method, both direction and travelled distance can be obtained. A whole frame is divided into several small grids usually addressed as interrogation area. The local displacement or distance travelled is the mean value from all particles detected within the interrogation area. When using cross-correlation, the local displacement vector for each interrogation between two successive images is determined in the following form

$$C_{orr}(dx, dy) = \sum_{x=0, y=0}^{x < n, y < n} I_1(x, y) I_2(x + dx, y + dy) \quad (3.1)$$

with  $I_1$  and  $I_2$  are the image intensities in the first and second frame, respectively. The resulting 2D  $C_{orr}$  array gives the correlation strength for all displacements (dx,dy) within the interrogation area between the two successive frames. Figure 3.2 also shows an example of a correlation distribution obtained using Eq. 3.1 in which the highest peak represents the most probable displacement.

Finally, the velocity can be deduced using Eq. 3.2.

$$\text{velocity} = \frac{\text{most probable displacement}}{\text{time between two frames}} \quad (3.2)$$

**Accuracy of PIV.** The accuracy of the PIV measurement technique depends strongly on several parameters that are discussed as follows.

*Particle Size.* The size of the particle imaged on the CCD camera is an important factor in terms of the measurement accuracy. The PIV algorithm is trying to determine the center of mass of a particle by fitting a Gaussian curve over the intensity distribution of that particular particle. If the particle is smaller than one pixel, the algorithm would of course find the center of mass at a position of an integer pixel value. If most of the particles are smaller than one pixel then the particle displacement distribution of a vector field contains strong peaks at the position of integer displacement. This effect is called peak-locking. According to Raffel et al. (1998), when the particles are larger than 1 pixel, the center of mass can be determined with an accuracy of 0.1 pixel and so avoiding the peak-locking effect.

*Seeding density.* The seeding density within the flow-field influences the probability of detecting the valid displacement as has been shown by Raffel et al. (1998). They suggest that the number of particles within one interrogation area should be more than 5 particles.

*Selection of interrogation area size and time between illumination.* Theoretically, it is desirable to have the flow-field displacement as large as possible in order to obtain more accurate measurement results. The maximum possible measurable displacement would be actually that of the length of the interrogation area. However, velocity biasing effects and signal drop out may occur when the displacement is greater than 25% of the interrogation area. For a typical 32 x 32 pixels interrogation area, the maximum recommended displacement on the CCD camera should not exceed 8 pixels. This implies that the selection of the time between the two consecutive illuminations has to

be selected carefully. The time interval should be long enough to allow a measurable displacement but can not be too long in order to avoid velocity biasing effects and signal drop out.

A common technique to evaluate the accuracy of a PIV system is given by Westerweel (2000), where artificial particle clouds are generated with random spatial distribution to simulate a known reproducible particle movement under well determined boundary conditions. The most important components of the PIV system used in this study is the same as the one used by Weitbrecht et al. (2002). Based on the technique described in Westerweel (2000), the accuracy (systematic error) of the current PIV system was evaluated to be less than 0.5 pixels (Weitbrecht et al. (2002)). The accuracy is, however, very sensitive to pre- and postprocessing parameters (Weitbrecht 2004). In the present study, no preprocessing was performed and the postprocessing performed was restricted to discarding vectors that are obvious outliers.

**PIV components.** Figure 3.3 shows the PIV setup used in this study. The PIV system was manufactured by LaVision and consisted of tracer, illumination system, image recorder and synchronization unit. The individual components employed in this study are described in the following.

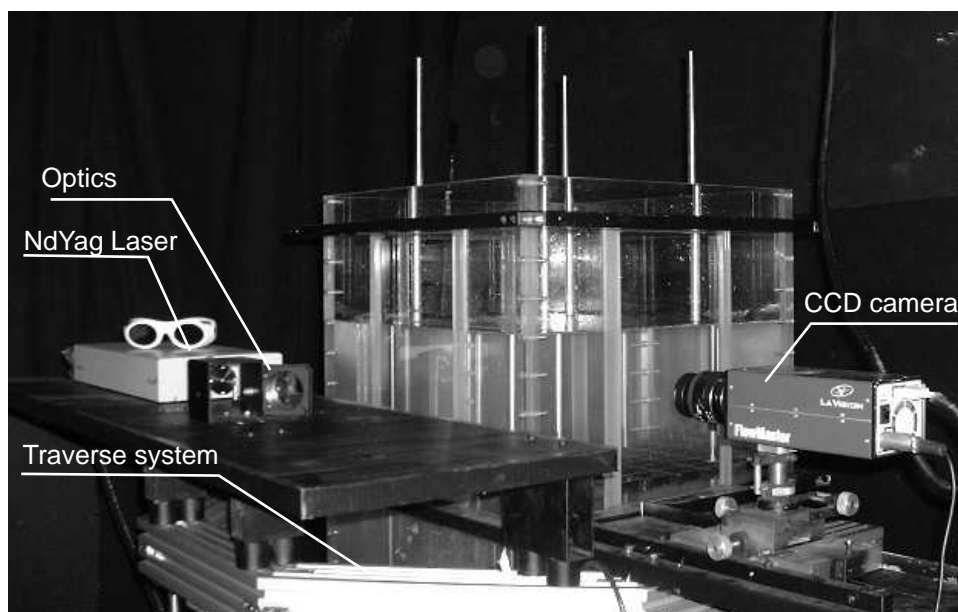


**Figure 3.3.** Experimental setup showing the configuration of the tank and PIV system

*Seeding particles.* The particles must be small enough to be able to follow the flow accurately, yet large enough to scatter sufficient light so that they could be detected by the



image recorder. Particles that are too small are invisible to the camera or they may evoke peak-locking effects as discussed above. The particles should also be neutrally buoyant in the fluid that means they should have approximately the same density as the fluid. Polyamid particles with nominal diameter of  $10\mu\text{m}$  and  $60\mu\text{m}$  from Degussa were used in this study.

*NdYag Laser.* The area of interest was illuminated with a laser light sheet in order to detect the particle movements. The laser was a dual-cavity Q-switched Nd:YAG laser which emits pulse-pairs with an energy level of 25 mJ per pulse. The emitted light is green at a wavelength of 532 nm. The Q-switch allows the pulse duration to be as short as 7 ns, thus giving a stroboscopic effect whereby the positions of the seeding particles are almost frozen during the illumination. The time interval between two recorded frames is determined by the time between the laser pulse-pairs. As explained above, the optimal time between pulses must be set so that the distance travelled by the particles from the first to second frame does not exceed a quarter of the interrogation area. A light sheet optic was mounted in front of the laser to expand the laser beam to a light sheet. A UV-mirror was used to direct the laser sheet into the centre of the test tank.

*CCD camera.* A SensiCam charge coupled device (CCD) camera was used in order to capture the illuminated flow field. It has a resolution of  $1280 \times 1240$  pixels and a grey scale depth of 12 bits. Two types of objectives were used. The first was the Nikon 50 mm / 1.8 to visualize approximately a  $70 \times 70 \text{ mm}^2$  flow-field. The second type was a macro objective, Componon-S 5.6/135 from Schneider Optics, to zoom into an investigation area of approximately  $25 \times 20 \text{ mm}^2$  from a distance of about 50 cm. A band pass filter was mounted in front of the objective so that only the scattered laser light reached the camera chips. The camera was positioned perpendicular to the laser light sheet. The recording rate was limited by the CCD camera transfer rate which is 4 Hz (double frames).

*Synchronization unit.* The synchronization of the camera and laser through a programmable timing unit (PTU) board was managed using the DaVis software developed by LaVision. DaVis also provides the algorithm for computing the vector fields.

### 3.2.2 Laser Induced Fluorescence (LIF)

The LIF technique employed here is based on the oxygen quenching phenomenon and has been developed by Vaughan & Weber (1970) to measure oxygen concentration in living tissues. Wolff et al. (1990) were the first who adopted this method to study gas transfer processes. They measured 1D oxygen concentration profile near the air-water interface in a small chamber. Since then, LIF based on the oxygen quenching technique

has been applied by other investigators in the field of gas transfer. Some of these works are shortly mentioned here. Wolff & Hanratty (1994) employed this method to study oxygen absorption in a stratified air-water flow with smooth and wavy interfaces. Münsterer et al. (1995) performed measurements in a circular wind / wave flume using two types of LIF techniques simultaneously. The first technique was LIF based on the oxygen quenching method and the second was a Fluorescein technique employing HCl as tracer. They could obtain 2D concentration information with very high time resolution up to 200 frame/s using the Fluorescein-HCl method. On the other hand, only 1D concentration profiles could be measured with the oxygen quenching method. The oxygen quenching method was then improved by Duke & Hanratty (1995) to measure not only 1D profiles but also 2D concentration fields in an air-water flow channel with wavy and flat interfaces. Other 2D measurements have been performed recently by Woodrow & Duke (2001) in a wave tank.

All applications of the 2D LIF-oxygen quenching technique mentioned above had been performed in channels with very shallow water depth (less than 30 mm) and the interrogation area were relatively near the side walls (less than 40 mm). Recently, Lee (2002) and Schladow et al. (2002) applied the 2D LIF technique in a deep water tank (0.6 m) to visualize the oxygen transfer across the air-water interface driven by natural convection. However, it should be noted that in their case the thermal boundary layer was between 2-4 mm so they had not looked into the small scale of ten to hundreds  $\mu\text{m}$  thick which is the scale that must be elucidated in the other previous LIF works as well as in our present case.

The application of LIF technique in the present study differs from previous works in that it was applied for the first time in a grid-stirred tank that enables the simulation of gas transfer process at the interface induced by bottom shear turbulence. The water depth of 480-490 mm which was considerably deeper than previous set-ups and the interrogation window which was about 250 mm away from the sidewalls made the application of LIF more complicated. This setup allows larger scales of turbulent eddies to grow and thus a wider spectrum of turbulent eddies can be observed.

**Principle of LIF.** The present LIF technique takes advantage of the fact that the fluorescent intensity which is proportional to the fluorescent lifetime of a fluorescent dye will be disturbed or quenched by the presence of oxygen molecules in a solution. The oxygen molecules offer a path for the excited molecule to relax back into the ground state without the emission of a photon. This process is called quenching. Therefore, the method is called oxygen quenching. Vaughan & Weber (1970) showed that the best fluorescent dye is pyrene butyric acid (PBA).

Oxygen, as the quencher, perturbs the excited states of the fluorescent dye, pyrenebutyric acid (PBA) and quenches the fluorescent lifetime of PBA. The fluorescence lifetime reduces from 160 ns in the absence of oxygen to 65 ns in air-saturated solution (Wolff & Hanratty 1994). This small variation in fluorescent lifetime significantly changes the intensity of the fluorescence. It shows an approximate 15% loss of fluorescence intensity with dissolved oxygen concentrations increasing from 0.8 to 8 mg/l (Münsterer 1996).

The lifetime of an excited molecule in the absence of a quencher may be expressed as

$$\tau = \frac{1}{k_f + k_d} \quad (3.3)$$

with  $k_f$  is the rate of light emission and  $k_d$  the sum rates of radiationless deactivation.

The fluorescence lifetime  $\tau$  is proportional to the fluorescence intensity  $F$  and depends on the quencher concentration  $Q$  as described by the Stern-Vollmer equation

$$\frac{F_o}{F} = \frac{\tau_o}{\tau} = 1 + K_{sv}Q \quad (3.4)$$

where  $\tau_o$  and  $F_o$  are the fluorescence lifetime and intensity respectively in the absence of the quencher,  $K_{sv}$  the Stern-Vollmer quenching constant. Hence, the quencher (in this case dissolved oxygen) concentration level can be determined by measuring the intensity of the emitted fluorescence.

This LIF-quenching technique was chosen because it provides a concentration measurement technique that does not involve any chemical reactions. The absorbance of the PBA solution is independent of external parameters like pH value. Another advantage of this method is that PBA does not show any absorption in the spectral range of visual light. This makes a possible combination with other imaging techniques easier. In comparison with the HCl-Fluorescein method, the quenching method offers the possibility to measure the fluctuation values of the oxygen concentration in time. This is not possible with the fluorescein method because the influence of air-sided controlled HCl flux fluctuations is superimposed to the surface concentration changes (Münsterer & Jähne 1998).

**LIF components.** Fig. 3.4 shows the LIF system configuration which consists of tracer, illumination system, image recorder and synchronization unit. The optical set-up was in general similar to the one developed by Duke & Hanratty (1995) and Woodrow & Duke (2001) except that here the light sheet was aligned from above the water surface instead from the bottom of the tank. The illumination from above was similar to Münsterer et al. (1995), only that the laser beam was expanded into a sheet in the present study. The individual components of the optical setup used in this study are described as follows.

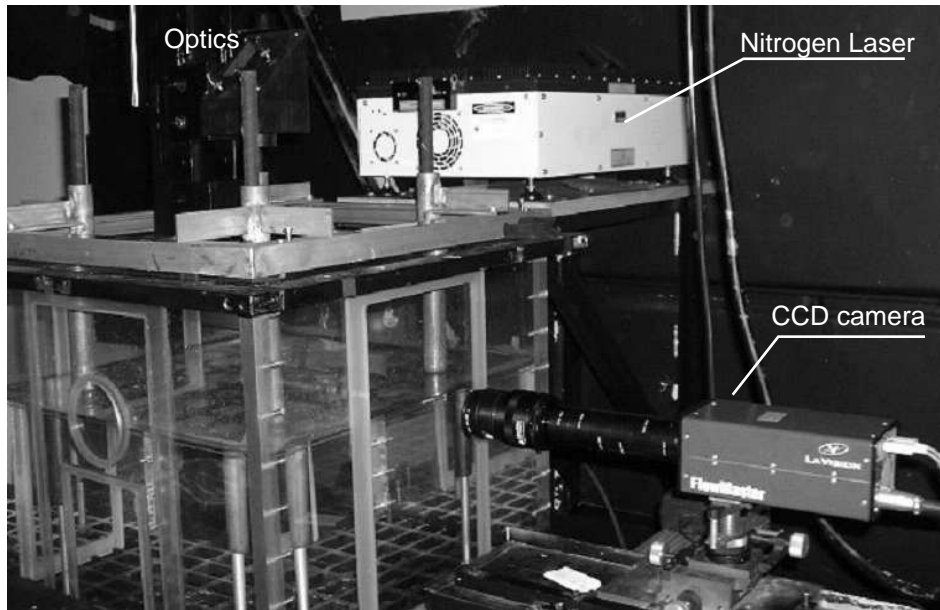


**Figure 3.4.** Experimental setup showing configuration of tank and LIF system

*PBA.* The test tank was filled with pyrene butyric acid (PBA) solution which served as the dissolved oxygen tracer. Preliminary experiments showed that the Lambert-Beer absorption of the nitrogen laser in PBA solution is relatively high. The optimum PBA concentration was found to be  $2 \cdot 10^{-5}$  Molar. A lower concentration resulted in too weak fluorescence whereas higher concentration made the solution too opaque which hampered any optical access.

*Nitrogen laser.* A pulsed nitrogen laser (MNL 801) with a mean energy power of 0.4 mJ was used to excite the PBA solution. The laser emission was at 337.1 nm which was ideal since the absorption peak of PBA is at 340 nm (see Figure 3.5). A UV-mirror was placed in front of the laser to guide the laser beam into the centre of the test tank. The laser beam was then expanded to a sheet by a combination of two spherical and one cylindrical ( $f=-25.4$  mm) lenses. The configuration of the illumination system was so that the sheet excited a 2D flow field at the centre of the tank. A disadvantage of directing the laser sheet from above the water surface arises due to dust particles floating on the water surface that partially block the laser light as it crosses the water surface. This leads to additional noise in the recorded intensity images when particles happened to float at the water surface within the measurement window. An ideal configuration to avoid this type of noise is if the laser light enters the test tank from the side walls. However, a laser with a very high power would therefore be required so that sufficient intensity still reaches the measurement area. For the laser power available, the present illumination configuration was an optimal solution.

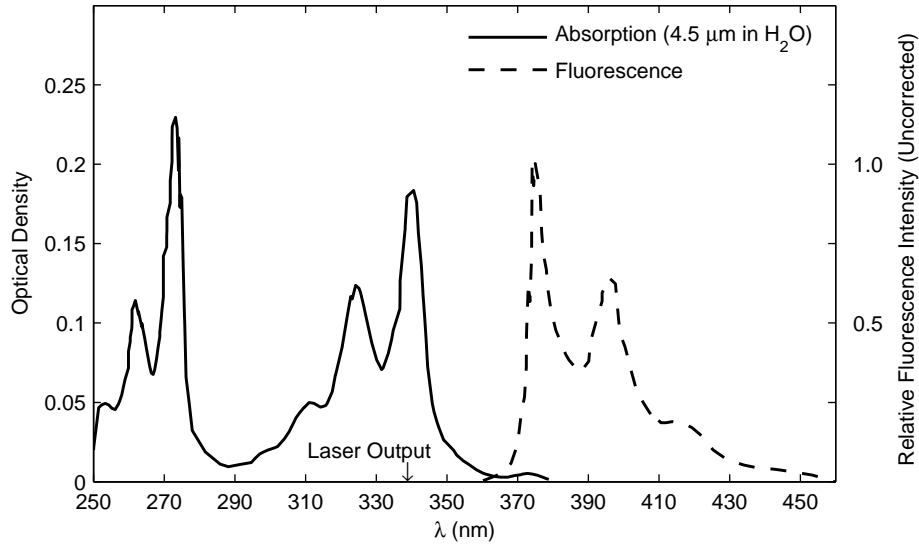


**Figure 3.5.** Absorption and fluorescence spectra of PBA (Vaughan and Weber, 1970)

*CCD camera and objective.* The intensity of the PBA fluorescence was captured with a FlowMaster CCD camera. It has a resolution of 1280 x 1024 pixels and a grey scale depth of 12 bit. A macro objective (Componon-S 5.6/135 from Schneider Optics) was used to zoom into an investigation area of approximately 9 x 7 mm<sup>2</sup> from a distance of about 30 cm. Hence, the measurement resolution was as small as 7  $\mu$ m. The PBA fluorescence lies between 370 - 410 nm. An optical bandpass filter was mounted in front of the camera in order to block out the scattered laser light and all ambient light. Hence, it was ensured that only the fluorescent light could pass through. The camera was tilted about 10° so that the viewing point was slightly from below the water surface. This adjustment was necessary to eliminate interference from the water surface meniscus at the side wall facing the camera. The recording interval of the camera was 4 Hz. Restricted by the memory (RAM) capacity of the computer, the maximum number of successive images in one run of experiment is limited to 300 frames.

*Programmable Timing Unit (PTU) board.* A PTU board synchronized all LIF activities including the synchronization between the laser pulse and camera. The commercial software DaVis provided the interface for communications between the user and the LIF system.

### 3.2.3 Bulk concentration measurements

The dissolved oxygen concentration in the bulk region was measured using the InoLab Level 3 oxygen sensor. An accuracy of approximately  $\pm 0.01$  mg/l was expected with a minimum flow rate of 10 cm/s. Therefore, the probe was installed about 10 cm below the centre of the grid stroke to ensure the fulfillment of the minimum flow rate required by the probe to measure accurately. The oxygen probe was also used to measure the temperature of the water and the air pressure.

## 3.3 Image Processing (LIF interpretation)

Several processing steps had to be performed on the raw images before the concentration information could be extracted. The processes include noise removal, water surface detection, correction of laser attenuation and correction of optical blurring near the interface. The image processing procedure was in general similar to that described in more detail by Woodrow & Duke (2001). The specific procedure and optimal parameters for the present case are discussed in the following. Figure 3.6 to 3.10 illustrate the individual processing step of a vertical intensity profile.

First, ten iterations of filtering in the horizontal  $x$  and vertical  $z$  directions were carried out to remove noise. An adaptive filter with filter size of 9 pixels was applied in the  $z$  direction. In the  $x$  direction, the filter size was 19 pixels. The different filtering size was chosen since the changes along the horizontal direction are not as abrupt in the vertical direction. The advantage of the adaptive filter is that it preserves strong gradients but it requires longer processing time. Figure 3.6 and 3.7 show an example of a vertical intensity profile before and after filtering, respectively.

In the next processing step, the water surface ( $z=0$ ) was detected. As mentioned previously, the camera was slightly tilted so that the reflection on the water surface was also recorded on the image. The location of the water surface could thus be detected by searching for the reflective symmetry line. Evaluating a single vertical column, the symmetry point would be at the zero-crossing of the first derivative of the profile. The Canny method was used to detect the zero-crossing. By finding the symmetry point for all vertical profiles, the water surface over the whole image could be determined and the whole image could be rearranged to the reference level where  $z = 0$  is the detected water surface (see Figure 3.8).

The intensity of the laser light decays exponentially when it travels through the water column as described by the Lambert-Beer theory. Consequently, the fluorescence response must be corrected to take into account the intensity attenuation. The Lambert-Beer exponent was determined by fitting an exponential curve on each vertical intensity profile

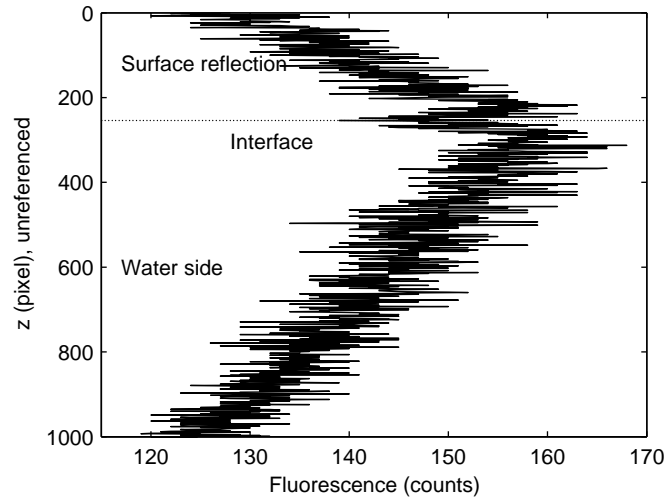


**Figure 3.6.** Example of a vertical intensity profile from a raw image

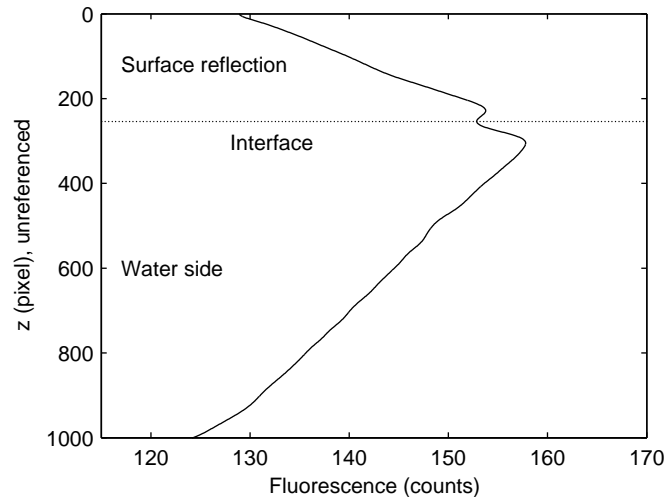


**Figure 3.7.** Example of vertical intensity profile after filtering

in the bulk region. The fitted exponents from 20 randomly chosen images were then averaged. The Lambert-Beer effect on each image was then corrected by dividing the recorded intensity with the averaged exponent.

The filtering and correction of laser attenuation reduce the sharp gradient at the interface. Assuming that directly below the water surface only molecular diffusivity occurs (i.e. a linear concentration distribution), the blurring effect is corrected by extrapolating the sharpest gradient up to the interface (see Figure 3.9).

Finally, the concentration level of the dissolved oxygen can be extracted. Assuming no gas phase resistance, the dissolved oxygen concentration at the interface should always be equal to the saturation concentration  $C_s$ . The conversion from each vertical profile of the

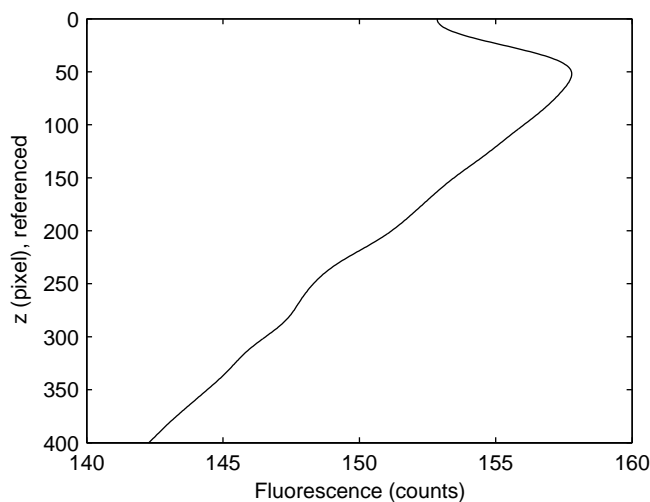


**Figure 3.8.** Example of vertical intensity profile after rearranged to the reference level where  $z = 0$  is the detected water surface

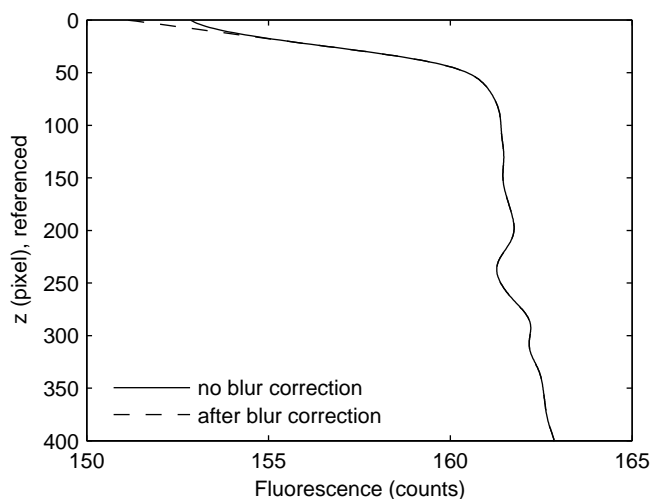


**Figure 3.9.** Example of a vertical intensity profile after the Lambert-Beer and optical blurring effect corrections

measured fluorescence intensity  $F$  values to DO concentration values  $C$  can be described by the following relation

$$C(z) = \frac{C_s - C_b}{F_b - F_i} [F_b - F(z)] + C_b \quad (3.5)$$

where  $C_b$  is the bulk concentration and  $F_i$  and  $F_b$  are the fluorescence intensities at the interface and the bulk, respectively (see Figure 3.10).

Performing the conversion from fluorescence values to DO levels on all vertical profiles, a whole planar contour map of the instantaneous DO concentration was obtained.



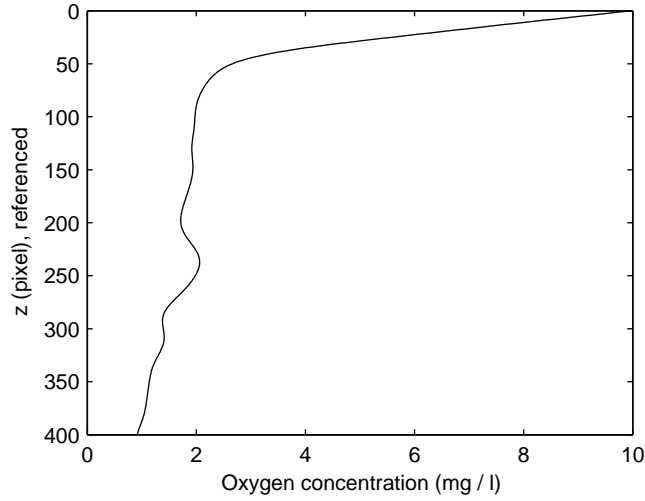


**Figure 3.10.** Example of a vertical intensity profile after converted into concentration

### 3.4 Verification of the LIF setup and image processing

Preliminary experiments without grid movements were performed using the same arrangements as the actual experiments in order to verify the current LIF setup. Five sets of images were recorded and the oxygen concentration was varied from 0.9 to 7.3 mg/l. The images were processed with the same image processing algorithm described in the previous section, except that no transformation from fluorescence intensity to concentration was done (i.e the last step was omitted). The normalized fluorescence intensities obtained for each level of oxygen concentration is plotted in Figure 3.11. The fluorescence intensities are normalized with the measured intensity in the absence of the quencher (i.e. the oxygen concentration = 0 mg/l). The data points represent the temporally mean values from 100 instantaneous images recorded in each set. The mean value was taken in order to rule out the variation of the incident laser light intensity that was about  $\pm 4\%$ . Münsterer et al. (1995) found that the best fit of the Stern-Vollmer equation (Eq. 3.4) yielded a  $K_{sv}$  value of  $683 \pm 70$  l/mol. The curve is included in the graph and it agrees well with the present data points.

It should be noted that the effect of the inconsistency in the incident laser light would be eliminated in the final step where fluorescence intensity is transformed into DO concentration since for each vertical profile the intensities are normalized when applying Eq. 5.1. It is difficult to determine the individual contribution to the total error from each component of the whole LIF setup. However, the standard deviation from DO images with the same concentration suggest that the resolution of the current set-up is about  $\pm 5\%$ .

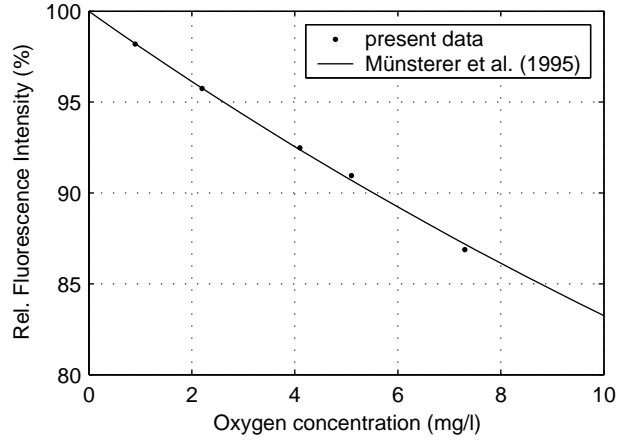


**Figure 3.11.** Relation of fluorescence intensity measured with the CCD camera to the absolute oxygen concentration measured with the oxygen probe. The fluorescence intensity is represented in a normalized form  $F/F_o$  in which  $F_o$  is the intensity when no oxygen is present

### 3.5 Experimental Program and Procedure

The overall experimental setup (i.e. the grid-stirred tank construction) and the individual components of the measurement systems have been discussed in Chapter 3. In this chapter, the experimental program and procedure as well as the specific objective for each particular series are described.

The experiments performed in this study can be categorized into four series with some differences in the experimental setup corresponding to the aim of each particular series. The first series (Vb-series) was conducted to acquire velocity vector fields in the bulk region in order to evaluate the turbulence characteristics generated by the grid-stirred tank itself. The second experimental series (C-series) was performed to measure the oxygen concentration variation near the interface. The main gas transfer experiments were performed in the third series (CV-series), in which the velocity and concentration fields were measured simultaneously using the combined PIV-LIF system. In the last series (Cb-series), the time histories of oxygen concentration increase in the bulk region were obtained.

The gas transfer measurements (C, CV and Cb-series) were all performed for five different turbulence conditions. In order to induce the interfacial gas transfer, a concentration gradient is forced by lowering the oxygen concentration in the test tank. The different levels of turbulence intensities were controlled by varying the frequency of the oscillating grid from 2 to 6 Hz which corresponded to  $Re_T$  (see Eq. 2.28) from 260 to 780. The typical grid conditions for the gas transfer measurements are given in Table 3.1. As mentioned in Section 2.2, Theofanus (1984) suggested that the flow regime could be categorized into low turbulence flow when  $Re_T$  is lower than 500 and high turbulence flow when  $Re_T$  is

higher than 500. The chosen  $Re_T$  investigated in this study covered both regimes and thus it is expected to cover a sufficient wide spectrum of turbulent eddies.

Experiment Series	Frequency $f$ (Hz)	Stroke $S$ (mm)	Water depth (mm)	$Re_T$
C1, CV1, Cb1	2	50	486	260
C2, CV2, Cb2	3	50	485	390
C3, CV3, Cb3	4	50	485	520
C4, CV4, Cb4	5	50	490	650
C5, CV5, Cb5	6	50	480	780

**Table 3.1.** Typical experimental parameters for the gas transfer measurements (C-series, CV-series, and Cb-series). For the calculation of  $Re_T$ , the viscosity  $\nu$  was taken as the viscosity at the reference temperature 20°C

### 3.5.1 Velocity measurements in the bulk (Vb-series)

The purpose of the experiments in the Vb-series was to examine the turbulence characteristics produced in the grid-stirred tank system. Therefore, the flow-fields in the tank from near the grid up to near the interface with varying turbulence intensities were measured.

Five series of experiments (Vb1 to Vb5) were performed in order to evaluate the grid-stirred tank (see Table 3.2). In all experiments, the grid was operated with a stroke of 5 cm. The frequency of the oscillation was varied between 2 to 6 Hz. The water depth between 449 and 480 mm thus the distance from the mid position of the grid to the water surface ranges between 249 to 280 mm. The turbulent Reynolds number varies from 260 to 780 and covers the range in which the gas transfer measurements were performed. The main experimental parameters are summarized in Table 3.2. The time between pulses (between two PIV frames) for each experiment depended on the frequencies of the oscillating grid and the positions of the camera and varied between 0.7 and 5 ms.

Experiment Series	Frequency $f$ (Hz)	Water depth (mm)	$Re_T$	Camera window (cm from sidewall)	Number of vector fields
Vb1	2.56	454	330	centre : 21.5 - 28.7	450
Vb2	4.00	449	520	centre : 21.5 - 28.7	450
Vb3	2.56	450	330	side : 2.71 - 9.45	450
Vb4	2	480	260	centre : 21.5 - 28.7	900
Vb5	6	480	780	centre : 21.5 - 28.7	900

**Table 3.2.** Experimental parameters for the Vb-Series

The instantaneous velocity fields were acquired using the PIV-technique described in Section 3.2.1. Figure 3.12 shows the experimental setup for the Vb-series. The laser light sheet was aligned so that it crosses the test tank from one side to the other side of the tank exactly at the centre of the tank. Thus, a cross-sectional plane was illuminated at the centre of the tank. The measurement windows were approximately  $7 \times 9 \text{ cm}^2$  large. This dimension was chosen so that the  $60\mu\text{m}$  seeding particle covered at least 3 pixels on the CCD camera in order to ensure the high accuracy of the PIV measurements (see Section 3.2.1).

In the vertical direction, the flow-field of interest extended from near the oscillating grid up to 3-5 cm below the water surface (i.e. about 20 cm). Consequently, the camera had to be shifted vertically several times to obtain a vertical velocity profile that covered the whole area of interest.

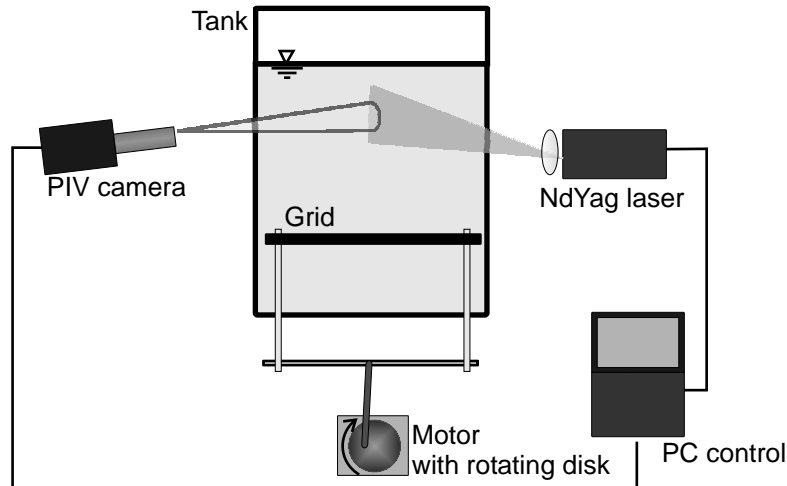


**Figure 3.12.** Schematic illustration of the experimental setup in the Vb-series

A plan view of the experimental setup is presented in Figure 3.13 to illustrate the positions of the laser light sheet and the camera. The positions of the measurement windows (PIV windows) in experiment Vb1, Vb2, Vb4, and Vb5 were located approximately at the centre of the tank. Experiment Vb3 had the same grid conditions as Vb1 only the measurement window was shifted from the centre of the tank closer to the side walls of the tank to evaluate the horizontal homogeneity of the turbulence produced by the grid-stirred tank.

Restricted by the RAM capacity of the computer, the maximum number of successive images in one run was limited to 150 (double frames) in the Vb1 to Vb3 series. The RAM capacity was latter upgraded so that the limit of 150 could be increased to 300 images. The statistical results of the velocity fluctuation are not consistent for small samples and only approach a constant when the sample exceeds 400 images (Cheng & Law 2001).

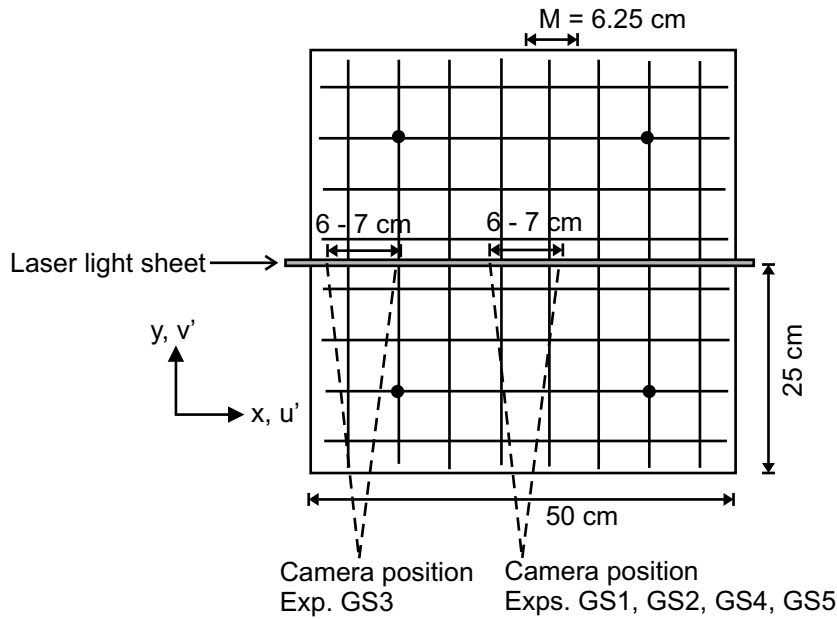


**Figure 3.13.** Plan view of the camera positions in the Vb-series

Thus, it was necessary to perform more than one run of experiment for each camera position in all experimental series. Here, three consecutive runs for each camera positions were performed, resulting in 450 and 900 samples for the Vb1 to Vb3 and Vb4 to Vb5, respectively (see Table 3.2).

The procedure for the Vb-experiments comprised of the following steps:

*Laser light alignment.* The laser was aligned by adjusting its height and angle carefully until it illuminated the desired measurement area.

*Camera focusing and calibration.* The next step following the laser light sheet alignment was focusing the camera onto the plane illuminated by the laser light sheet. The camera was positioned such that it was perpendicular to the laser light sheet to avoid or minimize geometrical distortion. One advantage of the PIV software employed here is that it provides a built in algorithm to calibrate geometrical distortion. Therefore, a plate with cross signs drawn at regular intervals on it was placed at the measurement location. Based on the image with the cross signs, the image distortion coefficients were calculated and the geometrical distortion could be calibrated. The distance between the crosses drawn on the calibration plate is known. Therefore, the scale factor object to image could also be determined.

*Tank preparation.* Before each experiment the test tank was drained, cleaned and filled with tap water up to the desirable water depth (480 to 490 mm). The PIV seeding particles ( $60 \mu\text{m}$ ) were added and well mixed into the water in the test tank with a

concentration of approximately 0.05 to 0.1 g / l. The exact optimal seeding density concentration were adjusted in preliminary experiments prior to each actual experiments so that more than five particles could be detected in one interrogation area.

*Turbulence generation.* The turbulence generation was started by turning on the motor connected to the oscillating grid. To ensure a stable turbulence condition, the measurements started at least 20-30 minutes after the motor was turned on.

The results and discussion of the Vb-series are given in Chapter 4.

### 3.5.2 Concentration measurements near the interface (C-series)

The oxygen concentration near the interface was measured using the LIF technique described in Section 3.2.2. Actually, the main objective of this study is to measure directly the turbulent mass flux quantities ( $cw$ ). For that purpose, a simultaneous measurement technique of velocity and concentration must be employed. Two different tracers were required for the simultaneous measurements, namely PBA solution for LIF and seeding particles for PIV. One would expect that the presence of the PIV particles may affect the LIF images since they may partially block the LIF laser light within the LIF measurement window. Consequently, the aim of the C-series was to measure the concentration solely with no interference from the PIV seeding particles (i.e. employing the LIF system as a stand-alone system first). The results could latter be compared with those obtained from the simultaneous PIV-LIF measurements to ensure the minimum effect of the PIV seeding particles in the LIF images. The stand-alone LIF system configuration for the C-series is depicted in Figure 3.14.

As listed in Table 3.1, the C-series were performed for five different turbulent Reynolds numbers. The RAM capacity of the LIF system was limited to 300 images (single frame). Therefore, three sets of images were recorded consecutively in order to achieve sufficient number of samples for the statistical analysis. The specific experimental conditions such as temperature  $T$ , air pressure  $p$  and bulk concentration  $C_b$ , are given in Table 3.3

Experiment Series	$Re_T$	$T$ (°C)	Air pressure (mbar)	$C_b$ (mg/l)
C1	260	15.9	1001	0.68
C2	390	16.0	1001	0.79
C3	520	16.2	1001	0.75
C4	650	17.9	1013	1.05
C5	780	17.7	1013	1.05

**Table 3.3.** Experimental conditions in the C-Series

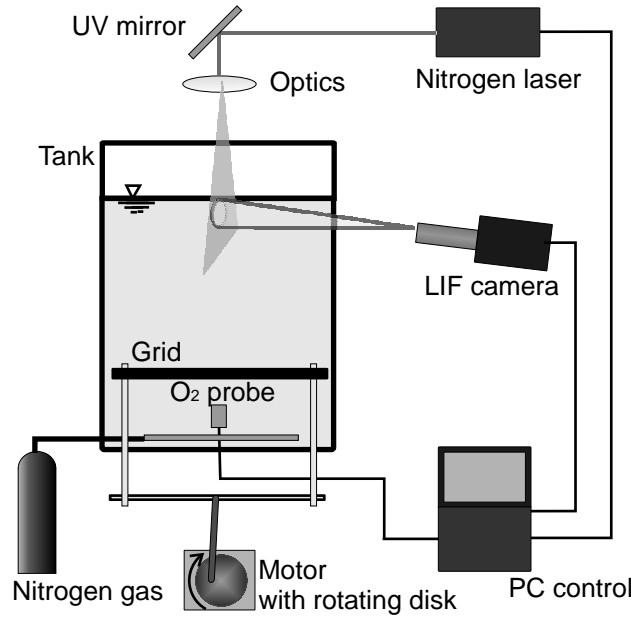


**Figure 3.14.** Schematic illustration of the experimental setup in the C-series

In order to investigate the gas transfer process, it is important to elucidate the concentration profile within the limited aqueous boundary layer which has a thickness of ten to hundreds  $\mu\text{m}$ . Brumley & Jirka (1988) suggested an estimation of the different hydrodynamic sublayers. The estimated sublayers for the present experimental conditions are given in Table 3.4. As explained in Section 3.2.2, the measurement resolution was approximately  $7 \mu\text{m}$ . Thus, the resolution of the current LIF system is sufficient to elucidate the Kolmogorov sublayer.

$Re_T$	260	390	520	650	780
Surface influenced layer	28.6	28.5	28.5	29.0	27.5
Viscous sublayer	1.78	1.45	1.25	1.14	0.99
Kolmogorov sublayer	0.89	0.65	0.52	0.45	0.37
Outer diffusive sublayer	0.16	0.13	0.11	0.10	0.09
Batchelor sublayer	0.040	0.029	0.023	0.020	0.017

**Table 3.4.** Estimated hydrodynamic thickness (in mm) based on Brumley and Jirka (1987)

The procedures of the experiments in the C-series included :

*Laser alignment and camera calibration.* The procedure for this step is the same as the laser alignment and camera calibration performed in the Vb-series described in Section 3.5.1, except that in the C-series the camera was not set perfectly perpendicular to the measurement area but intentionally tilted so that the viewing point was slightly

from below the water surface (see Section 3.2.2). The angle was less than  $10^\circ$  so that geometrical distortion was negligible.

*Tank preparation.* For the LIF measurements, the cleanliness of the tank was important. The presence of dust particles leads to additional noise to the fluorescence signals. Moreover, the presence of surface films such as from cleanser liquid affect the interfacial gas transfer process (Asher & Pankow (1986)). Therefore, the tank was cleaned with extra care before filling it with the PBA solution up to the desirable water depth (480 to 490 mm).

*PBA solution preparation.* PBA can be purchased in powder form. One problem is that it is not soluble in water. Therefore, before mixing the PBA with the water in the test tank, a 0.1N stock solution of PBA in NaOH was first prepared. This stock solution was then diluted to a  $2 \cdot 10^{-5}$  M solution in water for the experiments.

*Oxygen stripping.* Nitrogen bubbles were introduced into the test tank to purge the oxygen from the water. An initially low DO concentration of about 0.6 mg/l was achieved after 20 minutes of bubbling.

*Surface cleaning.* As can be seen in Figure 3.14, the laser light sheet entered the test tank from above the water surface. A disadvantage of directing the laser sheet from above the water surface is that dust particles floating on the water surface could partially block the laser light as it travels into the test tank. Thus, it is essential to keep the surface as clean as possible. Before the experiments started, the surface was cleaned from dust particles using a suction device.

*Turbulence generation.* Same as in the Vb-series, the measurements started only after 20-30 minutes after the grid oscillated to ensure the turbulence steady state condition.

### 3.5.3 Simultaneous concentration and velocity measurements (CV-series)

In the CV-series, the main gas transfer experiments were performed in which the turbulent mass flux ( $cw$ ) across the water surface was measured directly. The velocity and concentration fields near the interface were measured simultaneously using the combined PIV-LIF technique. The setup of the LIF system was exactly the same as in the C-series. The PIV system was coupled with the LIF system as schematically illustrated in Figure 3.15. The PIV camera was positioned at the opposite side of the LIF camera. The measurement window of the PIV camera was approximately  $20 \times 20 \text{ mm}^2$  so that it covered the  $10 \times 10 \text{ mm}^2$  area of the LIF camera. A smaller measurement window than  $20 \times 20 \text{ mm}^2$  for the PIV camera was not possible because much more seeding particles would be needed. If too much seeding particles are added into the water, the water would turn opaque which hampers the optical access of both PIV and LIF lasers. In addition,



the noise in the fluorescence signals would no longer be negligible when too much seeding particles are present in the LIF images.

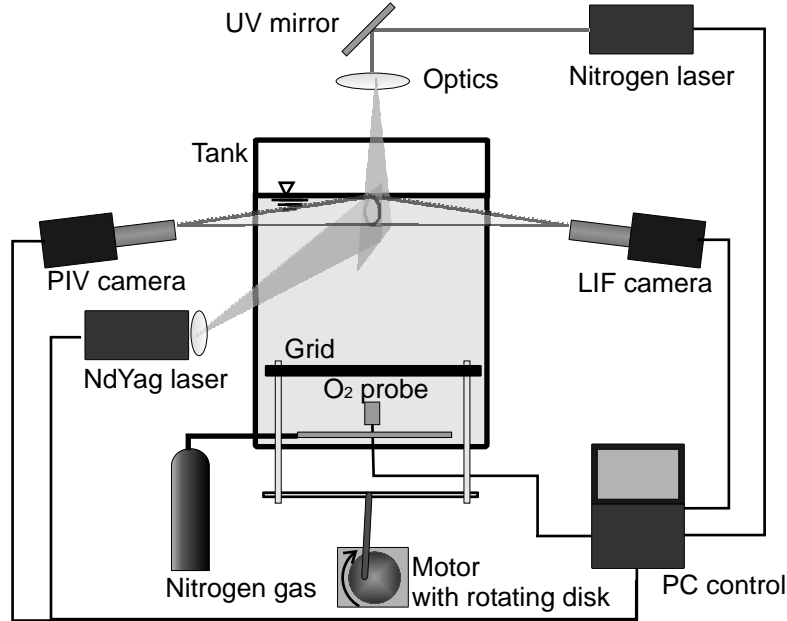


**Figure 3.15.** Schematic illustration of the experimental setup in the CV-series

The specific experimental conditions such as temperature  $T$ , air pressure and bulk concentration  $C_b$ , are listed in Table 3.3

Experiment Series	$Re_T$	$T$ (°C)	Air pressure (mbar)	$C_b$ (mg/l)
CV1	260	14.3	1001	1.02
CV2	390	14.4	1001	0.97
CV3	520	14.8	1001	0.98
CV4	650	15.0	1001	0.77
CV5	780	15.3	1001	0.89

**Table 3.5.** Experimental conditions in the CV-Series

The procedures for the simultaneous measurements were in principle the same as for the stand-alone LIF measurements (C-series). The tank preparation, PBA solution preparation, camera focusing and calibration, nitrogen bubbling, surface cleaning and turbulence generation are all the same as in the C-series. Some additional steps though were required for the coupling with the PIV technique, namely alignment of the two laser light sheets, alignment of the two cameras and preparation of the tracers. These additional steps are described as follows.

*Alignment of the two lasers.* The two lasers were aligned until the light sheets perfectly coincide with each other and illuminated the same desired measurement area.

*Alignment of the two cameras.* The two cameras were aligned by placing a string at the centre of the test tank. The cameras were positioned so that the string was located approximately at the centre of the imaged area. The position of the string could then be used as the reference point where the two cameras coincide.

*Tracer.* As mentioned previously, two tracers were needed for the simultaneous measurements, namely PBA solution and PIV seeding particles. The tank was first filled with PBA solution (procedure is same as in the C-series) and then PIV seeding particles with nominal diameter of  $10\ \mu\text{m}$  were added and well mixed with the solution.

### 3.5.4 Bulk concentration measurements (Cb-series)

The goal of these series of measurements is to determine the transfer velocity  $K_L$ . Therefore, the oxygen concentration in the tank was lowered and then the concentration increase in the bulk region were monitored for approximately 3 hours. Figure 3.16 shows the experimental setup for the Cb-series. The placement of the oxygen probe 10 cm below the grid centre ensures the fulfillment of the minimum flow rate required by the probe to measure accurately. It is common to present the  $K_L$  values at a reference temperature of  $20^\circ\text{C}$ . Thus, it was also necessary to monitor the temperature to allow temperature corrections.

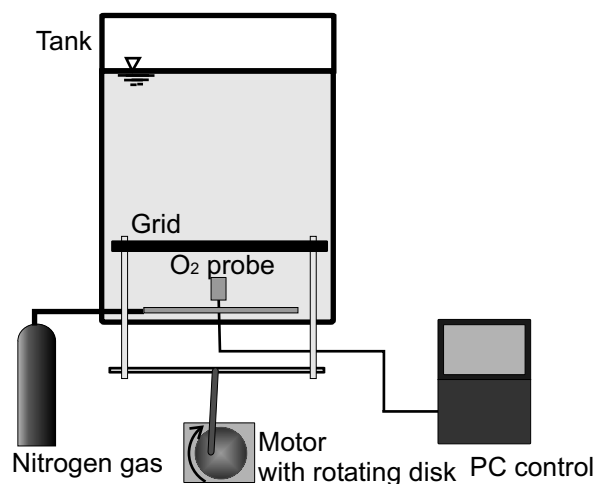


**Figure 3.16.** Schematic illustration of the experimental setup in the Cb-series

Similar as in the C and CV-series, the dissolved oxygen was purged from the water in the test tank by bubbling nitrogen gas and the experiments started 20-30 minutes after the grid has been turned on. The initial and final oxygen concentrations as well as the initial and final water temperature measured in the bulk region for the five turbulent Reynolds numbers (grid conditions) are summarized in Table 3.6.

Experiment Series	$Re_T$	Air pressure (mbar)	Initial $C_b$ (mg/l)	Final $C_b$ (mg/l)	Initial $T$ ( $^{\circ}\text{C}$ )	Final $T$ ( $^{\circ}\text{C}$ )
Cb1	260	994	0.91	1.51	17.4	18.2
Cb2	390	991	0.92	1.71	18.3	19.1
Cb3	520	991	0.79	1.70	19.2	19.9
Cb4	650	985	0.74	1.85	19.0	20.1
Cb5	780	985	0.62	1.95	20.2	21.5

**Table 3.6.** Experimental conditions in the Cb-Series

## 4. Evaluation of turbulence characteristics in the present grid-stirred tank

Before performing the gas transfer experiments in the grid-stirred tank, it is essential to evaluate the turbulence characteristics generated by the oscillating grid. In the present study, the results were compared with the data from previous works with similar grid construction (e.g. Hopfinger & Toly (1976), Thompson & Turner (1975), McDougal (1979), Brumley & Jirka (1987) and Cheng & Law (2001)) that allow direct comparison of the turbulence characteristics produced in the present grid-stirred tank system. The flow-fields in the test tank with varying turbulence intensity levels were measured in the Vb-series experiments. The experimental program and procedures have been described in detail in Section 3.5.1. In this chapter, the results are presented and discussed.

### 4.1 Velocity fluctuations

As mentioned in Section 3.5.1, the instantaneous flow-fields were measured using the PIV technique. One PIV image window covered an area of approximately  $7 \times 9 \text{ cm}^2$ . From each window, a velocity vector map consisting of  $80 \times 64$  vectors was obtained using an interrogation area of  $32 \times 32$  pixels with 50% overlap. A schematic illustration of the coordinate convention used for the discussion of the bulk turbulence measurements is depicted in Figure 4.1. The vertical axis ( $z_{cs}$ ) indicates the vertical distance from the centre of the stroke or the centre of the grid position. The origin of the horizontal axis ( $x$ ) is located at the side wall of the tank. Two successive instantaneous vector maps randomly chosen from Exp. Vb5 are shown in Figure 4.2. In the figure, only every second vector is shown to avoid congestion.

For each turbulence intensity level, measurements were performed at several imaging windows by shifting the camera along the vertical axis to cover the extensive range from near the grid up to approximately 3 to 5 cm below the water surface. The time-averaged velocity fluctuations  $u'$  and  $w'$  are the root-mean-squared values from the 450 (Vb1 to Vb3) or 900 (Vb4 to Vb5) instantaneous velocity maps

$$u' = \sqrt{\overline{u^2}} \quad (4.1)$$

$$w' = \sqrt{\overline{w^2}} \quad (4.2)$$

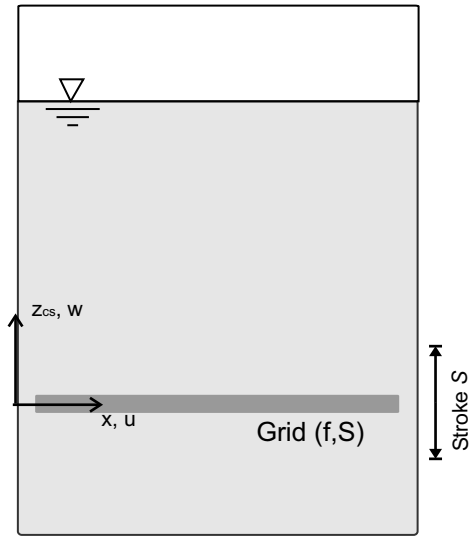


Figure 4.1. Coordinate convention used for the discussion of the bulk turbulence measurements

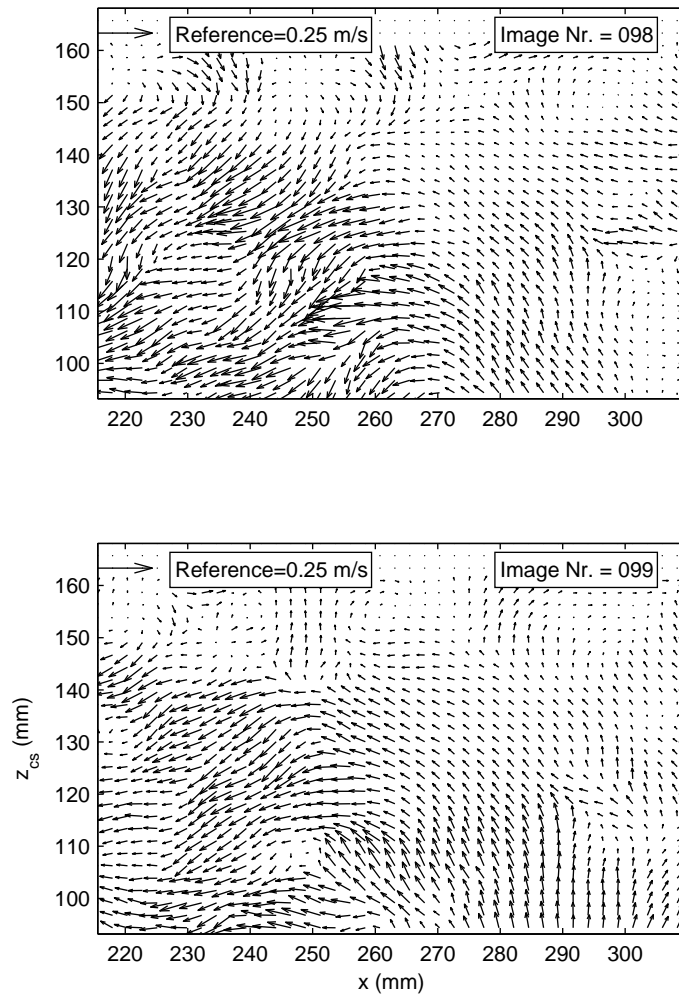


Figure 4.2. Example of two successive instantaneous vector fields (selected from Vb5)

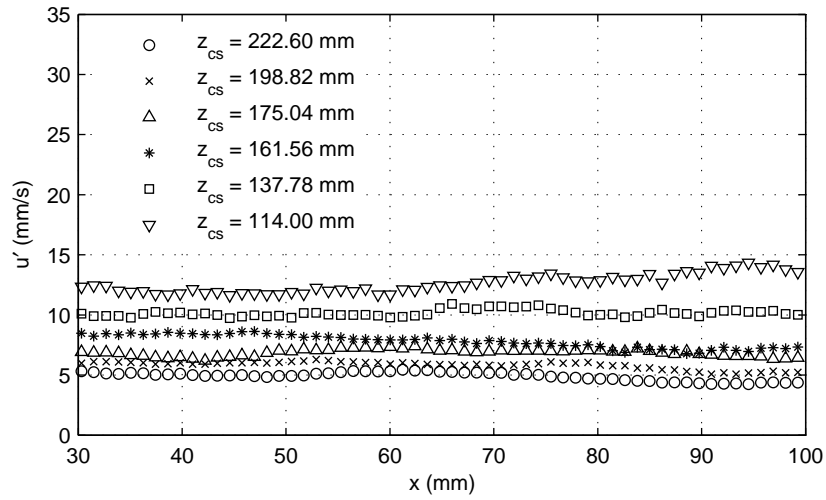
where  $u$  and  $w$  are the fluctuating parts of the instantaneous velocity vectors as defined in Eq. 2.3.

Figure 4.3 shows the typical horizontal variation of the the time-averaged turbulence characteristics produced by the grid-stirred tank at selected elevations. The values of  $u'$  and  $w'$  shown in Figure 4.3a and b represent the data obtained in Vb4. The horizontal variation obtained in the other experimental series (Vb1, Vb2, Vb3 and Vb5) are similar in trend (not magnitude) and can be explained as follows. It can be observed that the horizontal variation nearer to the grid are still inhomogeneous as indicated by the strong fluctuation of the  $u'$  and  $w'$  measured at  $z_{cs}= 114$  to 161 mm. Further away from the grid, the values are nearly constant. The transition from inhomogeneity near the grid to homogeneity further away from the grid agrees with the observation by Cheng & Law (2001) who found that the horizontal homogeneity only started at least three mesh sizes away from the centre of the stroke.

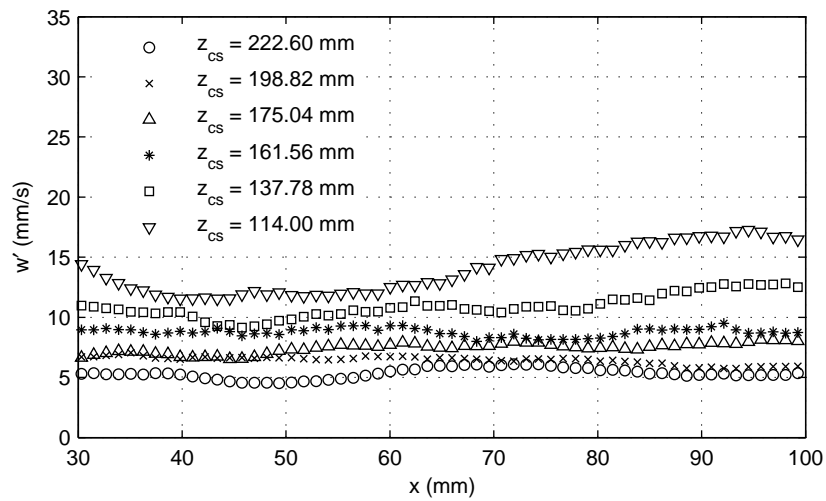
The decay of both the horizontal and vertical turbulence fluctuations ( $u'$  and  $w'$ ) with distance from the grid for the different turbulent Reynolds numbers  $Re_T$  are presented in Figures 4.4a and b, respectively. The profiles were obtained from further spatially averaging the time-averaged turbulence characteristics over the horizontal direction at each elevation. With the present measurement resolution, data points could be acquired at every 1.1 mm. However, to avoid congestion, only every third data point measured in the experiments are shown.

To evaluate the turbulence characteristics produced in the present grid-stirred tank system, the empirical relation of the turbulence decay (Eq. 2.22) proposed by Hopfinger & Toly (1976) is also included in Figure 4.4 as solid lines. As can be observed, the decay of the horizontal velocity fluctuations are in very good agreement with the relation proposed by Hopfinger & Toly (1976). The best-fitted  $c$  values of Eq. 2.22 for each  $Re_T$  are indicated in the legend of the graph. The  $c$  values range from 0.20 to 0.23 and were in close agreement to 0.25 which was given by Hopfinger & Toly (1976). The Hopfinger-Toly relation is only valid for unbounded conditions and therefore is no longer valid near the interface. The discussion in this chapter only considers the turbulence measurements in the bulk region. Further discussion on the velocity fluctuation measurements near the surface is given in Section 5.3.

To examine further the horizontal homogeneity of the velocity fluctuations in the tank, the temporally and then spatially averaged  $u'$  and  $w'$  profiles obtained from Exps. Vb1 (image acquisition at the centre of the tank) and Vb3 (image acquisition near the side wall of the tank) are plotted in Figure 4.5a and b, respectively. A plan view of the image acquisition windows in Vb1 and Vb3 has been given in Figure 3.13. As can be observed



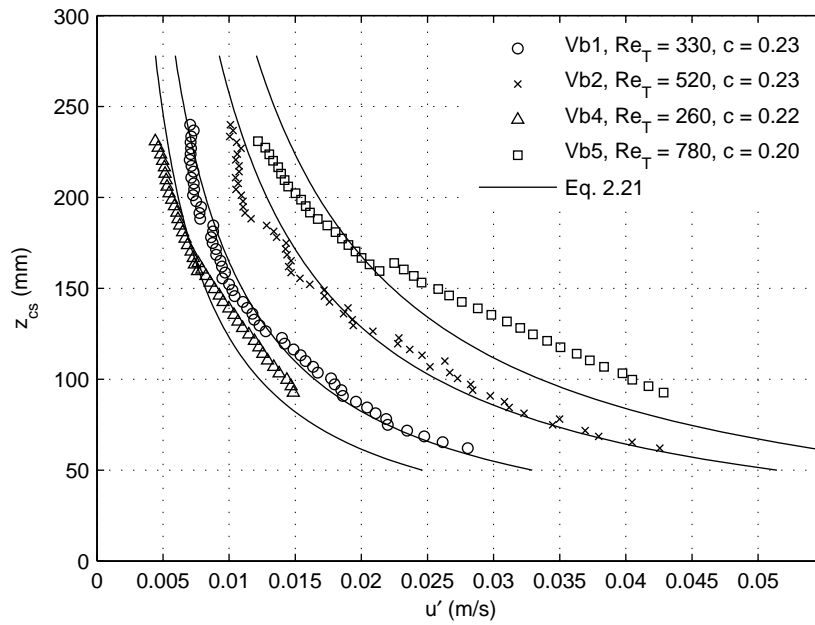
(a) horizontal fluctuations



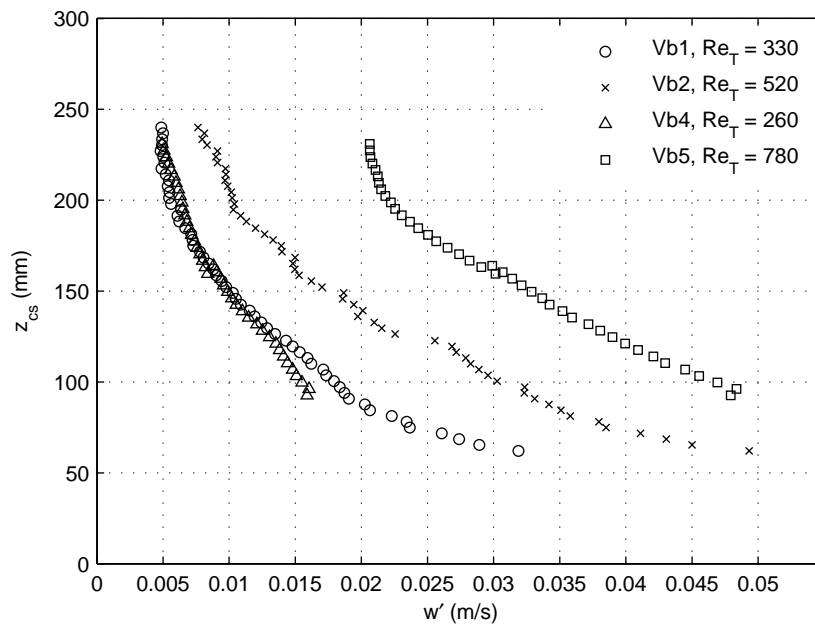
(b) vertical fluctuations

**Figure 4.3.** Distribution of velocity fluctuation at selected elevations from Vb4. (a) horizontal fluctuations (b) vertical fluctuations

in Figure 4.5a and b, the distribution of the turbulence fluctuations from Vb1 and Vb3 are in very good agreement. This result together with the result deduced from Figure 4.3 further proves the horizontal homogeneity of the turbulence generated in the present test tank.



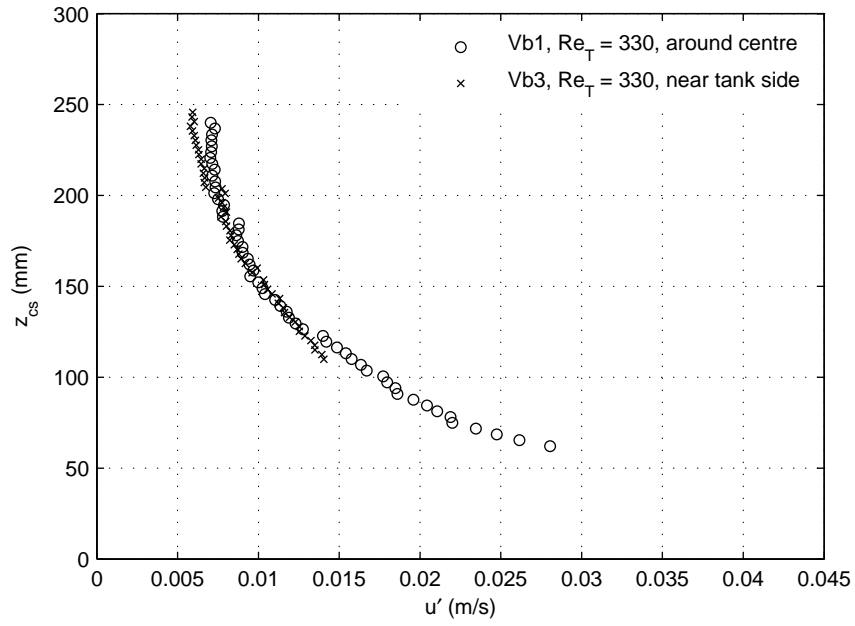
(a) horizontal fluctuation



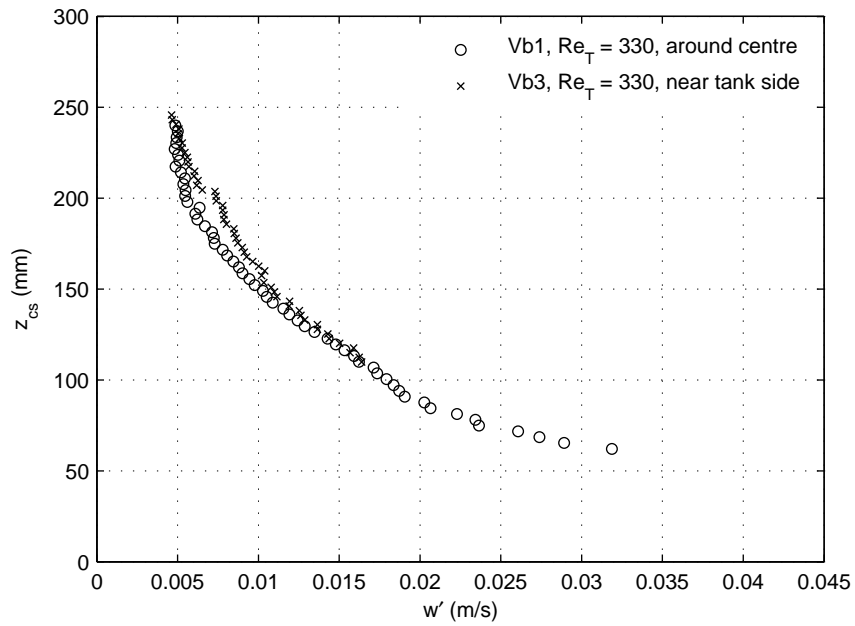
(b) vertical fluctuation

**Figure 4.4.** Temporally and spatially averaged turbulence velocities showing the decay of turbulence intensity with distance from the grid as a function of different turbulence conditions. (a) horizontal components  $u'$  (b) vertical components  $w'$





(a) horizontal fluctuation



(b) vertical fluctuation

**Figure 4.5.** Temporally and spatially averaged turbulence velocities at the centre and near the side wall of the tank. (a) horizontal fluctuations  $u'$ ; and (b) vertical fluctuations  $w'$

## 4.2 Integral length scales

An advantage of the PIV technique is that the velocity vectors within the planar measurement window are acquired simultaneously. This allows direct computation of the spatial cross-correlation of the velocity fluctuations over the imaged area. The longitudinal and transversal cross-correlation coefficients, following Tennekes & Lumley (1972), are defined as

$$R_{uu,x}(\zeta_x) = \frac{\overline{u(0)u(\zeta_x)}}{\overline{u^2(0)}} \quad (4.3)$$

$$R_{ww,x}(\zeta_x) = \frac{\overline{w(0)w(\zeta_x)}}{\overline{w^2(0)}} \quad (4.4)$$

with  $\zeta_x$  is the distance of the lags in the x-direction,  $R_{uu,x}$  and  $R_{ww,x}$  the longitudinal and transversal correlation functions, respectively.

As an example, the longitudinal and transversal correlation coefficients computed for Exp. Vb4 are shown in Figure 4.6. The correlation coefficients are plotted as a function of the lags  $\zeta_x$ . It can be observed that the area under the curve of the correlation functions increase with further distance from the grid.

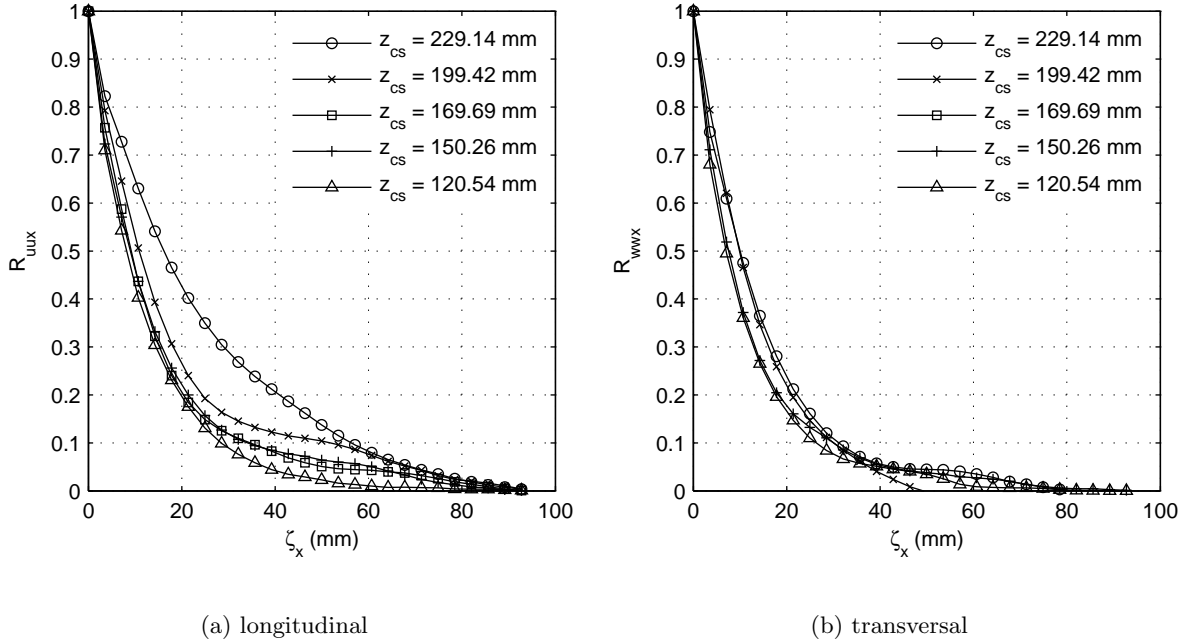


**Figure 4.6.** Correlation-coefficients as a function of  $\zeta$  at selected  $z_{cs}$  levels from Exp. Vb4 : (a)longitudinal (b)transversal

The area under the correlation functions up to the first zero intercept can be interpreted as the integral length scale. Hence, the longitudinal and transversal integral length scale can be computed with the following equations :

$$L_u = \int_0^\infty R_{uu,x}(\zeta) d\zeta \quad (4.5)$$

$$L_w = \int_0^\infty R_{ww,x}(\zeta) d\zeta \quad (4.6)$$

in which  $L_u$  and  $L_w$  denote the longitudinal and transversal integral length scales, respectively. The computed integral length scales are presented in Figure 4.7 and they clearly grow with distance from the grid. Thompson & Turner (1975) found that the growth of the longitudinal integral length scale  $L_u$  is proportional to the distance from the grid with a constant factor of approximately 0.1. Figure 4.8 shows the integral length scales estimated in this study that are normalized with  $z_{cs}$  to examine the constant of proportionality. After about three mesh sizes away from the centre of the grid, the constants of proportionality for the longitudinal integral length scale are found to be between 0.08 to 0.1 which are comparable to the value obtained by previous works. The constant of proportionality for the transversal integral length scales indicate that  $L_w$  tend to grow slower than  $L_u$ , except for the case  $Re_T = 780$ .

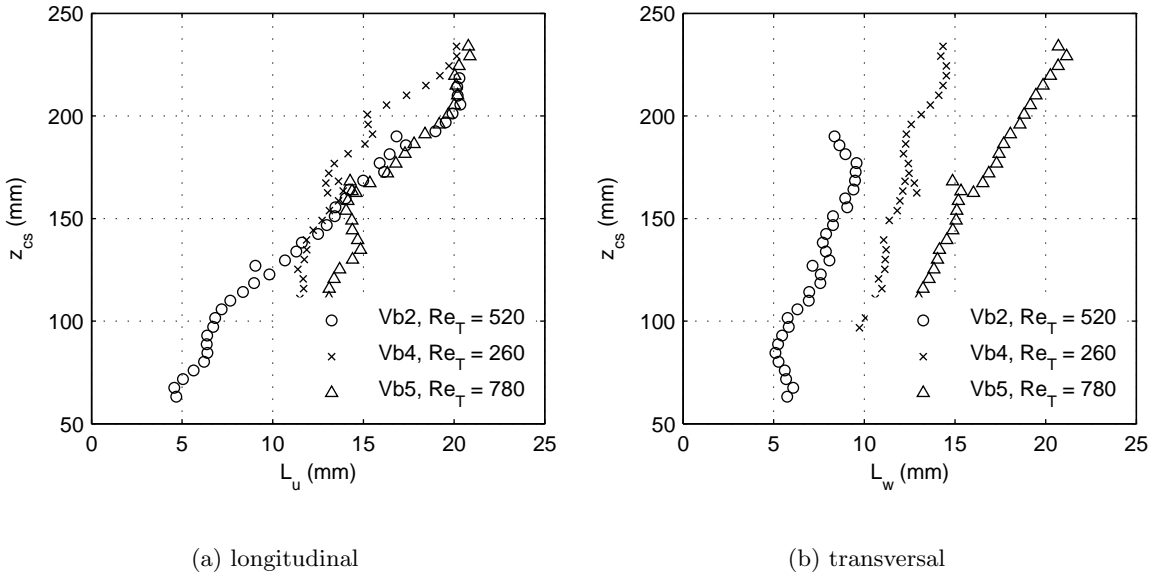


**Figure 4.7.** Variation of the longitudinal and transversal integral length scales of the velocity fluctuations with distance from the centre of the grid

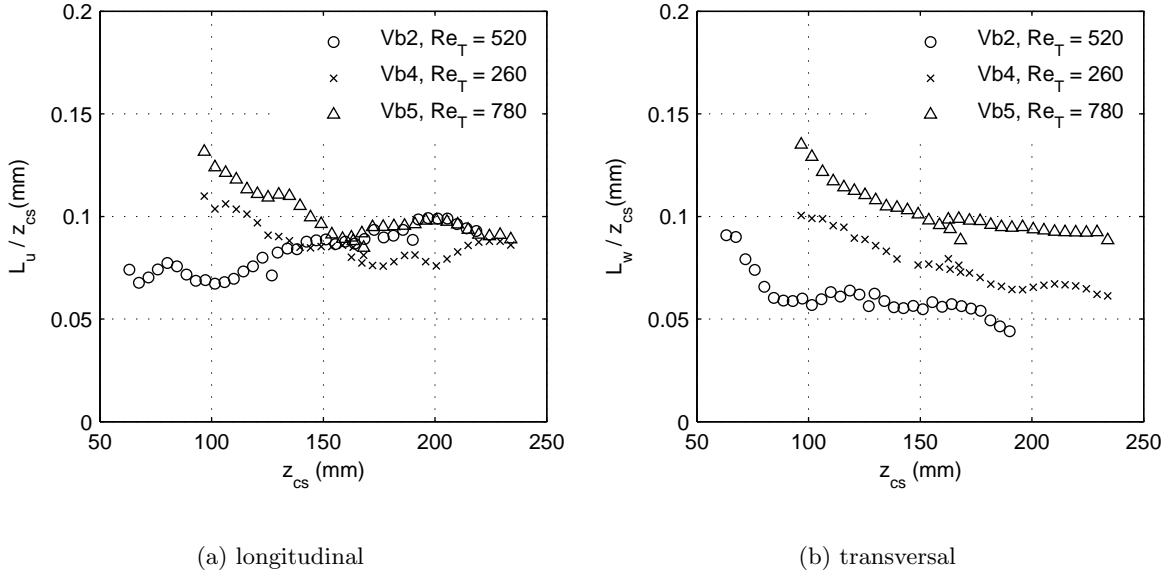


**Figure 4.8.** Variation of the longitudinal and transversal integral length scales of the velocity fluctuations with distance from the centre of the grid

### 4.3 Turbulent kinetic energy

Although the source of turbulence is different, it is still interesting to make a rough comparison between the turbulence intensity level generated by the grid-stirred tank with the one occurring in open-channel or stream flows. For that purpose, the turbulent kinetic energy seems to be the most appropriate measure for the energy produced by the oscillating grid since no mean shear is present in the grid-stirred tank system.

The turbulent kinetic energy  $k$  is defined as

$$k = 0.5 [u'^2 + v'^2 + w'^2] \quad (4.7)$$

The PIV measurements delivered planar and not three-dimensional velocity information, only the  $u$  and  $w$  components were quantified. Fortunately, in the present grid-stirred tank system, the  $v$  component is almost equal to the  $u$  component. Therefore, the turbulent kinetic energy in the tank can be estimated as

$$k = 0.5 [2u'^2 + w'^2] \quad (4.8)$$

For open channel flows, Nezu & Nakagawa (1993) proposed the following relations for the longitudinal, transversal and vertical velocity fluctuations, respectively.

$$\frac{u'}{u_*} = 2.3e^{-z/h} \quad (4.9)$$

$$\frac{v'}{u_*} = 1.67e^{-z/h} \quad (4.10)$$

$$\frac{w'}{u_*} = 1.2e^{-z/h} \quad (4.11)$$

with  $z$  is the depth from the water surface,  $h$  the water depth and  $u_*$  is the bottom-shear velocity which is a common scaling parameter used to characterize stream flows. Substituting Eqs. 4.9 to 4.11 into Eq. 4.7 yields

$$\frac{k}{u_*^2} = 4.76e^{-2z/h} \quad (4.12)$$

Allowing the introduction of a characteristic velocity scale  $u_{*\alpha}$  for the turbulent kinetic energy in the grid stirred tank and incorporating it into the relation of Nezu and Nakagawa, the term  $u_{*\alpha}$  can be estimated as

$$u_{*\alpha} = \sqrt{\frac{k}{4.76e^{-2z/h}}} \quad (4.13)$$

where  $h$  is taken as the distance from the centre of the stroke to the water surface.

The turbulent kinetic energy for the present measurements estimated using Eq. 4.8 is plotted in Figure 4.9. The solid lines in the figure are the relation of Nezu and Nakagawa for open channel flows with the fitted  $u_{*\alpha}$  indicated in the legend of the graph. By allowing the comparison between the magnitude of  $u_{*\alpha}$  generated in the tank with  $u_*$  occurring in streams or open-channel flows, the turbulence levels produced in the tank ( $Re_T = 260$  to  $780$ ) correspond to stream flows with  $u_*$  ranging approximately between  $0.65$  to  $2$  cm/s. Although this is just a crude comparison but it may help to give a sense of how strong the turbulence levels generated in the grid-stirred tank are. Of course, higher values than  $2$  cm/s may occur in nature. However, natural streams with this range of  $u_*$  do exist. For example, the Eaton Nord River in Canada has a typical  $u_*$  value ranging from  $0.5$  to  $1.3$  cm/s (Roy et al. 2004). The levels of turbulence generated in this study covered the low and high turbulent flow-regimes suggested by Theofanus (1984) and so it is expected that a sufficient wide spectrum of turbulent eddies could be investigated.

## 4.4 Spectra

It is interesting to estimate the power spectral density when studying turbulence properties. The power spectral density gives an indication of the energy distribution over various length or time scales. The spectral density function of the horizontal and vertical velocity

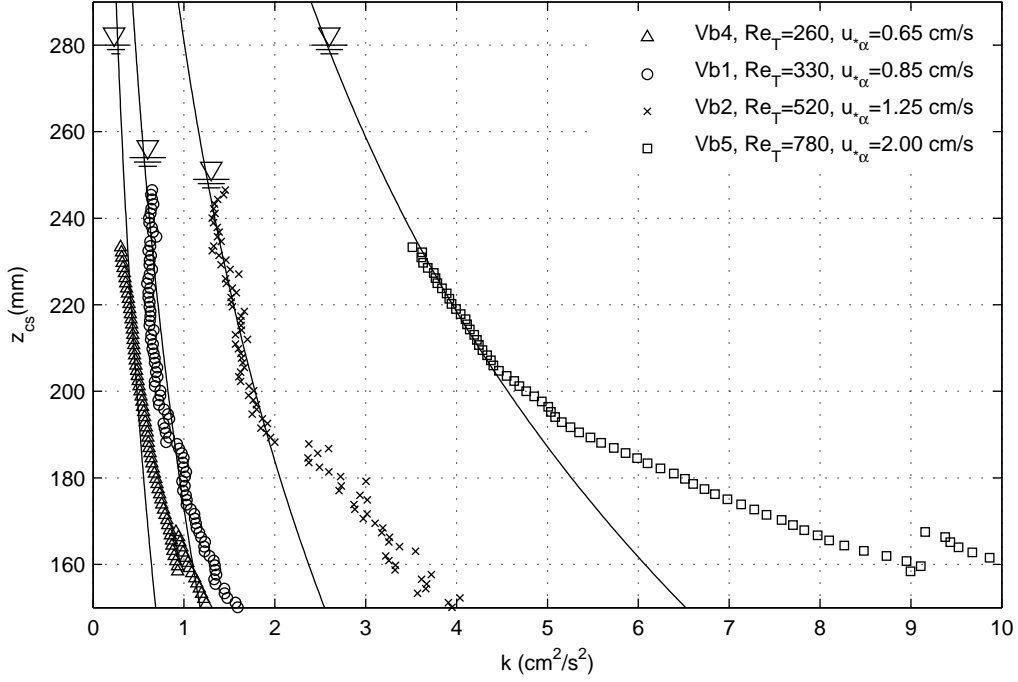


**Figure 4.9.** Measured turbulent kinetic energy  $k$

fluctuations is related to the Fourier transformation of their auto-correlation functions  $R_u$  and  $R_w$ , respectively.

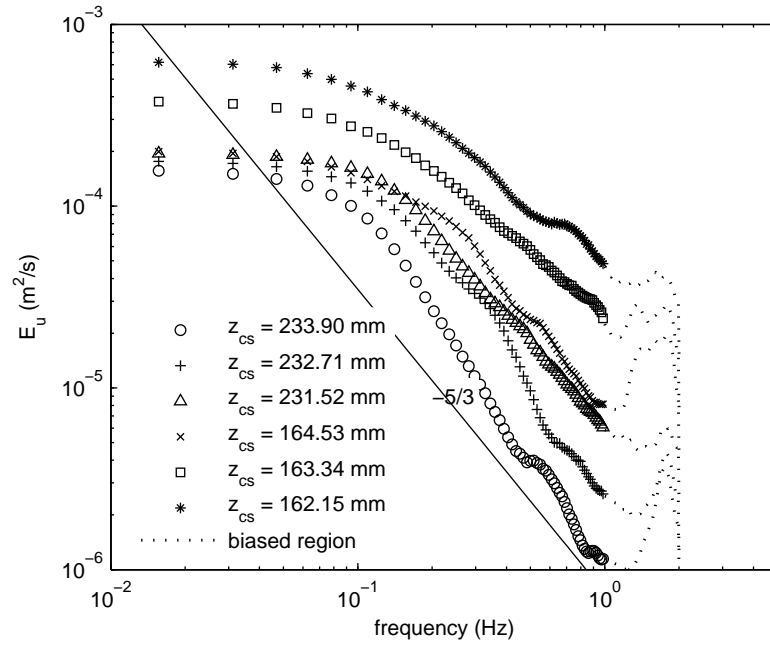
$$E_u(f) = \frac{1}{f_s} \int_{-\infty}^{+\infty} R_u(\tau) e^{-2\pi i f \tau / f_s} d\tau \quad (4.14)$$

$$E_w(f) = \frac{1}{f_s} \int_{-\infty}^{+\infty} R_w(\tau) e^{-2\pi i f \tau / f_s} d\tau \quad (4.15)$$

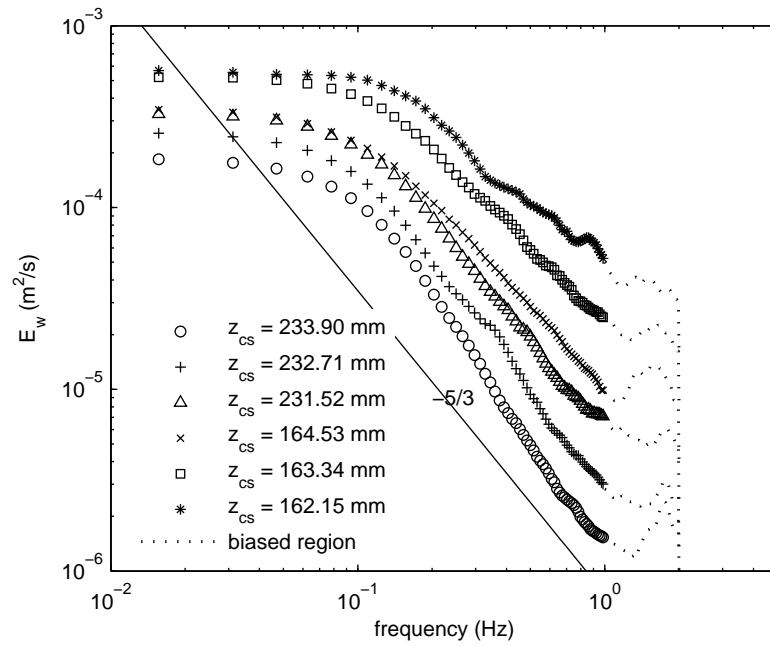
with  $E_u$  and  $E_w$  are the power spectral density functions of the horizontal and vertical velocity fluctuations, respectively and  $f_s$  is the sampling frequency ( $= 4$  Hz in the present study).

The Welch method is used to estimate the power spectral density for the signal analysis in this study. With this method, an array of signals is segmented into several sections of equal length, each with a certain overlap. Welch (1967) specifically recommended the use of a Hamming window with an overlap of 50%. The remaining entries that can not be included into the segments are discarded. The Hamming window is applied on each segment which has the same size (length) as the segment window itself. The detailed discussion on the Welch method is not presented here. Further reading on this topic can be found for example in Marple Jr. (1987).

Figures 4.10 and 4.11 show the power spectral density functions for the lowest and highest grid frequencies operated (measured in Vb4 and Vb5), respectively.

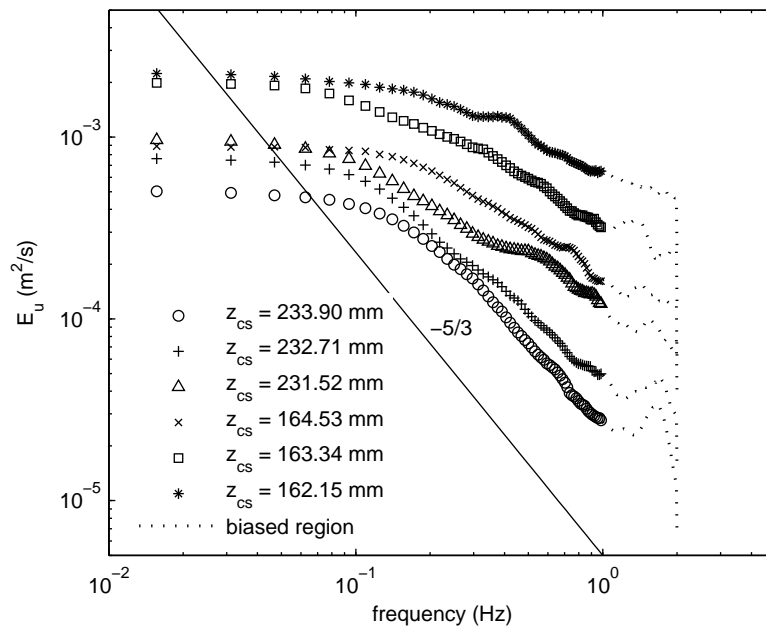


(a) horizontal fluctuation

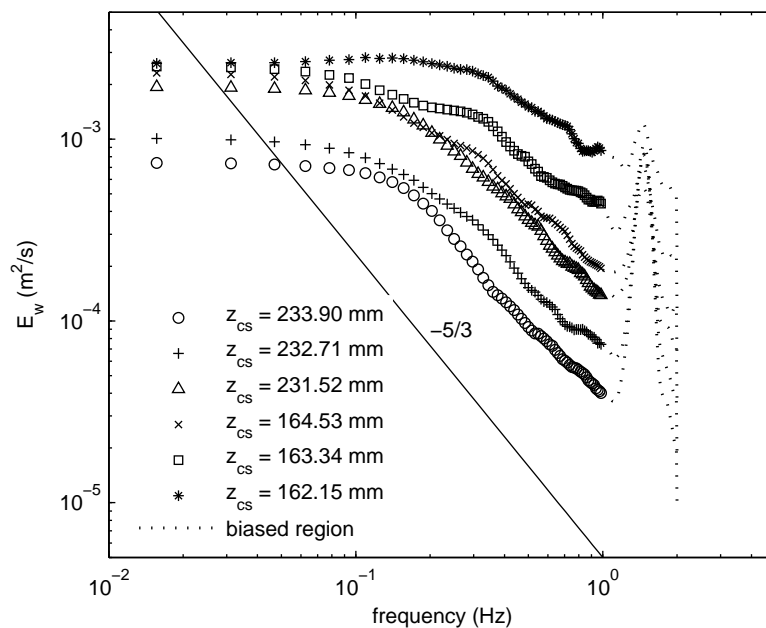


(b) vertical fluctuation

**Figure 4.10.** Spectra of velocity fluctuations at different  $z_{cs}$  levels for  $Re_T = 260$ , water surface is at  $z_{cs} = 280$  mm. (a) horizontal component; and (b) vertical component



(a) horizontal fluctuation



(b) vertical fluctuation

**Figure 4.11.** Spectra of velocity fluctuations at different  $z_{cs}$  levels for  $Re_T = 780$ , water surface is at  $z_{cs} = 280$  mm. (a) horizontal component; and (b) vertical component



In Figures 4.10 and 4.11, the spectra at different distances from the grid centre ( $z_{cs}$ ) are shown. For one selected  $z_{cs}$  level, time series data of  $u'$  and  $w'$  were extracted at 30  $x$  locations from the total of 80  $x$  measured positions. Power spectral densities of the  $u'$  and  $w'$  at each extracted  $x$  location were computed and then ensemble averaged to obtain a representative power spectrum for each selected  $z_{cs}$  level.

The spectra indicate the decay of the turbulent energy with increasing distance from the oscillating grid. The peaks at and around 1-2 Hz observed in the spectra of the velocity fluctuations are caused by the noise related to the grid oscillation frequencies and not to any turbulence production. In the figures, these biased regions are indicated by the dotted lines. If these peaks caused by the noise are ignored, then it can be observed that the spectra for  $z_{cs}$  levels larger than three mesh sizes follow a  $-5/3$  slope. The trend that no peak is found and the energy density monotonically decrease with a  $-5/3$  slope towards higher frequencies characterize a full three-dimensional turbulent flow (see e.g. Townsend 1975). Nearer to the surface the spectra show different behavior as discussed in Section 5.7.1.

## 4.5 Summary of evaluation

In this chapter, the turbulence generated by the grid-stirred tank employed in this study has been evaluated. The evaluation was based on the flow-field measurements extending from near the grid up to 3 to 5 cm below the water surface with the aid of the PIV technique. The decay of the measured turbulence velocity with distance from the grid showed very good agreement with the relation proposed by Hopfinger & Toly (1976). Taking advantage of the simultaneous planar measurements, the integral length scales could be directly estimated using the spatial cross-correlation of the velocity fluctuations. The integral length scales measured were comparable to previous works. An attempt to compare roughly the turbulence intensity level produced in the tank with the one occurring in nature was performed by means of the turbulent kinetic energy and a characteristic velocity scale  $u_{*a}$ . Comparing this term with the bottom-shear velocity  $u_*$  in stream flows, it seems that the turbulence levels produced in the tank ( $Re_T = 260$  to  $780$ ) roughly correspond to stream flows with  $u_*$  ranging between 0.65 to 2 cm/s. The spectral analysis indicate that the turbulence generated by the grid-stirred tank is a full three-dimensional turbulent flow, in the bulk region. Comparison with near surface spectra is given in Section 5.7.1.

Consequently, two important conclusions can be drawn from the results of this evaluation. First, it could be shown that the PIV technique was applicable for measuring the velocity fields in the grid-stirred tank. Second, the turbulence characteristics generated by

the present grid-stirred tank system was verified with previous works. It could be shown that the present grid-stirred tank was a well-controlled system that could generate turbulence with known reproducible scales. Thus, the system is suitable for performing the gas transfer measurements.

In addition, the experiments showed that the undulations at the water surface were typically smaller than  $30 \mu\text{m}$  so that the water surface can be considered as flat at least in the present range of grid frequencies and stroke.

## 5. Results and Discussion

In this chapter, the results of the gas transfer measurements, which were performed in the C,CV and Cb series, are presented and discussed. Each series was performed with varying turbulent Reynolds numbers  $Re_T$  ranging from 260 to 780. The gas transfer process in all series was induced by lowering the dissolved oxygen concentration of the water in the test tank so that a concentration gradient is forced between the interface and the water in the bulk region. The experimental conditions and procedures have been discussed in Section 3.5.2 to 3.5.4. Before moving on to the discussion, a schematic illustration of the coordinate system used in discussing the results of the gas transfer measurements is shown in Figure 5.1 for clarity. The horizontal axis  $x$  indicates the distance from the side wall and the vertical axis  $z$  indicates the depth from the water surface.

### 5.1 Qualitative observations of instantaneous concentration fields

As stated previously, variations of the oxygen concentration near the interface were measured using the Laser Induced Fluorescence (LIF)-oxygen quenching technique. Besides being non-intrusive, the advantages of this method compared to point based measurements are the high spatial resolution and the instantaneous measurement of 2D concentration fields. This possibility of visualizing planar concentration fields is very useful in gaining more insight of the gas transfer mechanisms as discussed in the following paragraphs.

Figures 5.2 and 5.3 show two sequences of 12 instantaneous concentration fields. The dark and light color scaling in the images correspond to the regions with high and low oxygen concentration, respectively. Therefore, the following general description for all images is expected. The darkest layer occurs at the water surface where the oxygen concentration reaches saturation. In the vicinity of the interface, a very thin dark layer indicating the boundary layer in which the oxygen concentration decreases rapidly from saturated to the bulk concentration can be observed. Below this boundary layer, the images are dominated with light color corresponding to the low oxygen concentration in the bulk region that is constantly being mixed by the turbulence generated by the oscillating grid.

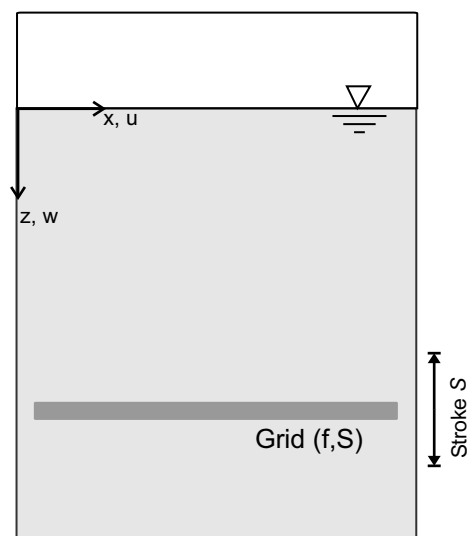
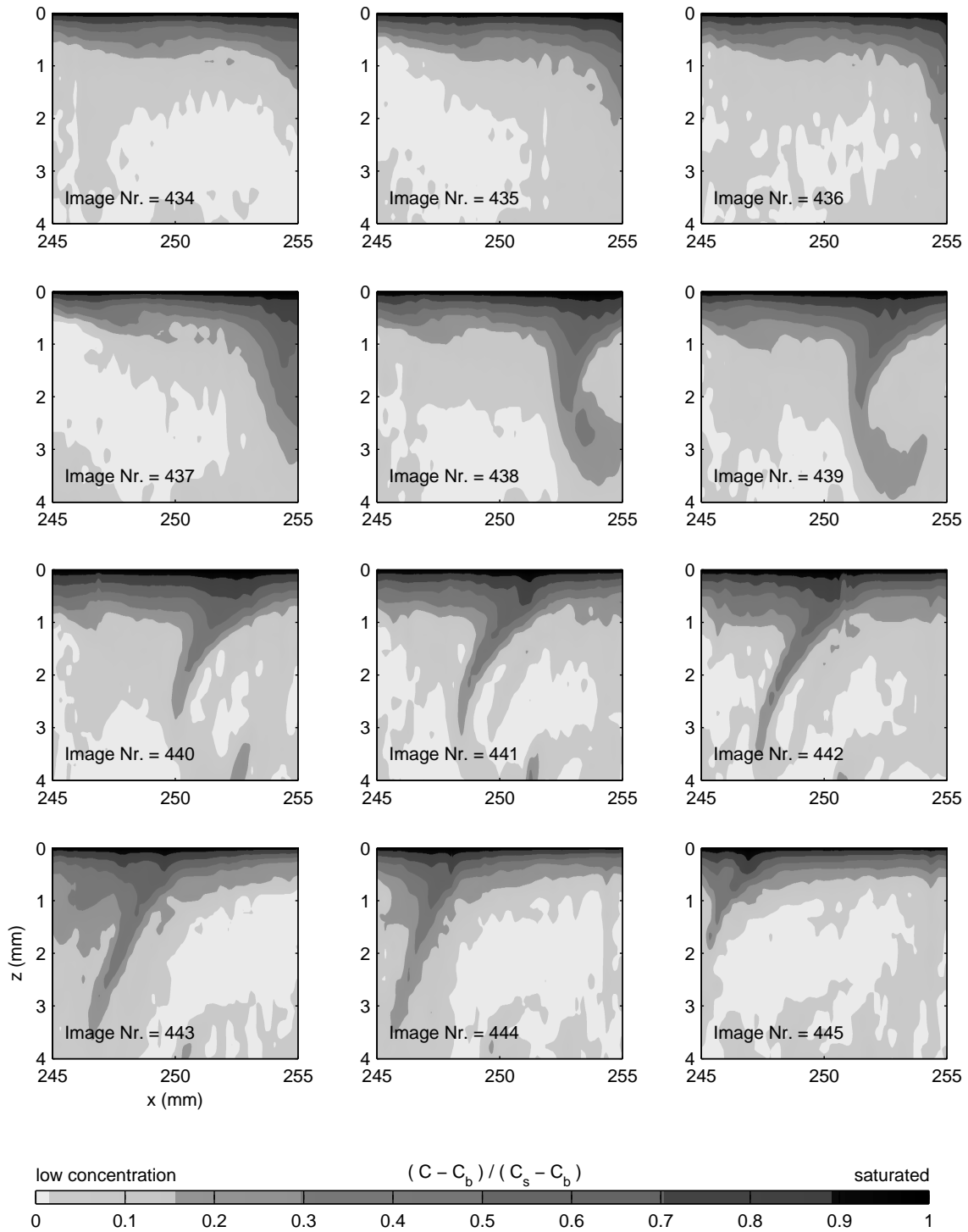


**Figure 5.1.** Schematic illustration of the coordinate system used in discussing the results of the gas transfer measurements

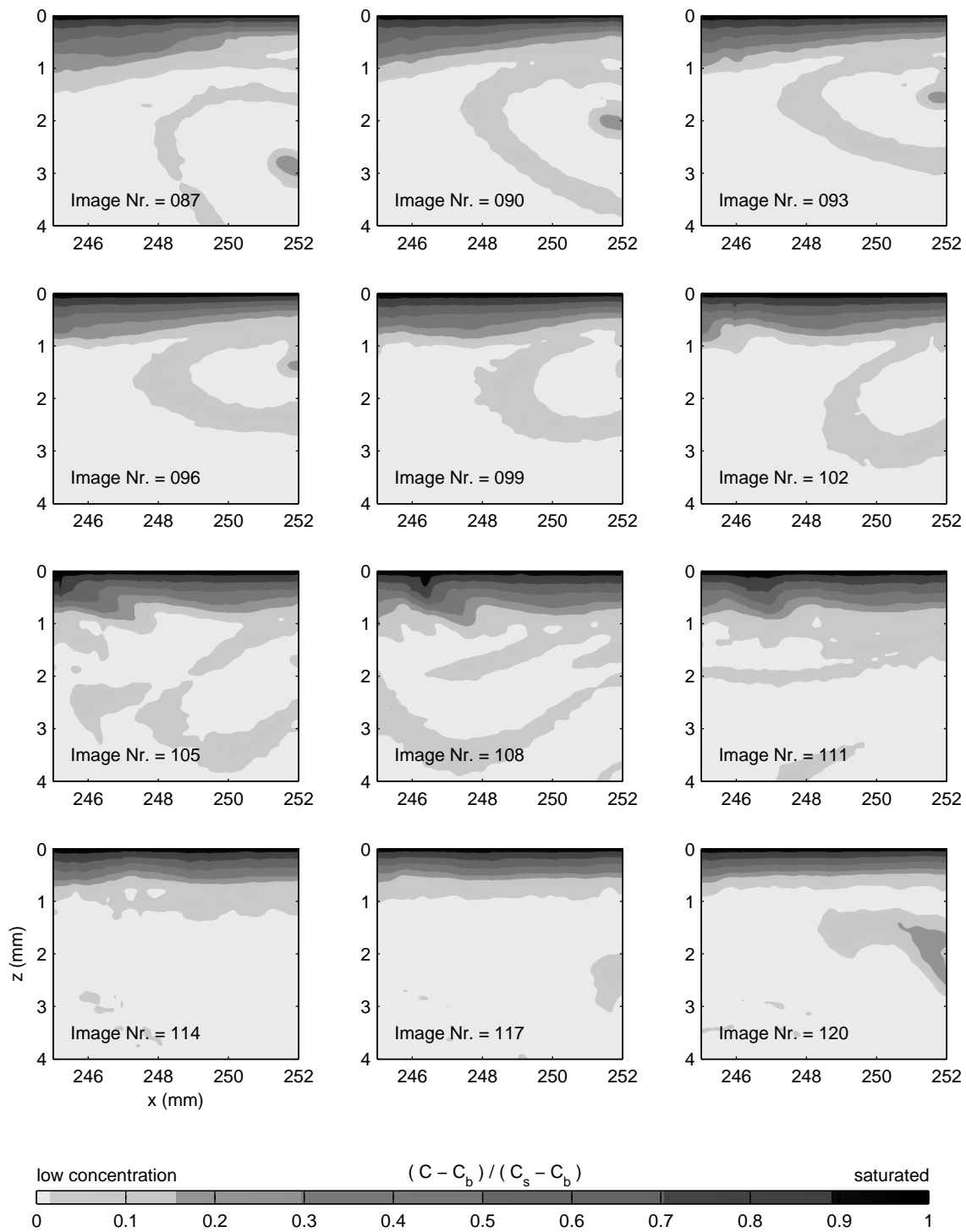
It is interesting to observe the turbulent actions occurring in the instantaneous images. Figures 5.2 and 5.3 show that the turbulence obviously plays a role in the gas transfer process as can be compared to Figure 5.4 which is one typical example of images taken in a quiescent environment (i.e. no grid movements). There were no variation of the local boundary layer thickness and no dark strikes found penetrating the bulk region in all images taken in quiescent environment. This fact ensures that the phenomena visible in Figures 5.2 and 5.3 are indeed the effect of the turbulence and not optical, processing, nor flow artifacts.

Figure 5.2 shows a sequence of images recorded with  $Re_T = 780$  (C5-series). The images were recorded at 4 Hz, thus the time interval between the shown images is 0.25 s apart. A transport process initiated by an eddy structure can be observed in the sequence. The turbulent structure is peeling off portions of the surface layer transporting fluid with higher oxygen concentration into the bulk region (surface renewal events). The presence of turbulence obviously aid the oxygen absorption into the water body. It is observed that the surface renewal events occur several times in all sequences measured with different turbulence levels. The size of the eddy initiating the peeling process shown in Figure 5.2 is obviously larger than the observation window.

The sequence presented in Figure 5.3 is taken from measurements published in Herlina & Jirka (2004). The grid frequency was 3 Hz, the water depth was 473 mm and the water temperature about 10°C. The recording rate was also 4 Hz but only every third image is shown so that the time interval between the shown images is 0.75 s. This particular sequence is presented again here because it represents a good visualization of a turbulent structure approaching the boundary. In the sequence, it can be observed that as soon as the



**Figure 5.2.** A sequence of oxygen concentration contour maps visualizing a peeling process associated to a surface renewal event,  $z = 0$  is the water surface, time interval between shown images is 0.25 s.



**Figure 5.3.** A sequence of oxygen concentration contour maps visualizing a small eddy structure approaching the boundary,  $z = 0$  is the water surface, time interval between shown images is 0.75 s.

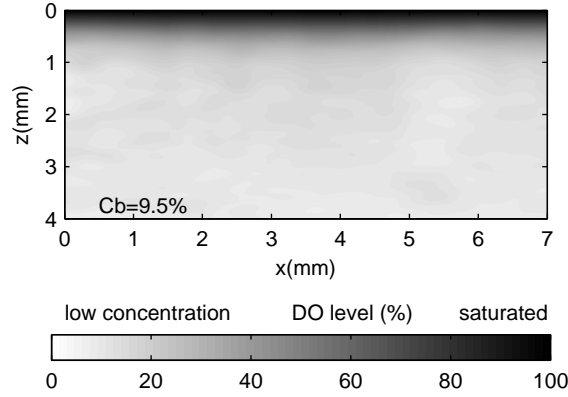


**Figure 5.4.** Typical instantaneous image with no grid movements

structure impinges the water surface (Image Nr. 093), the vertical growth of the structure is inhibited and consequently it undergoes horizontal stretching and finally diffuses.

For comparison purposes, the characteristic length scale of the smallest turbulent eddies, the Kolmogorov scale  $\eta$ , is estimated following Brumley & Jirka (1987) as

$$\eta = 2L_\infty Re_T^{-3/4} \quad (5.1)$$

Based on this equation, the Kolmogorov scale for that sequence is about 0.7 mm. The large structures on the other hand would be theoretically of order integral scale  $L_\infty = 27$  mm. These large structures can not be visualized within the present image field ( $4 \times 5$  mm<sup>2</sup>) that is much smaller than the integral scale size. The eddy captured in Figure 5.3 is therefore of intermediate scale since its size is about 4 mm.

Comparing the observations in Figures 5.2 and 5.3, it seems that both large and small structures contribute to the transfer process.

**Instantaneous concentration profiles.** The oxygen concentration contour maps presented in Figures 5.2 and 5.3 show that the vertical distribution of the oxygen concentration at one  $x$  position may experience enormous changes over time including also in the bulk region outside the boundary layer. Figure 5.5 depicts the vertical concentration profiles extracted from Figure 5.2 at  $x = 248$  mm. The profiles show the occurrence of relatively high concentration in the bulk region (indicated by arrows) which is associated to the peeling process visualized in Figure 5.2.

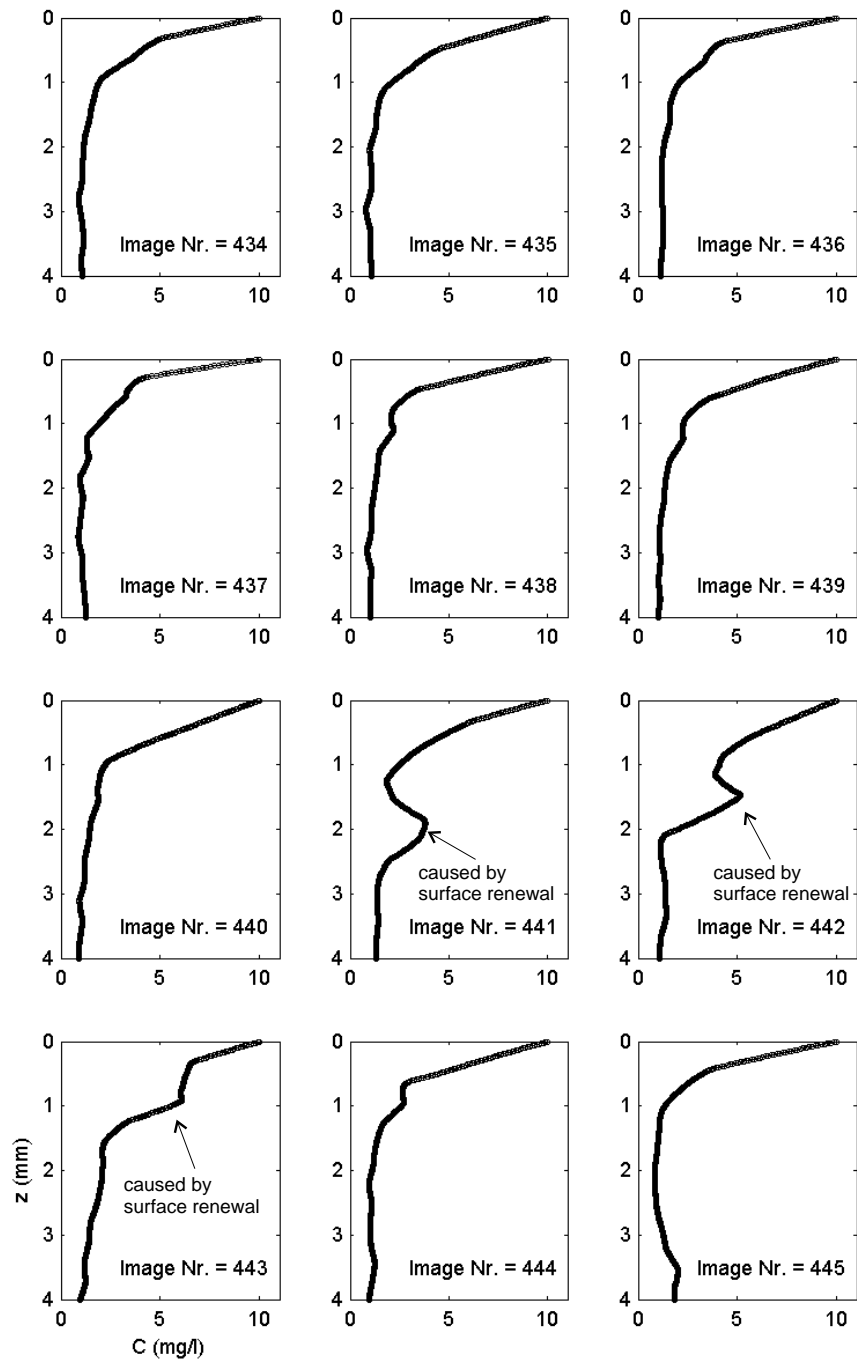


**Figure 5.5.** Instantaneous concentration profiles measured with  $Re_T = 780$  (C5) extracted from Figure 5.2 at  $x = 248$  mm which is approximately at the centre of the recorded image.



## 5.2 Quantitative results : Mean and turbulence characteristics of concentration

The statistical results for the concentration measurements of all five grid conditions measured both with the stand-alone LIF system (C-series) and the combined PIV-LIF system (CV-series) are presented and discussed in this section. The statistical analysis are performed over the 900 instantaneous images acquired in each series. The temporally mean concentration values  $C$  are obtained by ensemble averaging the instantaneous concentration values

$$\bar{c} = \langle c \rangle = \frac{\sum C}{n} \quad (5.2)$$

with  $C$  is the instantaneous concentration and  $n$  the number of samples which is 900 in the present study. The concentration fluctuation  $c'$  is the standard deviation or the root-mean-squared value from the 900 samples.

$$c' = \sqrt{c^2} \quad (5.3)$$

in which  $c$  denotes the fluctuating part of the instantaneous concentration as defined in Eq. 2.3.

The LIF camera has a resolution of 1024 (rows) x 1280 (columns) pixels. However, not the total resolution capacity (whole data points) are taken into account when performing statistical analysis. The information at the edges of the LIF images, namely the first and last 300 columns as well as the last 200 rows, are discarded in order to eliminate the area with low gray scale contrast. Further, the water surface was typically located around 225 to 275 pixels from the top of the recorded images so that about 250 pixels from the top are also not considered in the statistical analysis. Hence, an area of about 500 x 500 pixels from the total 1280 x 1024 resolution capacity has been used in the analysis. The area inside the box in Figure 5.6 depicts the LIF imaged area used in the statistical analysis.

### 5.2.1 Mean and fluctuation profiles

The high spatial resolution of the LIF images enables to elucidate in detail the concentration distribution near the water surface. The mean concentration profiles for all five grid conditions are shown in Figure 5.7. Figure 5.7a represents the mean profiles acquired using the stand-alone LIF system (C-series) and Figure 5.7b represents the data point acquired with the simultaneous PIV-LIF system (CV-series). The mean profiles are obtained by temporally averaging the 900 instantaneous concentration maps and then horizontally averaging the temporally averaged concentration maps. The oxygen concentration in the

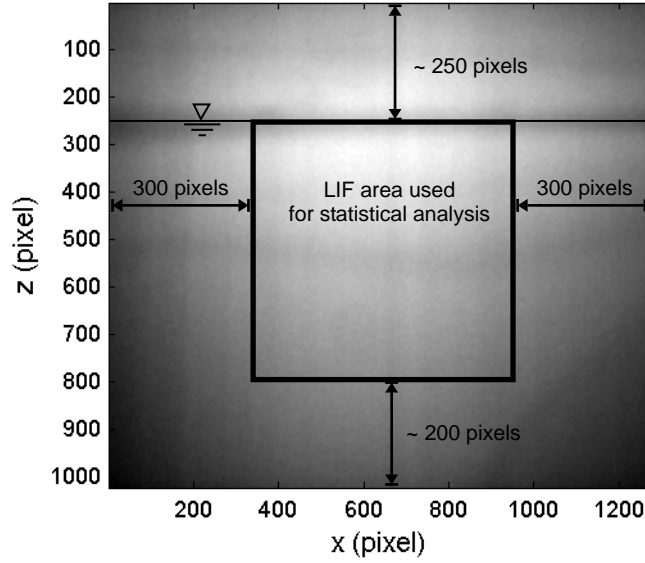
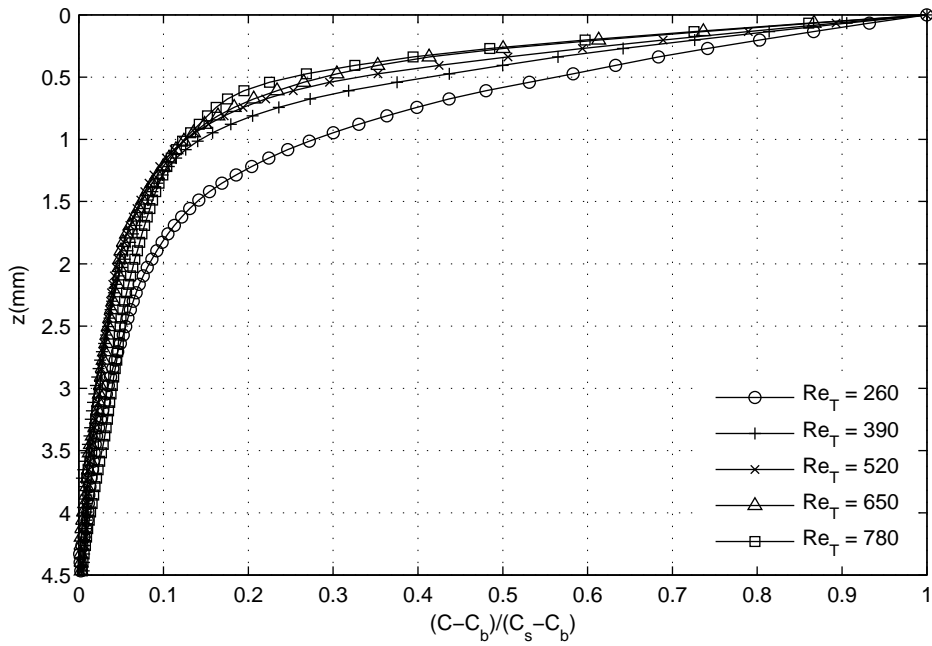


**Figure 5.6.** Illustration of the LIF area used in the statistical analysis

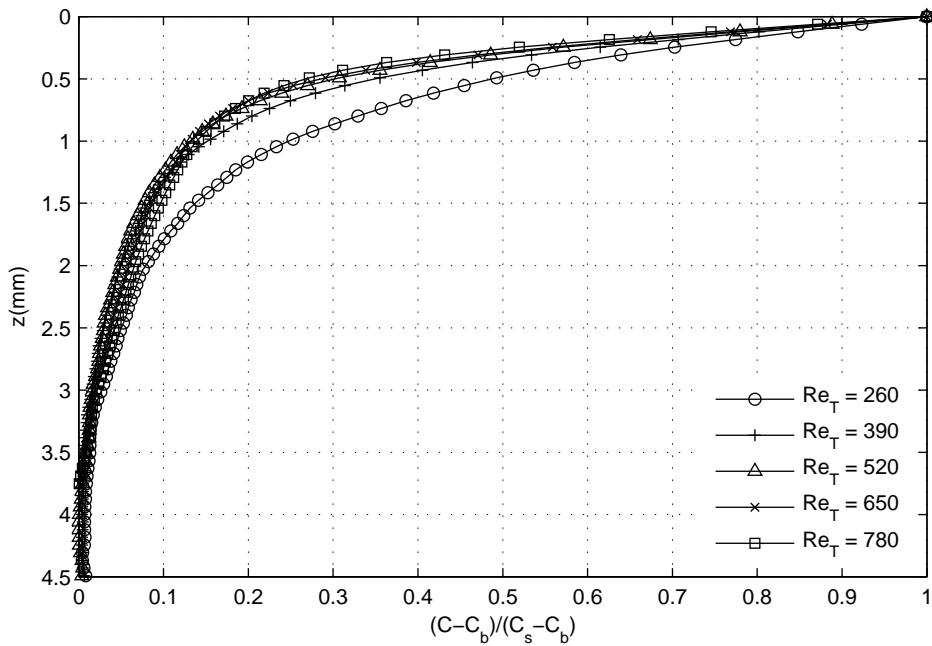
bulk region  $C_b$  and at the interface  $C_s$  differ slightly in each experiment. Therefore, it is convenient to present the concentration in a normalized form  $(C - C_b)/(C_s - C_b)$ . In the graph, only every seventh data point is shown to avoid congestion.

The concentration fluctuation (root mean squared values) profiles for each grid conditions are shown in Figures 5.8a and b for the C-series and CV-series, respectively. In the immediate vicinity below the water surface, the measured concentration fluctuations might be biased due to the optical blurring correction procedure performed in the image processing. The correction was performed with the argumentation that extremely close to the surface any turbulent transport has to vanish and transfer is solely due to molecular diffusion (i.e. a linear concentration distribution) and therefore the blurring effect is corrected by extrapolating the sharpest gradient up to the interface (see Figure 3.9 in Section 3.3. The probably biased data points (the first 10 data points) are purposely left unconnected by the solid lines in order to distinguish them from the unbiased data points.

As mentioned in Section 3.5.2, the reason for performing concentration measurements using the stand-alone LIF system with the same grid conditions as in the simultaneous PIV-LIF measurements was to examine the interference effect of the seeding particles present in the LIF images when applying the combined PIV-LIF system. Comparing the mean concentration profiles obtained from the stand-alone LIF measurements (Figure 5.7a) with the profiles obtained from the simultaneous PIV-LIF measurements (Figure 5.7b), the profiles are similar in trend and magnitude. For improved confidence, the mean profiles from C3 and CV3 are plotted again in one graph in Figure 5.9a. It could be shown that the profiles coincide approximately onto one curve. Little discrepancies in the

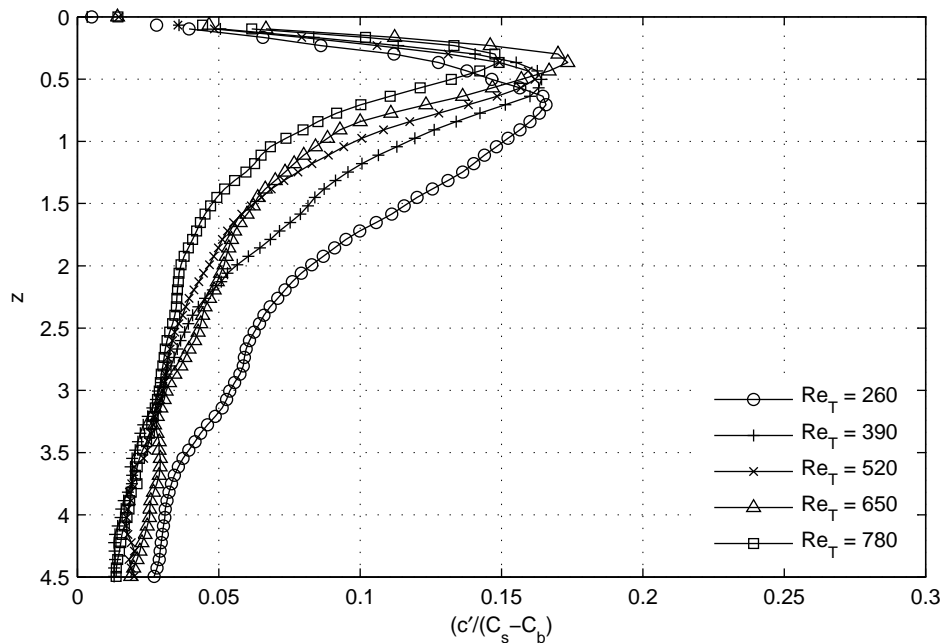


(a) stand-alone LIF

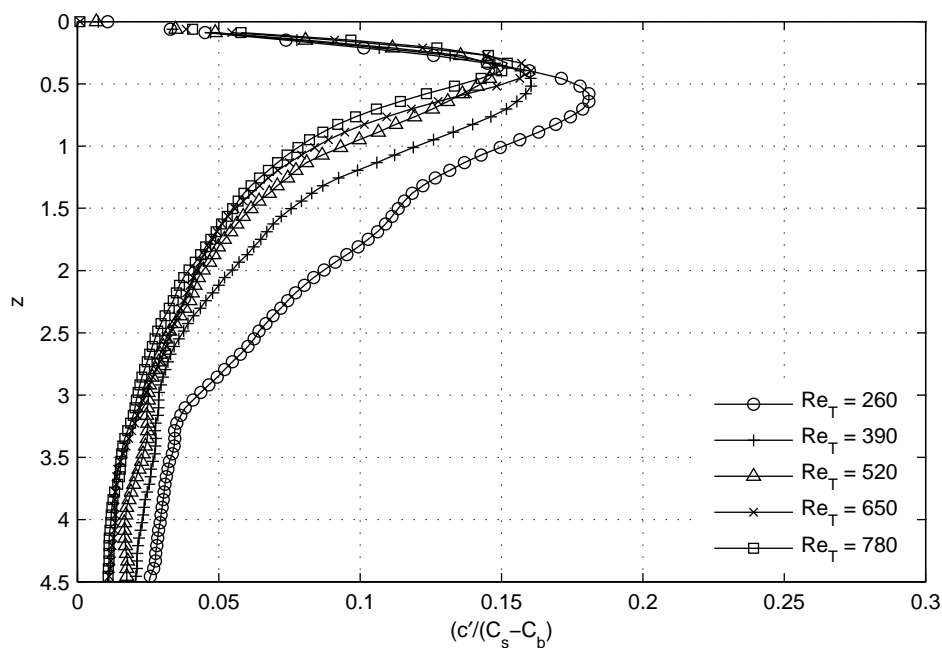


(b) simultaneous PIV-LIF

**Figure 5.7.** Mean concentration profiles obtained from (a) the stand-alone LIF measurements (C-series) and (b) the simultaneous PIV-LIF measurements (CV-series). Only every seventh data point is shown in the graph to avoid congestion.

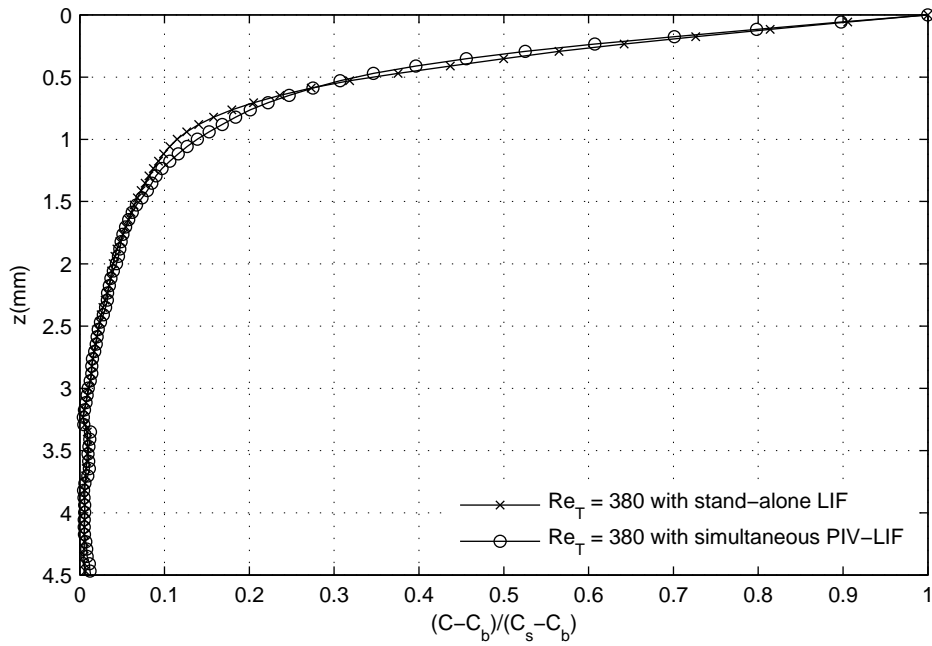


(a) stand-alone LIF

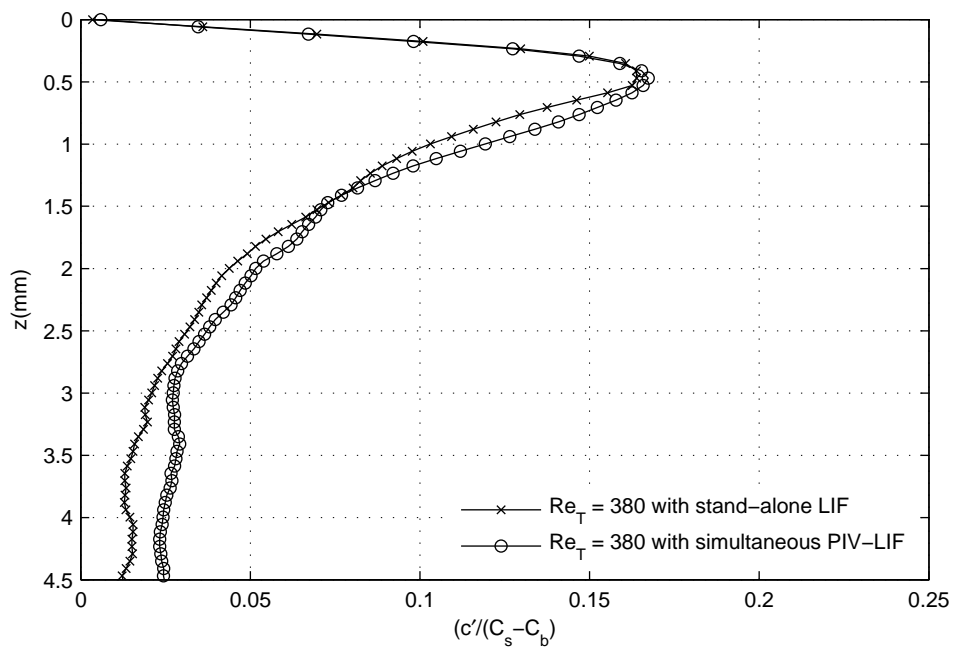


(b) simultaneous PIV-LIF

**Figure 5.8.** Concentration fluctuation profiles, data obtained with (a) stand-alone LIF (C-series) and (b) simultaneous PIV-LIF (CV-series) Only every seventh data point is shown in the graph to avoid congestion. The unconnected data points extremely close to the surface are data points that are probably biased due to the optical blurring correction procedure in the image processing.



(a) mean



(b) fluctuation

**Figure 5.9.** Comparison of concentration profiles obtained using the stand-alone LIF and the simultaneous PIV-LIF for  $Re_T = 380$ . (a) mean profiles (b) fluctuation profiles. Only every seventh data point is shown for clarity.

concentration fluctuation profiles can be observed as shown in Figure 5.9b. However, the discrepancies are not higher than the accuracy of the LIF system itself ( $\pm 5\%$ ). These results ensure that the effect of the particles interference in the LIF images when performing the simultaneous measurements were negligible.

For better interpretation of the mean and fluctuation concentration profiles, it is convenient to present the profiles in a non-dimensional form as will be discussed further in the next sections.

### 5.2.2 Boundary layer thickness

**Definition.** As mentioned above, it is convenient to present the vertical concentration distribution in a non-dimensional form to allow comparison with other experiments despite the different turbulence characteristics. Based on their experimental results, Chu & Jirka (1992) have proposed an exponential function for the normalized mean concentration profiles which can be written as

$$\left\langle \frac{C - C_b}{C_s - C_b} \right\rangle = e^{-z/\delta_e} \quad (5.4)$$

where  $C$  is the instantaneous concentration,  $C_b$  the bulk concentration,  $C_s$  the concentration at the interface and  $\delta_e$  can be interpreted as the measured boundary layer thickness. Looking at Eq. 5.4, the measured boundary layer thickness  $\delta_e$  may thus be defined as the depth ( $z$ ) where the value of the normalized concentration  $(C - C_b)/(C_s - C_b)$  is equal to  $1/e = 37\%$ .

Due to the absence of any turbulent transport through the boundary, Fick's law applies directly at the water surface :

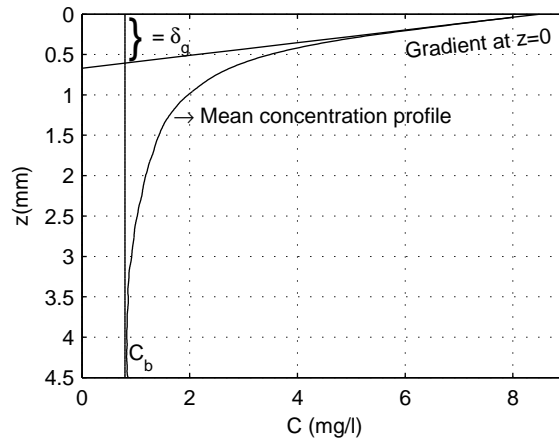
$$j = -D \frac{\partial \bar{c}}{\partial z} \Big|_{z=0} \quad (5.5)$$

From Eqs. 2.6 and 5.5, the boundary layer thickness may alternatively be defined as the intercept between the gradient at the water surface with  $C_b$  as illustrated in Figure 5.10.

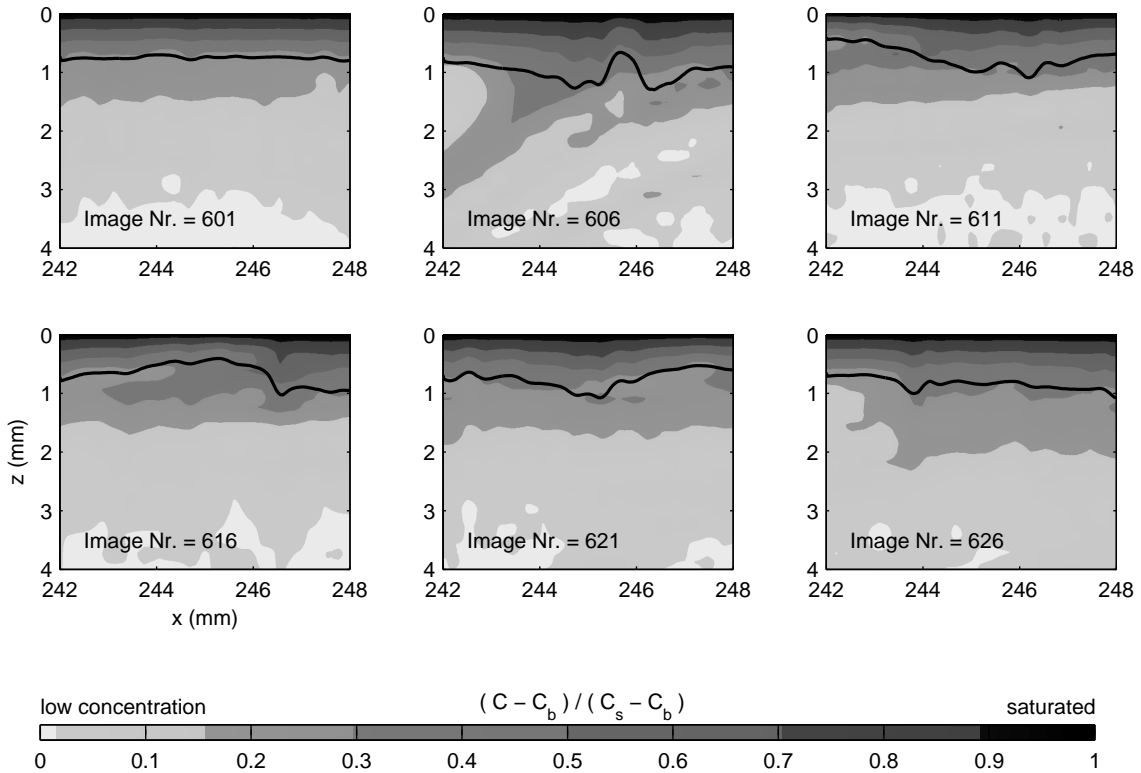
$$\delta_g = \frac{\Delta \bar{c}}{(-\partial \bar{c} / \partial z) \Big|_{z=0}} \quad (5.6)$$

**Variation of local instantaneous boundary layer thickness.** Figure 5.11 depicts six instantaneous concentration images taken from Exp. CV3 ( $Re_T = 520$ ) with the solid line showing the local and instantaneous boundary layer  $\delta_g$ . The sequence shows that the boundary layer at one instant varies with space due to the turbulence structure impinging on the air-water interface.

The local boundary layer thickness at one particular point also changes with time. For example, the temporal variation of the boundary layer thickness at one point from Exp.

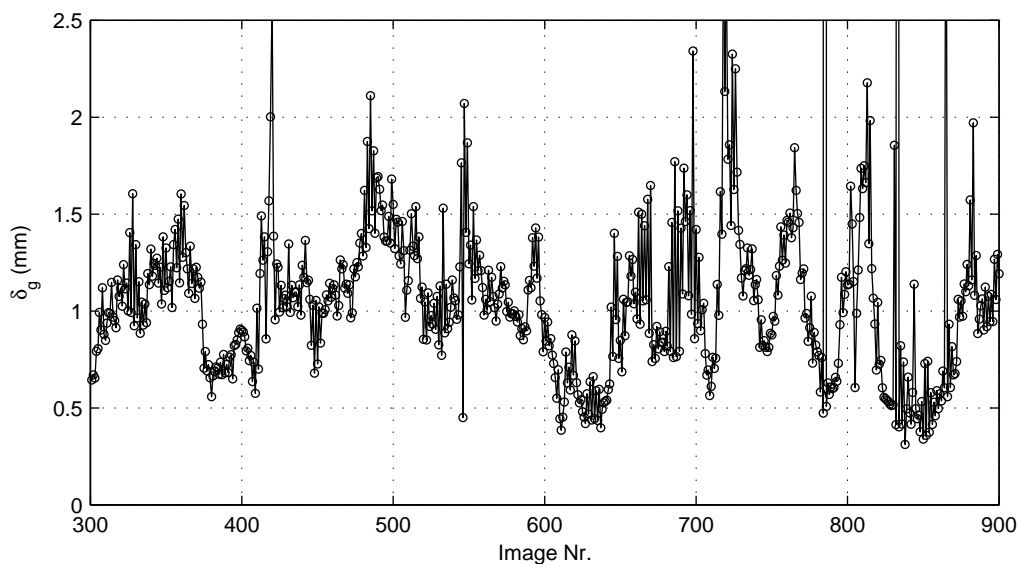
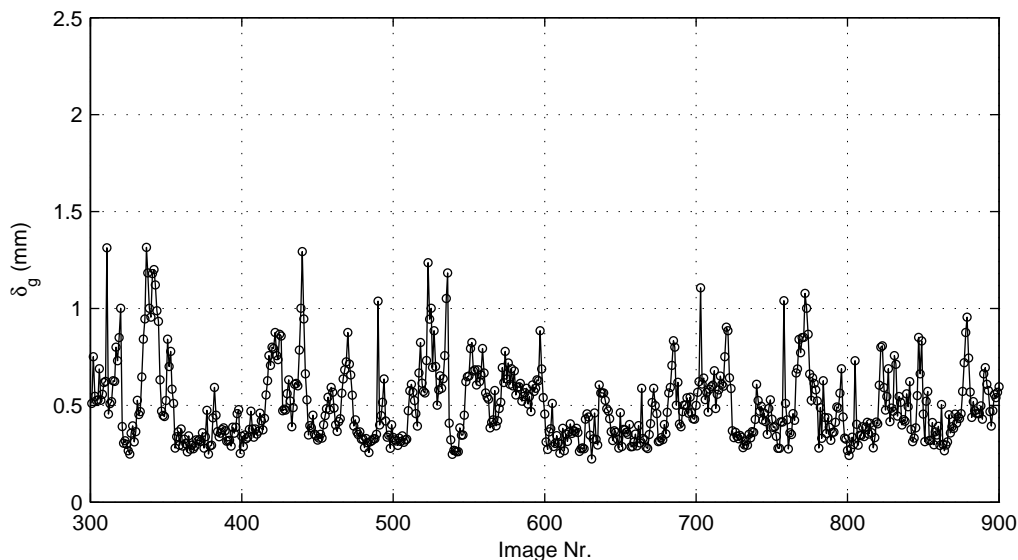


**Figure 5.10.** Illustration of the boundary layer thickness defined based on the steepest gradient at the water surface ( $\delta_g$ )



**Figure 5.11.** Instantaneous concentration images and the boundary layer, showing the boundary layer thickness variation in space and time

C1 and C5 are shown in Figure 5.12a and b, respectively. Figure 5.12a represents the temporal variation for measurements with the lowest  $Re_T$  whereas Figure 5.12b with the highest  $Re_T$ . The boundary layer thickness fluctuates with time and is obviously thinner when the level of turbulence intensity is higher leading to a higher transfer rate.

(a)  $Re_T = 260$ (b)  $Re_T = 780$ 

**Figure 5.12.** Time-series of local boundary layer thickness. (a)  $Re_T = 260$  and (b) with  $Re_T = 780$ . The magnitude of the boundary layer thickness is smaller when the turbulence intensity is higher.



**Mean boundary layer thickness.** The mean boundary layer thickness based on the two definitions explained above ( $\delta_e$  and  $\delta_g$ ) for the present experimental conditions are summarized in Table 5.1 and plotted against the turbulent Reynolds number in Figure 5.13. As already interpreted from 5.12a and b, Figure 5.13 also shows that the boundary layer thickness is limited by higher turbulence intensities. The thickness is suppressed from about  $800\mu\text{m}$  for  $Re_T = 260$  to  $300\mu\text{m}$  for  $Re_T = 780$ .

$Re_T$	$\delta_g$ ( $\mu\text{m}$ ) C-series	$\delta_g$ ( $\mu\text{m}$ ) CV-series	deviation $\delta_g$ %	$\delta_e$ ( $\mu\text{m}$ ) C-series	$\delta_e$ ( $\mu\text{m}$ ) CV-series	deviation $\delta_e$ %
260	865	806	6.8	697	729	4.5
390	618	602	2.5	470	466	0.9
520	549	546	0.5	395	413	4.6
650	503	520	3.4	387	396	2.3
780	473	473	0.0	357	360	0.8

**Table 5.1.** Measured boundary layer thickness

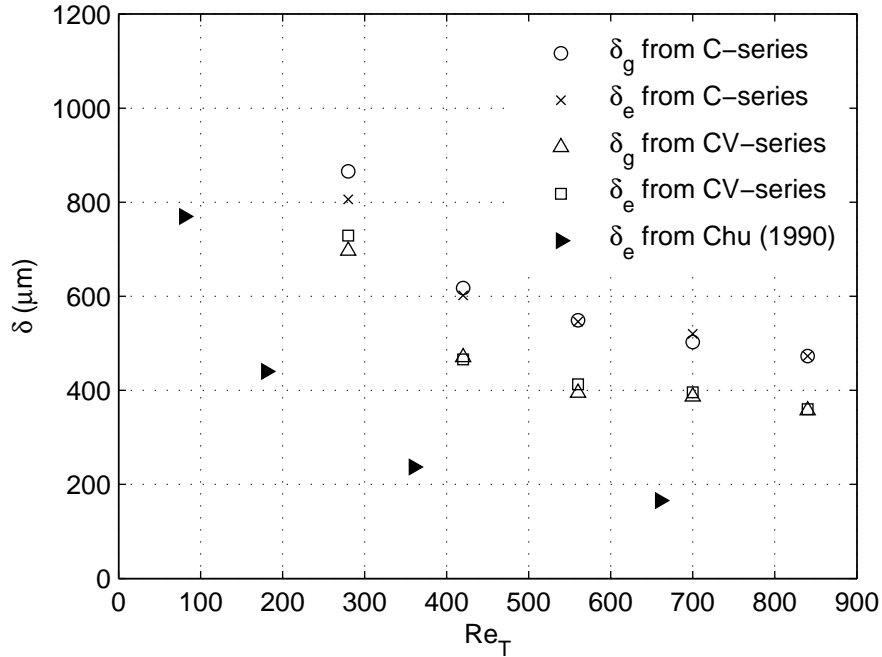


**Figure 5.13.** Measured boundary layer thickness

For comparison, the data from Chu (1990) are incorporated in Figure 5.13. The boundary layer thickness measured by Chu (1990) were smaller compared to the present study although the turbulence generation and the definition of the turbulent Reynolds number  $Re_T$  are the same. Besides the measurement techniques used, the only difference in the

experiments was the distance from the centre of the grid to the water surface ( $z_s$ ). In Chu (1990) experiments,  $z_s$  was between 240-245 mm whereas in the present study  $z_s$  varied between 280-290 mm. Assuming that the discrepancy introduced by the differences in the measurement techniques is small, it is expected that the approximately 5 cm differences in  $z_s$  is large enough for the turbulence to decay (weaken) significantly so that the energy for suppressing the aqueous boundary layer in the present study is lower leading to a thicker boundary layer as compared to Chu (1990). The influence of  $z_s$  is not represented in the turbulent Reynolds number ( $Re_T = u_{HT}2L_\infty/\nu$ ). The term  $z_s$  in  $u_{HT}$  and  $L_\infty$  cancel out each other so that  $Re_T$  (with the same grid frequency, stroke and mesh size) stays constant although  $z_s$  is varied. Thus, the usage of  $Re_T$  in order to characterize the different turbulence levels for the gas transfer process in a grid-stirred tank is only appropriate when  $z_s$  has approximately the same value in the different experiments. Alternatively, the square root of the interfacial kinetic energy  $\sqrt{k_s}$  ( $k_s = 0.5(u_{HT}^2 + u_{HT}^2)$ ) can be used instead of  $Re_T$  as shown in Figure 5.14. Also shown in this figure are the data from Atmane & George (2002), who used up-flowing micro jets to generate the turbulence. The data from Chu (1990) are still lower perhaps due to the invasive oxygen probes. On the other hand, the data from Atmane & George (2002) are comparable to the present data although the turbulence generation are somewhat different. The square root of the interfacial kinetic energy  $\sqrt{k_s}$  seems to be a good alternative in order to characterize the different turbulence levels for the gas transfer process in a tank with far-field homogeneous turbulence.

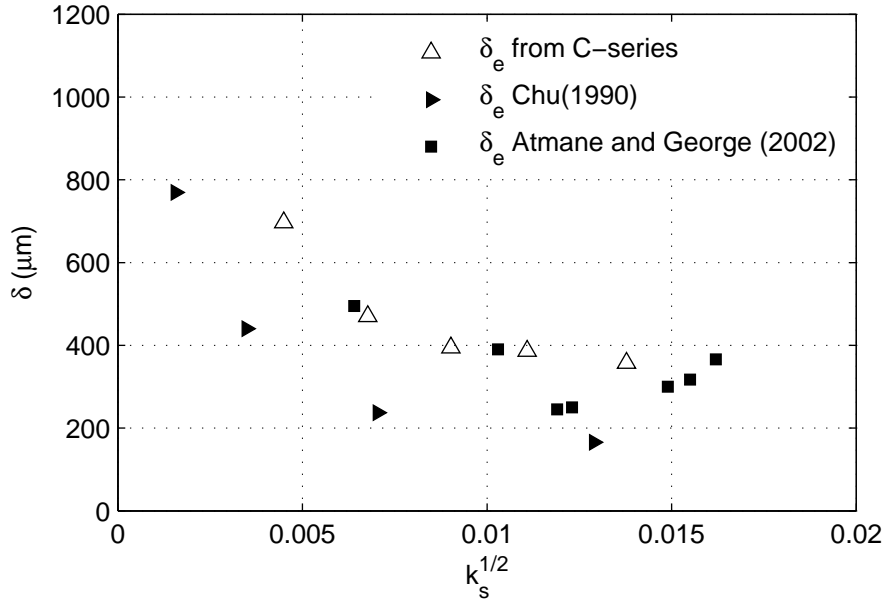


**Figure 5.14.** Measured boundary layer thickness  $\delta_e$  plotted against the square root of the interfacial turbulent kinetic energy  $\sqrt{k_s}$

In addition, the deviations of the measured  $\delta_g$  and  $\delta_e$  obtained from the simultaneous PIV-LIF measurements (CV-series) in comparison to the stand-alone LIF measurements (C-series) are included in Table 5.1 and are less than 5%. This further confirms that the effect due to the presence of the PIV seeding particles in the LIF images is negligible.

**Boundary layer thickness and outer diffusive sublayer.** Brumley & Jirka (1988) proposed the estimation of the thickness of an outer diffusive layer based on hydrodynamic arguments  $L_D = 2L_\infty Sc^{-1/2} Re_T^{-1/2}$  (see Figure 2.1). Chu & Jirka (1992) found that the outer diffusive sublayer ( $L_D$ ) have a quantitative relationship to the boundary layer thickness  $\delta_e$  as follows

$$\delta = cL_\infty Sc^{-1/2} Re_T^{-1/2} \quad (5.7)$$

where  $c$  lies in the range of 2 and 3. Since the outer diffusive layer is controlled by the large eddies (Brumley & Jirka 1988), Chu & Jirka (1992) conclude that the gas transfer process should be dominated by the large eddies at least in their measured range of turbulent Reynolds number (80 to 660).

Figure 5.15 shows the estimated outer diffusive sublayer for the present grid conditions plotted against the measured boundary layer  $\delta_e$ . In the figure, the value of  $\delta_e$  is taken as the mean value from the  $\delta_e$  obtained from the stand-alone LIF measurements (C-series) and the simultaneous PIV-LIF measurements (CV-serie). Also plotted in the graph is the quantitative relationship given in Eq. 5.7 indicated by the solid line. Excluding the data

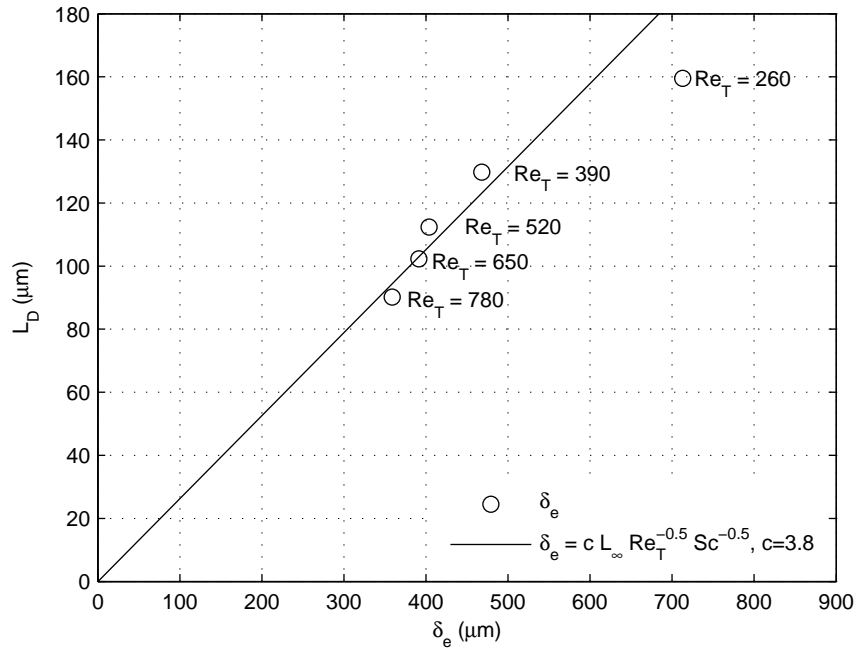


**Figure 5.15.** Outer diffusive sublayer vs boundary layer thickness

point  $Re_T = 260$ , a  $c$  value of 3.8 gives the best fit for Eq. 5.7. The figure shows that Eq. 5.7 agrees well for  $Re_T$  ranging from 390 to 780.

### 5.2.3 Normalized mean profiles

Assuming horizontal homogeneity, Jähne & Haussecker (1998) have shown that the mass flux equation can be solved in order to describe the concentration distribution as a function of depth. They solved the mass flux equation by incorporating the surface renewal assumption and small eddy assumption with two different boundary conditions, namely a mobile interface and a rigid wall interface. A mobile boundary represents a clean interface, whereas a rigid-wall boundary maybe associated to very high contaminated interface. The detailed solving steps to the solution are omitted but the resulting equations are given.

Incorporating the surface renewal assumption when solving the mass flux equation with a mobile interface boundary condition, one ends up with an exponential function.

$$\bar{c}_+(z_+) = \exp(-z_+) \quad (5.8)$$

Note that the solution is the same as the exponential function proposed empirically by Chu & Jirka (1992). The normalized concentration  $c_+$  and depth  $z_+$  in Eq. 5.8 is presented as  $(C - C_b)/(C_s - C_b)$  and  $z/\delta_e$ , respectively in Eq. 5.4. Eq. 5.9 is the solution assuming a surface renewal scheme for the case of a rigid-wall boundary.

$$\bar{c}_+(z_+) = \frac{1}{\text{Ai}(0)} \text{Ai} \left[ \frac{\text{Ai}(0)}{\text{Ai}'(0)z_+} \right] \quad (5.9)$$

with Ai is the Airy function and Ai' the derivative of the Airy function with respect to  $z_+$ . Ai (0) and Ai(0) / Ai'(0) have the approximate values of 0.3550 and 1.372, respectively. The solutions when incorporating the small eddy assumption are given in Eqs. 5.10 and 5.11 for the case of a mobile and rigid-wall boundary, respectively.

$$\bar{c}_+(z_+) = \frac{2}{\pi} \text{arccot} \left[ \frac{\pi}{2z_+} \right] \quad (5.10)$$

$$\bar{c}_+(z_+) = \left[ 1 + \frac{-6\text{arctan}(1/\sqrt{3} + 2\sqrt{3}\log(9) - \sqrt{3}\log(81))}{4\pi} \right] \left[ \frac{-6\text{arctan}\left(\frac{-3^{3/2}+4\pi z_+}{9}\right) + 2\sqrt{3}\log(9 + 2\sqrt{3}\pi z_+)}{4\pi} \right] \left[ \frac{-\sqrt{3}\log(81 - 23^{5/2}\pi z_+ + 12\pi^2 z_+^2)}{4\pi} \right] \quad (5.11)$$

Figure 5.16 shows the normalized mean concentration profiles from CV1 to CV5. In this figure, the measured boundary layer thickness defined based on the steepest gradient at the surface  $\delta_g$  is used to scale the depth and the normalized concentration is presented in the form of  $(C - C_b)/(C_s - C_b)$ . Also plotted in the figure are the theoretical profiles given in Eqs. 5.8 to 5.11. It should be noted that the major difference between the predictions given by the surface renewal model and the small eddy model is that the profile predicted by the surface renewal model decreases much faster towards the concentration in the bulk region. In this figure, no clear match can be found between the measured profiles and the different theoretical predictions. However, the profiles show a tendency that the profiles with lower  $Re_T$  experience a faster decrease towards the concentration in the bulk. When  $\delta_e$  instead of  $\delta_g$  is used to scale the depth a better interpretation associated with the theoretical profiles can be obtained as discussed in the following paragraph.

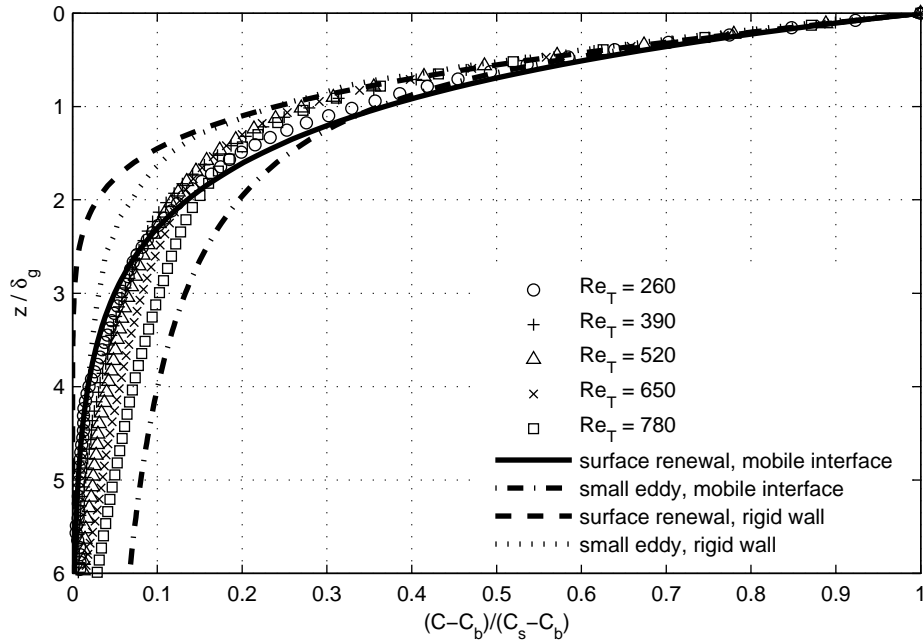


**Figure 5.16.** Normalized mean concentration profiles plotted against the depth normalized with  $\delta_e$ . Only every seventh data point is shown in the graph to avoid congestion.

The normalized mean concentration profiles that are plotted against  $z/\delta_e$  instead of  $z/\delta_g$  are shown in Figure 5.17. Indeed, the use of  $\delta_e$  as a scaling factor will bias the shape of the profile towards an exponential distribution. However, the bias will not cause complete distortion of the actual profile shape. By using  $\delta_e$  to scale the depth, the normalized profiles fall between the surface renewal model and the small eddy model with mobile interface as shown in Figure 5.17. One may think that a distinction between this two models is vulnerable. However, for the case of mobile interface, the faster decrease towards

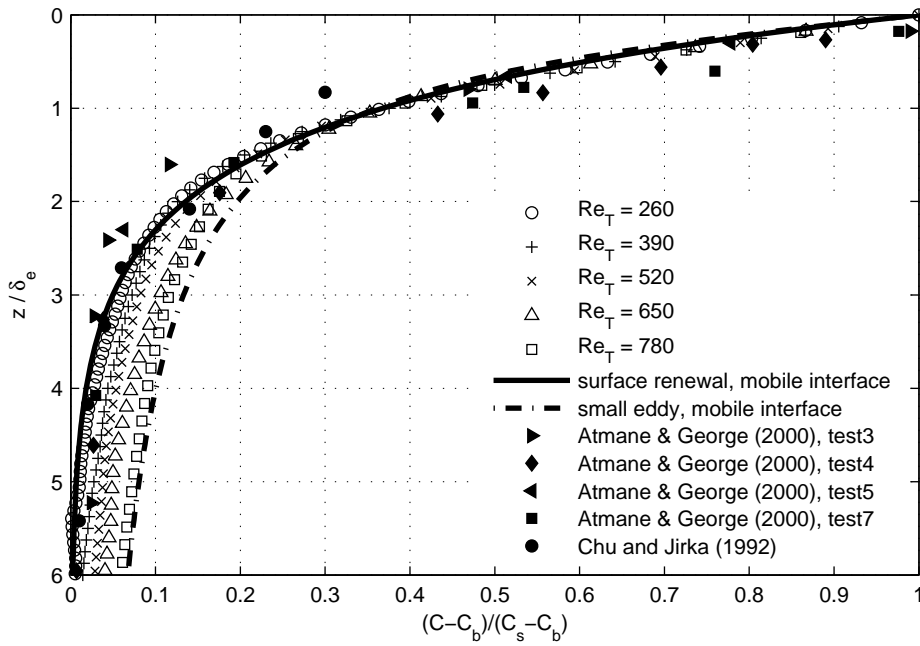
the concentration in the bulk region predicted by the surface renewal model compared to the small eddy model is an effect of the order of 10% that should not change due to simple scaling effects. With the profiles in Figure 5.17 clearly show the following tendency, as the turbulent Reynolds number increases, the decay of the concentration into the bulk is slower. The results indicate that the gas transfer is controlled by a spectrum of different eddy sizes. It seems that the gas transfer at different turbulence levels can be associated with a certain eddy size. At very high turbulence levels, the eddy sizes should be asymptotic to the Kolmogorov scales. From a practical point of view, the results can be interpreted that the surface renewal model holds better for low  $Re_T$  whereas the small eddy model appears preferable for high  $Re_T$ . This supports the idea of the two-flow regime model suggested by Theofanus (1984).

The data points from Chu & Jirka (1992) with  $Re_T = 360$  and Atmane & George (2002), who performed gas transfer measurements in similar experimental facilities as the present study, are incorporated in the figure for comparison which obviously highlights the advantage of the non-intrusive LIF quenching method over their point-based measurement technique. The spatial resolution is much higher thus the vertical concentration profile could be elucidated in more detail. The mean distribution obtained by Chu & Jirka (1992) and Atmane & George (2002) showed relatively good agreement with the surface renewal model. It should be noted that their  $Re_T$  measurement range was mostly below 500 which was classified as low turbulent intensity by Theofanus (1984).

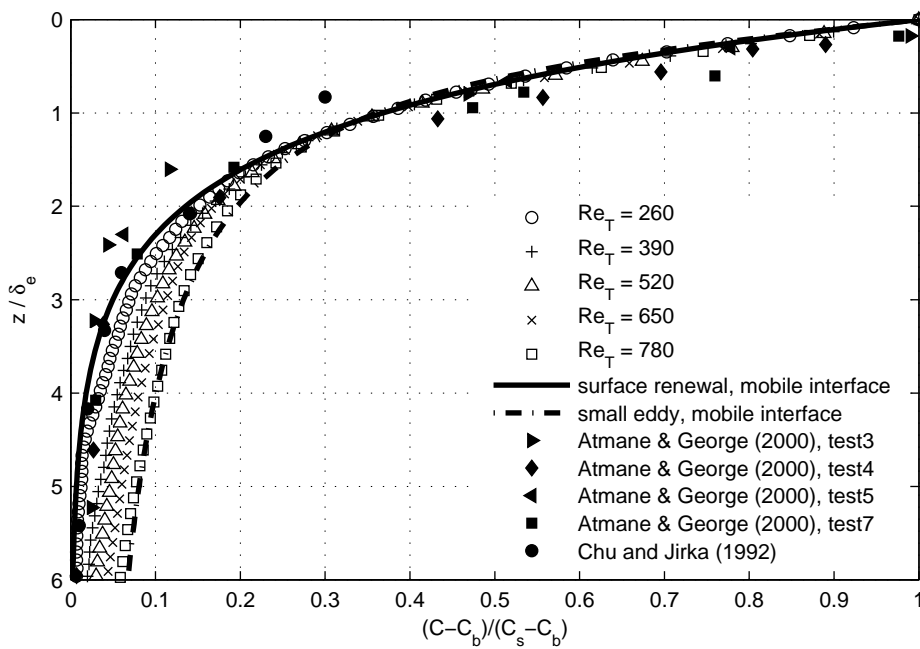
#### 5.2.4 Normalized fluctuation profiles

The variation of  $c'$  with the depth measured in this study is shown in Figure 5.18. The  $c'$  values are normalized with  $C_s - C_b$  and the depth with  $\delta_e$ . Figure 5.18 shows that the fluctuations increase from smaller values near the interface to a maximum around the boundary layer thickness ( $z/\delta_e = 1$ ). The maximum peaks range between 0.15 to 0.2. After reaching a maximum, the  $c'$  values decrease with further submergence. Theoretically, the  $c'$  values in the bulk region should be equal to zero. The margins of error for an instantaneous profile was estimated to be  $\pm 5\%$  (see Section 3.4). For the mean concentration profiles, it is expected that the noise levels contained in the instantaneous profiles would cancel out each other. In contrast, the noise level in the  $c'$  is maintained. Therefore, the non-zero value (2-5%) in the bulk region is due to the noise level present in the instantaneous concentration profiles.

The concentration fluctuations below the interface in a tank with far-field homogeneous turbulence have been measured among others by Chu & Jirka (1992) and Atmane & George (2002). The data points from previous work are incorporated in the figure for comparison. The fluctuation values of the present data show some discrepancies with

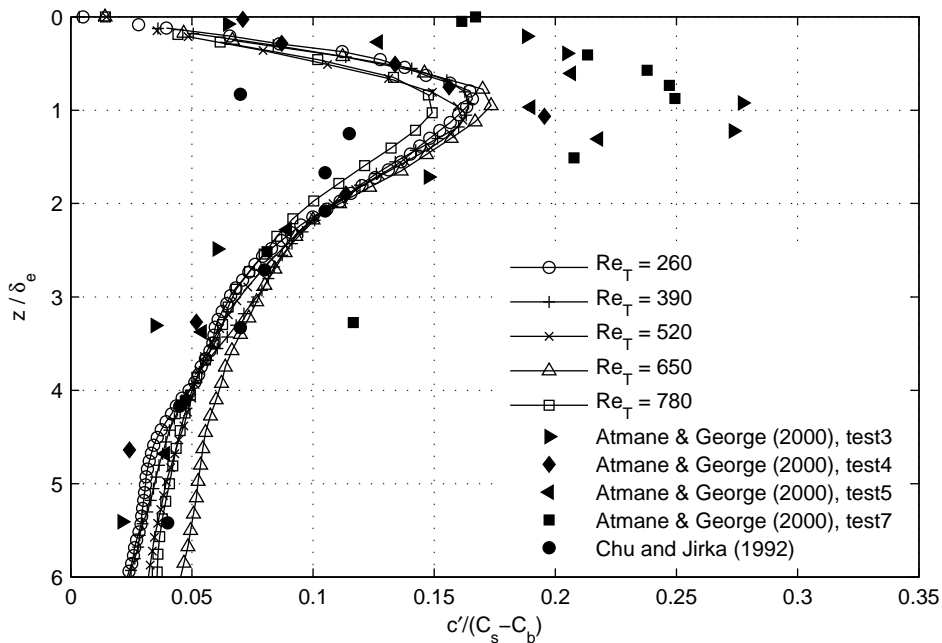


(a) stand-alone LIF

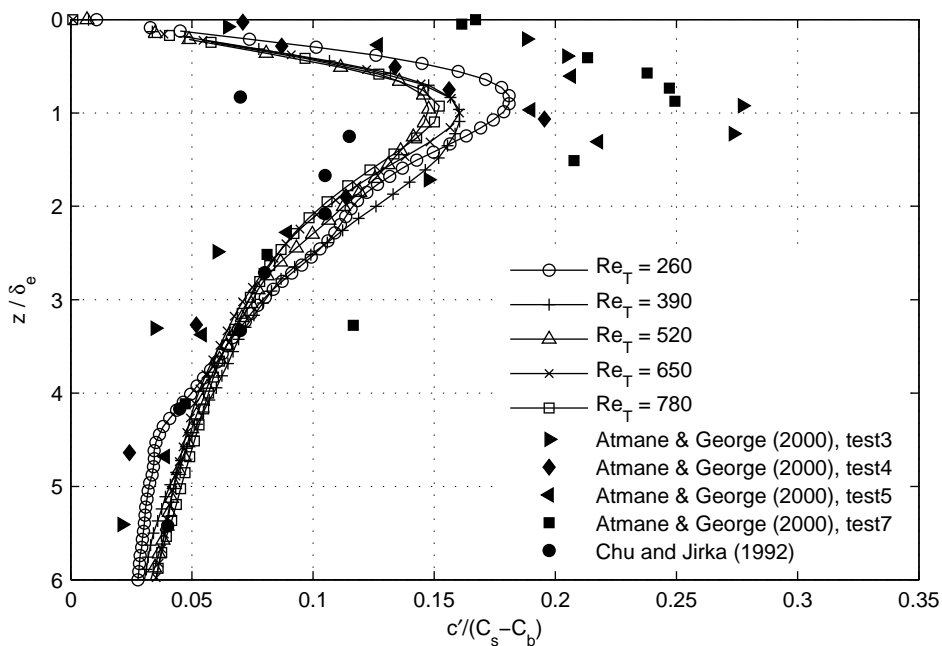


(b) simultaneous PIV-LIF

**Figure 5.17.** Normalized mean concentration profiles with stand-alone LIF and with simultaneous PIV-LIF. Only every seventh data point is shown in the graph to avoid congestion.



(a) stand-alone LIF



(b) simultaneous PIV-LIF

**Figure 5.18.** Normalized fluctuation concentration profiles. Only every seventh data point is shown in the graph to avoid congestion. The unconnected data points extremely close to the surface are data points that are probably biased due to the optical blurring correction procedure in the image processing.



the previous data. It should be noted that both Atmane & George (2002) and Chu & Jirka (1992) used an invasive polarographic oxygen microprobe to measure the oxygen concentration level. The probe was rotated on a horizontal level to obtain the statistics of the vertical concentration distributions. This means that the data points obtained by them were discrete and not simultaneous. Moreover, it was difficult to assure a constant distance from the surface through the whole experiments. This might have caused an unpredictable bias in the  $c'$  values. The advantages of the present measurements over Chu & Jirka (1992) and Atmane & George (2002) is the non-invasive technique and the capability of providing instantaneous planar concentration information with a good temporal resolution.

Regarding the concentration fluctuations extremely near the interface, previous experiments by Chu & Jirka (1992), Atmane & George (2002) and Prinos et al. (1995) yielded different results. Chu & Jirka (1992) interpreted from their result that the concentration fluctuations very near the interface decreases to zero towards the interface. Atmane & George (2002) also observed a decrease of the fluctuations near the interface. In contrast, the results from Prinos et al. (1995) showed an increase towards the surface. It is difficult to find a reason for the discrepancy. It should be noted that this interface region is infinitely thin. Thus, it is expected that this region is a singular region, especially when using invasive measurement techniques.

The physical explanation for the zero and non zero value of  $c'$  at the interface is as follows. When a surface renewal effect reaches the surface and sweeps part of the boundary layer (i.e. up to the interface) into the bulk, the surface concentration may drop significantly from its saturation value. This effect causes the non-zero value  $c'$  at the interface. On the other hand, the surface concentration remains saturated when the surface renewal effect does not reach the boundary and so the  $c'$  value is zero.

In the present study, the fluctuation in the vicinity of the interface show a tendency to decrease to zero towards the interface as shown in Figure 5.18. The level of certainty of the  $c'$  data extremely close to the water surface is unpredictable due to the optical blurring correction procedure performed in the image processing as has been mentioned in Section 5.2.1. Same as in Figure 5.8, the probably biased data points are purposely left unconnected by the solid lines in order to distinguish them from the unbiased data points. From visual observations, a distinct boundary layer could always be detected in all the raw LIF images recorded in the present study. In other words, the surface renewal effect was never found penetrating up to the air-water boundary. This means that the surface concentration is expected to be always at saturation. Therefore, the tendency towards zero for the concentration fluctuations near the surface shown in Figure 5.18 is most probably

a real physical effect at least for the present range of turbulent Reynolds number ( $Re_T = 260$  to  $780$ ).

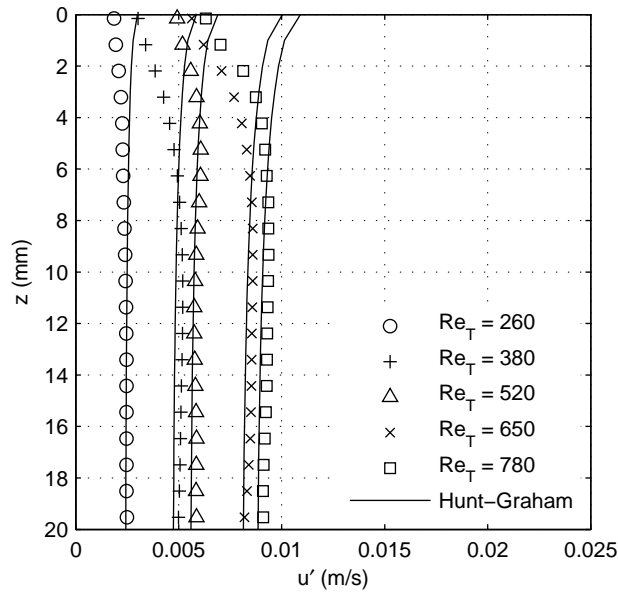
### 5.3 Velocity fluctuations near the interface

The profiles of the horizontal and vertical velocity fluctuations in the vicinity of the water surface, which are obtained from the simultaneous PIV-LIF measurements (CV-series), are presented in Figure 5.19.

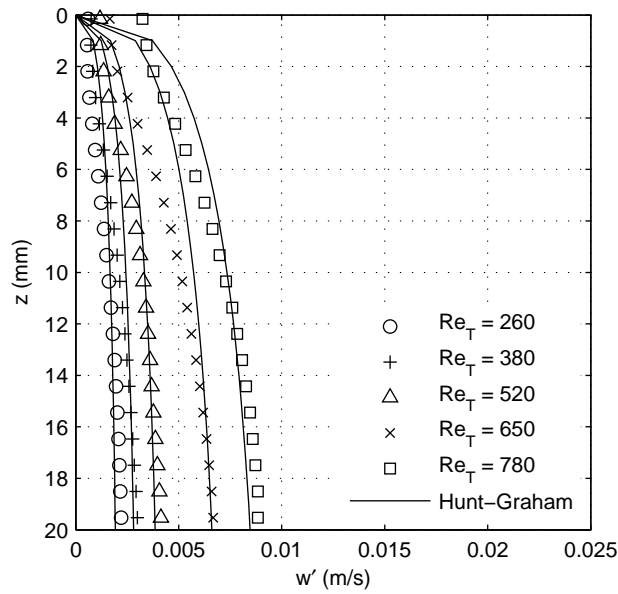
The solid lines shown in Figure 5.19 are the fitted relations proposed by Brumley & Jirka (1987) that are based on the Hunt & Graham (1978) theoretical predictions. The relations have been given in Eqs. 2.24 and 2.25. Brumley & Jirka (1987) found that within a distance of approximately 10% of  $z_s$  from the surface, the velocity fluctuations are influenced by the surface and deviated from the Hopfinger & Toly predictions, with  $z_s$  is the distance between the water surface and the centre of the grid. For this reason, Brumley & Jirka (1988) suggested that the far-field fluctuations values  $u'_\infty$  and  $w'_\infty$  in Eqs. 2.24 and 2.25 can be estimated with the  $u'$  value at 10% of  $z_s$  below the water surface calculated using the Hopfinger & Toly relation Eq. 2.22. The  $c$  values from Eq. 2.22 for the grid conditions in the CV-series ranged between 0.18 to 0.25.

The same profiles from Figure 5.19 are plotted again in a normalized form in Figure 5.20 to show the similar behavior of the profiles despite the varying experimental conditions. The velocity fluctuations  $u'$  and  $w'$  are scaled with their values at  $z = 20$  mm  $u'_{z=20}$  and  $w'_{z=20}$ . The depth  $z$  is normalized with the distance between the water surface and the centre of the grid  $z_s$  and presented as percentage. Figure 5.20a and b indicate that the profile shapes in most of the surface-influenced layer agree well with the theoretical profile from Hunt & Graham. Extremely near the water surface, however, the measured profiles starts to deviate from the Hunt & Graham profile. Here, the velocities are lower than the Hunt & Graham profile. This shows the existence of a viscous boundary layer, which following the estimation from Brumley & Jirka (1987) should range between  $z/z_s = 0.4\%$  to  $0.6\%$  (see Table 3.4). The vertical fluctuations are better predicted by the Hunt & Graham theory as compared to the horizontal fluctuations. The Hunt & Graham theory predicts an increase of horizontal fluctuations very near the interface. Contrary, the present data for all series show that the horizontal fluctuations constantly decrease when approaching the surface. The data from Brumley & Jirka (1987) showed the same behavior.

The deviation from the theory is due to the fact that the Hunt & Graham irrotational source theory does not take into account several second order effects. The purely kinematic Hunt & Graham theory assumes a uniform (i.e. constant with depth) dissipation rate even in the theoretical source layer. It also assumes that the smallest eddies near a surface are

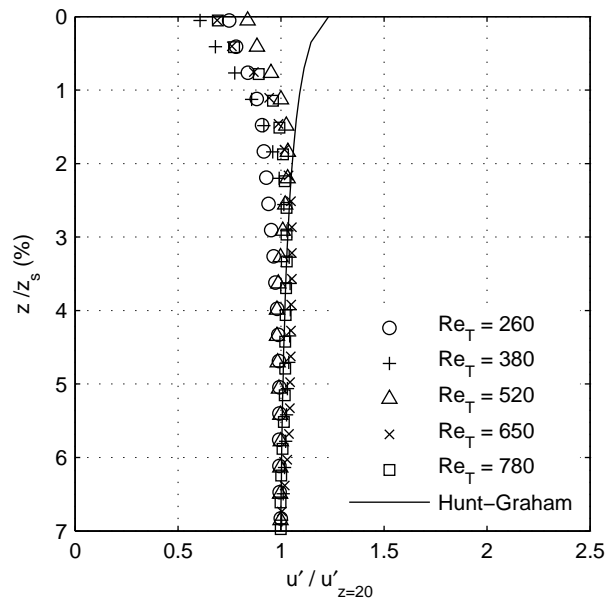


(a) horizontal fluctuation

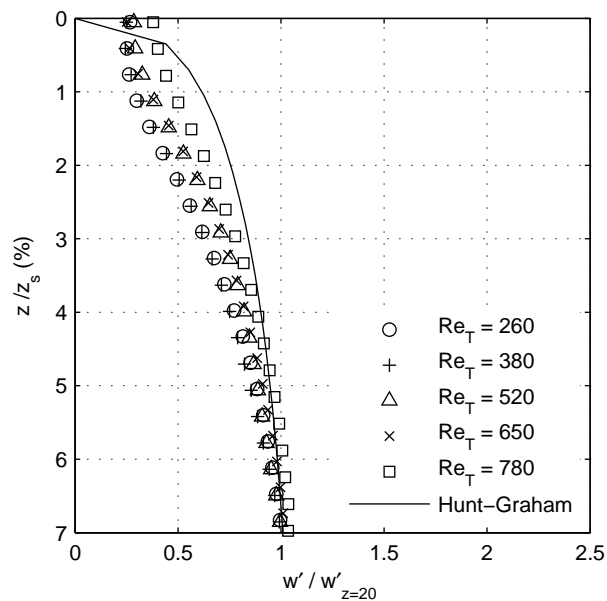


(b) vertical fluctuation

**Figure 5.19.** Turbulence fluctuations near the interface (from CV-series) (a) horizontal fluctuation (b) vertical fluctuation



(a) horizontal fluctuation



(b) vertical fluctuation

**Figure 5.20.** Normalized turbulence fluctuations near the interface (from CV-series) (a) horizontal fluctuation (b) vertical fluctuation

of the same size as the smallest eddies in isotropic turbulence. These assumptions are not exactly true. With their assumptions, the surface effect modifies the velocity spectra at low wavenumbers, but the inertial subrange of wavenumbers associated to length scales smaller than the depth and larger than the Kolmogorov scale is supposed to be unaffected. However, this may not be the case as indicated by the dissipation rates profiles measured by Brumley (1984). Anisotropic straining may transfer energy from the vertical to the horizontal component even in the inertial subrange. All these dynamics are not considered by the Hunt & Graham theory.

Besides the above dynamics, the Hunt & Graham theory also does not consider the existence of a viscous boundary layer, which obviously exist in the present experiments. The two extreme boundary conditions at the interface are specified by either zero shear-stress (clean surface) or zero velocity fluctuations (dirty surface). At a perfectly clean interface, the viscous boundary layer mostly affects the horizontal velocity, whereas the effect on the vertical velocity is negligible. The non-zero horizontal velocity fluctuations at the interface (Figure 5.20b) indicate that the surface in the present experiments is far from dirty. With the careful precaution taken during the experiments, the water surface can be categorized as a clean surface. Thus, it is expected that the Hunt & Graham theory predicts the vertical velocity fluctuation better than the horizontal one.

## 5.4 Oxygen transfer velocity ( $K_L$ )

The time histories of the oxygen concentration and temperature increase during the approximately three hours Cb-series measurements for all five grid conditions are shown in Figure 5.21.

The oxygen velocity transfer  $K_L$  defined in Eq. 2.6 is related to the reaeration coefficient  $K_2$  through the following equation

$$K_L = K_2 \cdot H \quad (5.12)$$

with  $H$  is the water depth. The reaeration coefficient  $K_2$  can be determined using the conservation of mass equation

$$\frac{dC_b}{dt} = K_2(C_s - C_b) \quad (5.13)$$

Integrating Eq. 5.13 with an initial condition  $(C_s - C_b)_o$  at time  $t = t_o$  yields

$$\ln(C_s - C_b)_o - \ln(C_s - C_b) = K_2(t - t_o) \quad (5.14)$$

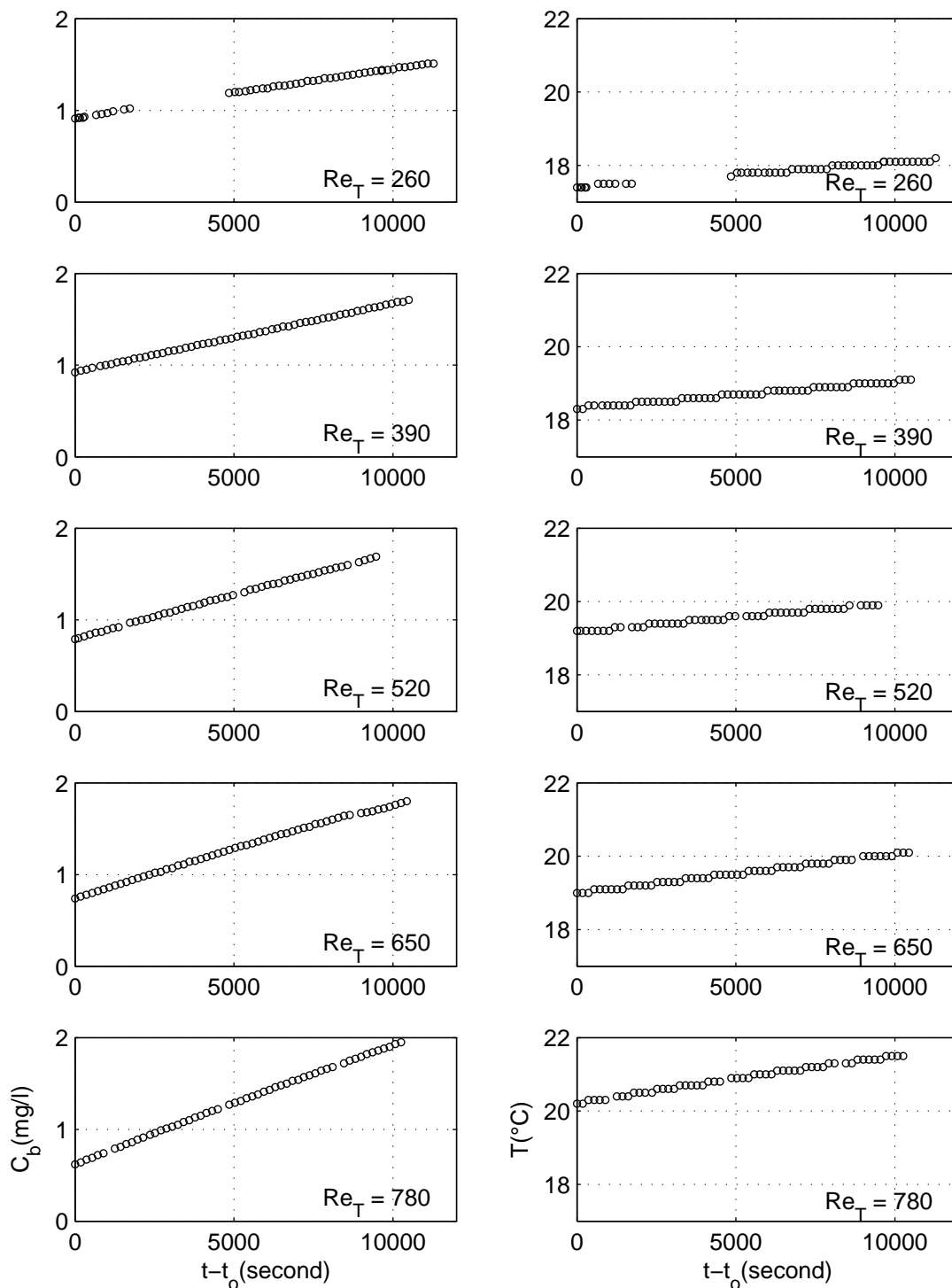


**Figure 5.21.** Bulk concentration measurements ( $C_b$ -series) : Time histories of oxygen concentration as well as temperature in the bulk region for all five grid conditions

In the literature,  $K_2$  and  $K_L$  values are normally reported at a reference temperature of 20°C. A correction factor of 1.0241 proposed by Churchill (1961) can be used for the temperature  $T$  differences

$$K_2(T) = K_{2,20} \cdot 1.0241^{(T-20)} \quad (5.15)$$

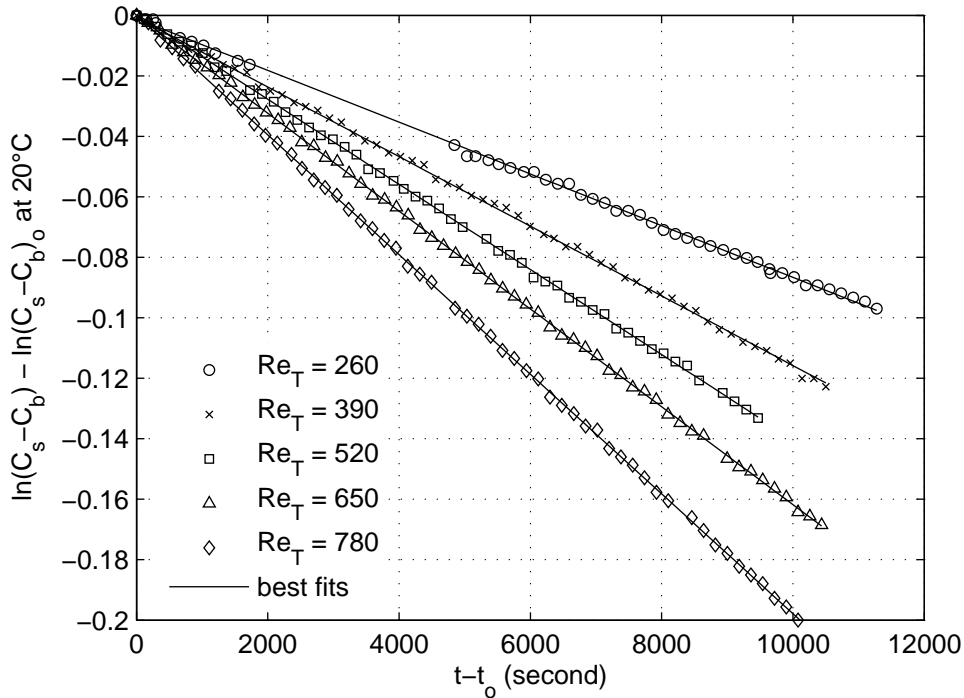


**Figure 5.22.** Bulk measurement in the form of Eq. 5.14 to determine the re-aeration coefficient,  $K_2$

Based on the above equations, the  $K_2$  values are determined as the gradients obtained from the graph in Figure 5.22. As expected, the oxygen transfer rate increases with increasing turbulence as can be clearly observed in Figure 5.22.

Finally, the transfer velocity  $K_{L,t}$  values at 20°C can be obtained by multiplying  $K_2$  with the water depth in the tank. The  $K_{L,t}$  values obtained for all grid conditions are shown in Table 5.2.

Based on the simplest film model by Lewis & Whitman (1924), the gas boundary layer thickness is related to the transfer velocity using Eq. 2.9. For comparison, the transfer velocities  $K_{L,\delta_e}$  estimated based on Eq. 2.9 using the measured  $\delta_e$  are included in Table 5.2. When turbulence is present, the transfer velocity calculated using the film model ( $K_{L,ze}$ ) is usually underestimated compared to the actually measured ( $K_{L,t}$ ) one. This is expected as the film model oversimplifies the actual mechanism. The presence of turbulence causes

Exp. Serie	$Re_T$	$K_2$ (1/s)	$H$ (cm)	$K_{L,t}$ (cm/s)	$K_{L,\delta e}$ (cm/s)
Cb1	260	$8.55 \cdot 10^{-6}$	28.6	$4.16 \cdot 10^{-4}$	$2.80 \cdot 10^{-4}$
Cb2	390	$11.51 \cdot 10^{-6}$	28.5	$5.58 \cdot 10^{-4}$	$4.27 \cdot 10^{-4}$
Cb3	520	$14.07 \cdot 10^{-6}$	28.5	$6.82 \cdot 10^{-4}$	$4.95 \cdot 10^{-4}$
Cb4	650	$16.18 \cdot 10^{-6}$	29.0	$7.93 \cdot 10^{-4}$	$5.11 \cdot 10^{-4}$
Cb5	780	$19.79 \cdot 10^{-6}$	28.0	$9.50 \cdot 10^{-4}$	$5.57 \cdot 10^{-4}$

**Table 5.2.**  $K_L$  values with varying turbulence intensities.  $K_{L,t}$  is the absolute transfer velocity coefficient determined from the bulk measurement.  $K_{L,\delta e} = D/\delta_e$  is the estimated transfer velocity using the film model

constant changes of the boundary layer thickness and also may transport portions of rich oxygen layers into the bulk. This, of course, would affect the gas transfer process.

The prediction of  $K_L$  using the large eddy model Eq. 2.14 can be written in the form

$$\frac{K_L \cdot Sc^{0.5}}{u} = aRe_T^{-0.5} \tag{5.16}$$

whereas using the small eddy model in the form

$$\frac{K_L \cdot Sc^{0.5}}{u} = bRe_T^{-0.25} \tag{5.17}$$

with  $u$  is the turbulent velocity scale,  $a$  and  $b$  are coefficients of proportionality.

The normalized  $K_L$  values obtained in this study are plotted in Figure 5.23 against the turbulent Reynolds number using a log-log scale. For the present case, the Hopfinger & Toly velocity predicted at the interface  $u_{HT}$  is taken as the turbulent velocity scale.

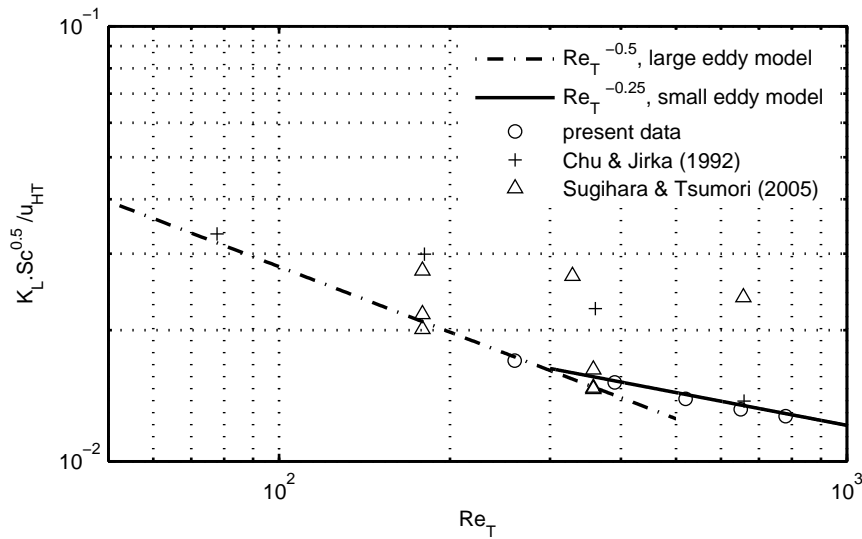


**Figure 5.23.** Variation of the normalized transfer velocity  $K_L$  with the turbulent Reynolds number  $Re_T$



The data obtained by Chu & Jirka (1992) and Sugihara & Tsumori (2005) are included in the graph. The dashed lines shown in the figure are Eqs. 5.16 and 5.17 with  $a = 0.28$  and  $b = 0.07$ . Fortescue & Pearson (1967) suggested a value of  $a = 1.46$  and Lamont & Scott (1970)  $b = 0.4$ , whereas Theofanus (1984) proposed  $a = 0.73$  and  $b = 0.25$ . Chu & Jirka (1992), whose turbulence generation was similar to the present study, obtained a lower value of  $a = 0.25$  that is comparable to the present value. The large discrepancy of the coefficients  $a$  and  $b$ , could be due to the differences in the turbulent scales definitions between grid-stirred tank and open channel flow as already pointed out by Chu & Jirka (1992).

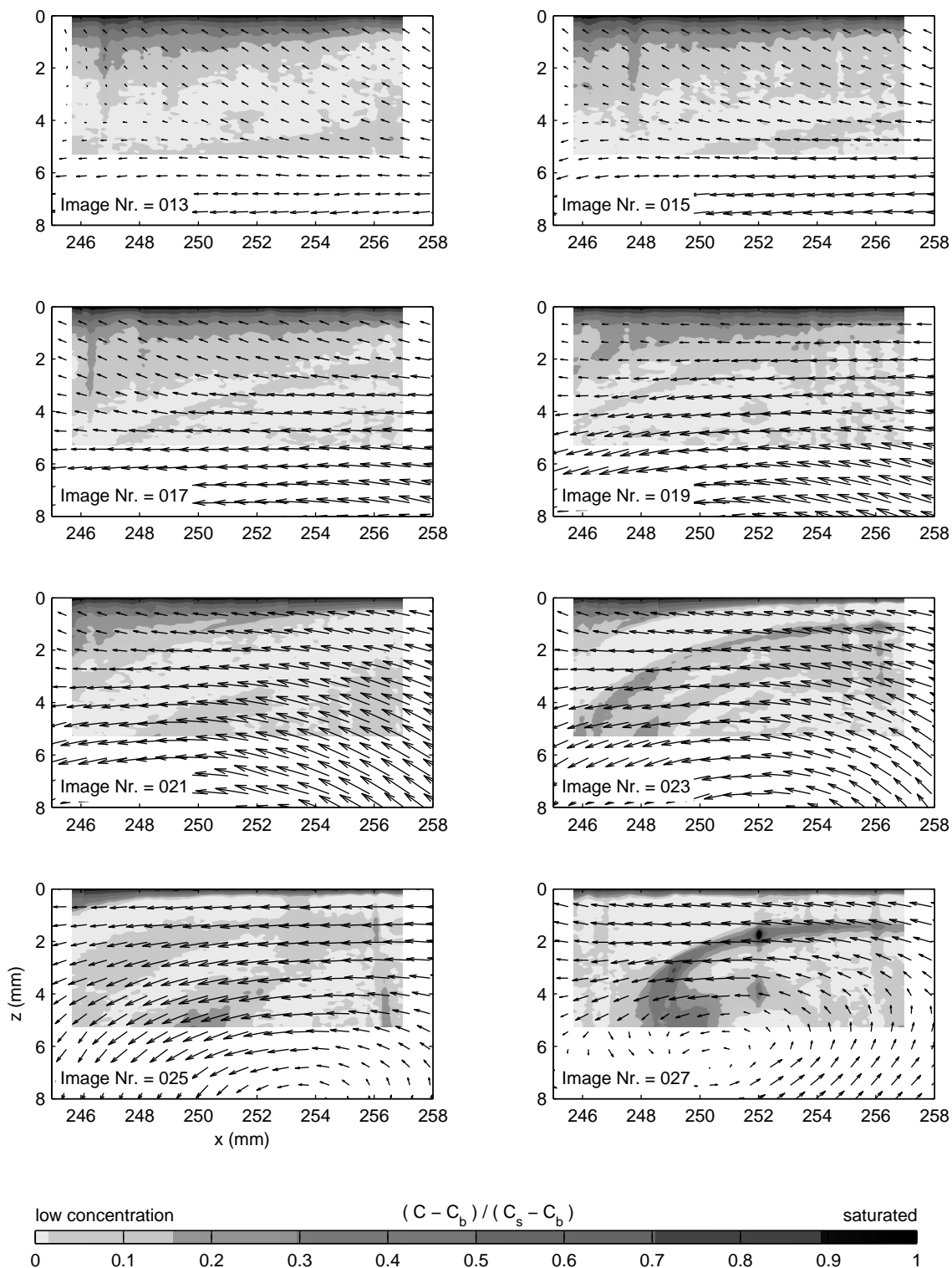
## 5.5 Turbulent mass flux

The turbulent mass flux quantities, the second term of Eq. 2.5, could be measured directly in the present study using the eddy-correlation method owing to the combined PIV and LIF technique. The simultaneous and spatially synoptic measurements of the velocity and concentration field directly below the water surface allowed direct quantification of the instantaneous turbulent mass flux  $cw$  as well as its time-averaged value  $\overline{cw}$ . The results are presented in the following sections.

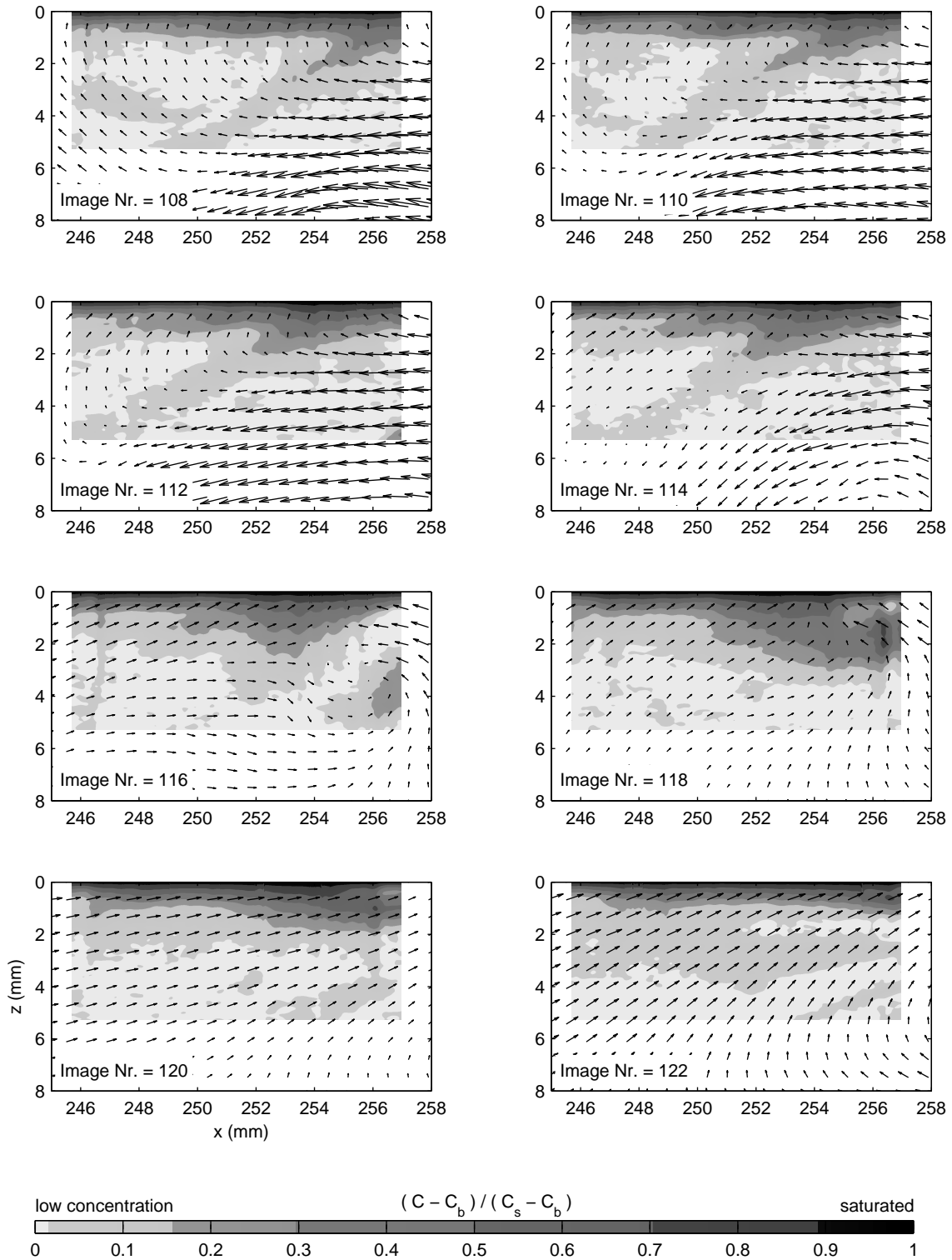
### 5.5.1 Instantaneous turbulent mass flux

Figure 5.24 and 5.25 show examples of 8 successive images of the simultaneous concentration and velocity maps taken from CV2 and CV3, respectively. The superimposition of the concentration map on to the velocity maps in one graph gives a better insight of the interaction between the turbulent flow-field and gas transfer process. For example, the velocity maps in Image Nr. 21 to 27 in Figure 5.24 indicate that an eddy is approaching the interface. The transport of water portions with high oxygen concentration from near the interface into the bulk is obviously associated to that eddy. One would expect that the actions of the eddies enhance the gas transfer rate. A similar process can be observed in Figure 5.25. It can also be seen that the eddies approaching the interface suppresses the boundary layer thickness. Observing Figure 5.24, the boundary layer thickness in Image Nr.17 is thicker compared to Image Nr. 25 where an eddy is approaching the interface. In Image Nr. 21, an eddy is approaching from the right hand side. It can be seen that the boundary layer on the right is being suppressed by that eddy.

It should be noted that the sequences shown above clearly demonstrate the logical correlations of the flow-field with the concentration distribution. Thus, it visually convinces and proves that the data acquisitions of the velocity and concentration fields were indeed simultaneous both in time and space.



**Figure 5.24.** Sequence of oxygen contour map and vector map from the simultaneous PIV-LIF measurements, taken from CV2. The shown sequence was taken within 3.5 seconds and the time interval between the shown is 0.5 s.



**Figure 5.25.** Sequence of oxygen contour map and vector map from the simultaneous PIV-LIF measurements, taken from CV3. The shown sequence was taken within 3.5 seconds and the time interval between the shown is 0.5 s.

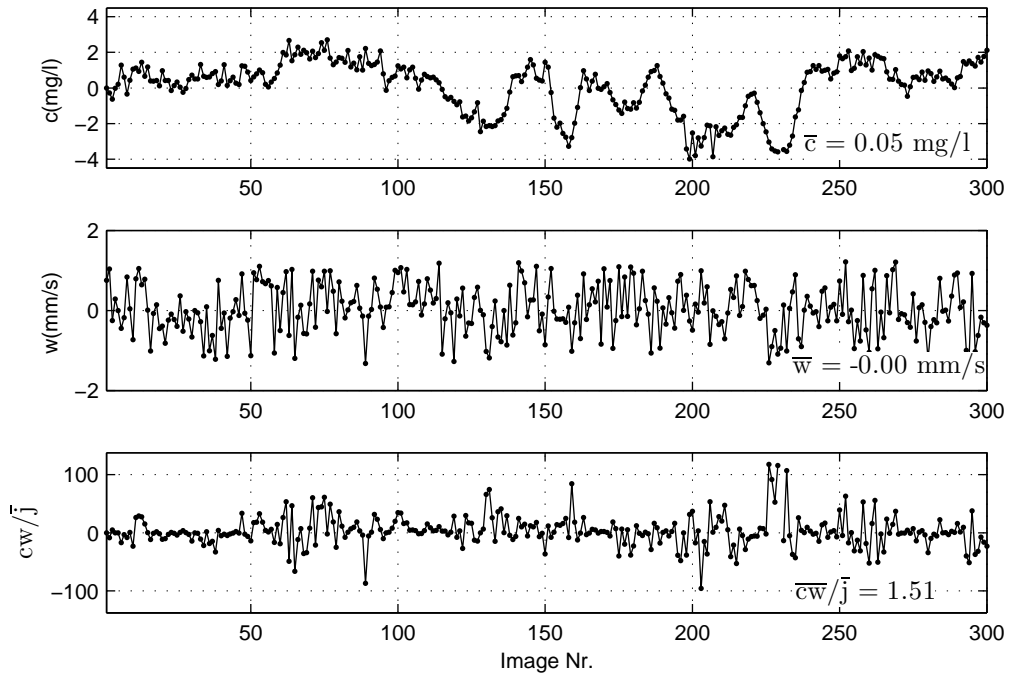
The cross product of the velocity fluctuations with its coinciding concentration fluctuations gives the turbulent mass flux quantities. It is interesting to look at the instantaneous fluctuation data in order to understand the interaction between the eddy motions and the gas transfer process. Representative time histories of the simultaneously measured concentration fluctuation and velocity fluctuation as well as their normalized cross-product at selected points from CV1 with  $Re_T = 260$  and CV5 with  $Re_T = 780$  are shown in Figure 5.26 and 5.27, respectively. In the graph, the measured turbulent mass fluxes are normalized by the mean flux ( $\bar{j} = K_L(C_s - C_b)$ ) determined from the obtained  $K_L$  values measured in the bulk concentration measurements (Cb-series). The mean fluxes  $\bar{j}$  for all five turbulent Reynolds numbers are summarized in Table 5.3. It has been observed that the largest absolute instantaneous concentration fluctuation ( $|c|$ ) that occurred at a certain depth was typically three times its root mean squared value ( $c'$ ). The same was found for the maximum absolute velocity fluctuations. The coordinate system for the gas transfer measurements has been shown in Figure 5.1. The vertical axis  $z$  is positive in the submergence direction so that a velocity vector pointing towards the bulk region is positive.

Exp. Serie	$Re_T$	$T$ (°C)	$K_{L,t}$ at 20°C (cm/s)	$C_s$ (mg/l)	$C_b$ (mg/l)	$\bar{j}$ (mg/l · cm/s)
CV1	260	14.3	$4.16 \cdot 10^{-4}$	10.12	1.02	$33.8 \cdot 10^{-4}$
CV2	390	14.4	$5.58 \cdot 10^{-4}$	10.10	0.97	$45.9 \cdot 10^{-4}$
CV3	520	14.8	$6.82 \cdot 10^{-4}$	10.09	0.98	$54.2 \cdot 10^{-4}$
CV4	650	15.0	$7.93 \cdot 10^{-4}$	9.96	0.77	$64.7 \cdot 10^{-4}$
CV5	780	15.3	$9.50 \cdot 10^{-4}$	9.90	0.89	$75.7 \cdot 10^{-4}$

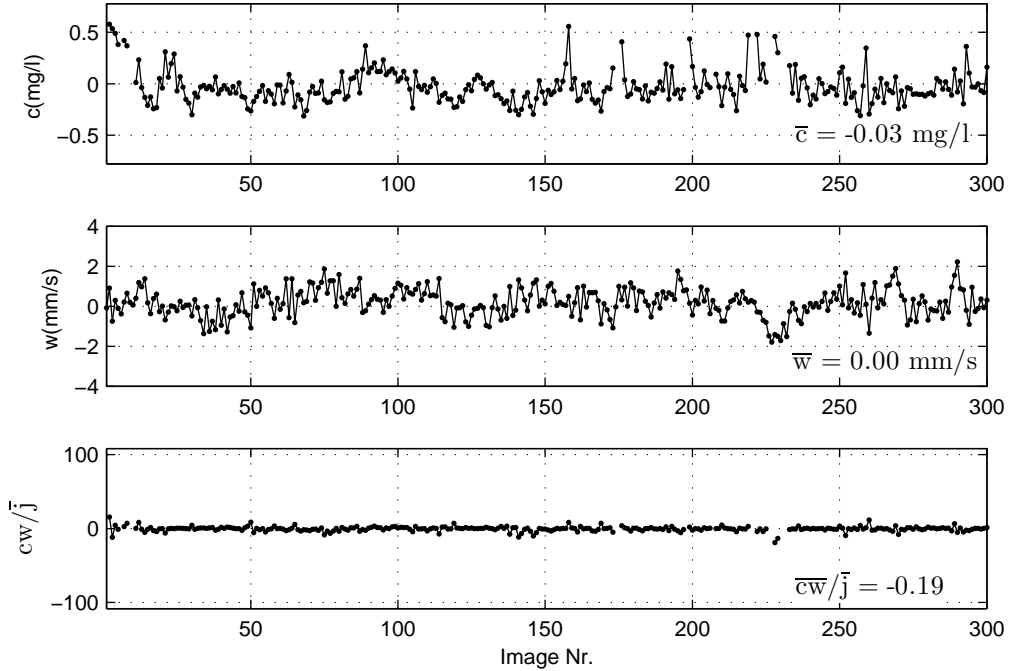
**Table 5.3.** Total mean flux values determined from the bulk measurements ( $\bar{j} = K_L(C_s - C_b)$ )

Part (a) of Figure 5.26 and 5.27 represents a measurement point near the interface ( $z = 0.5$  mm), whereas part (b) further away from the interface ( $z = 4.2$  mm). Comparing the actions that occur at these different depths, the concentration fluctuations are significantly higher near the interface. Here, the instantaneous cross-product  $cw$  fluctuates energetically and can reach a value up to two orders magnitude larger than the absolute mean flux  $\bar{j}$ . At deeper submergence, although the vertical velocity fluctuations increase with distance from the interface, the rapid decrease of the concentration fluctuations seems to suppress the turbulent mass flux. This is shown in Figures 5.26b and 5.27b, the  $cw$  fluctuates very weakly and becomes almost zero.

A downward flux that represents an oxygen transfer from the air into the water body occurs when both fluctuations are correlated (i.e. a positive turbulent mass flux). As depicted in Figure 5.26 and 5.27, the concentration fluctuations  $c$  are not always correlated

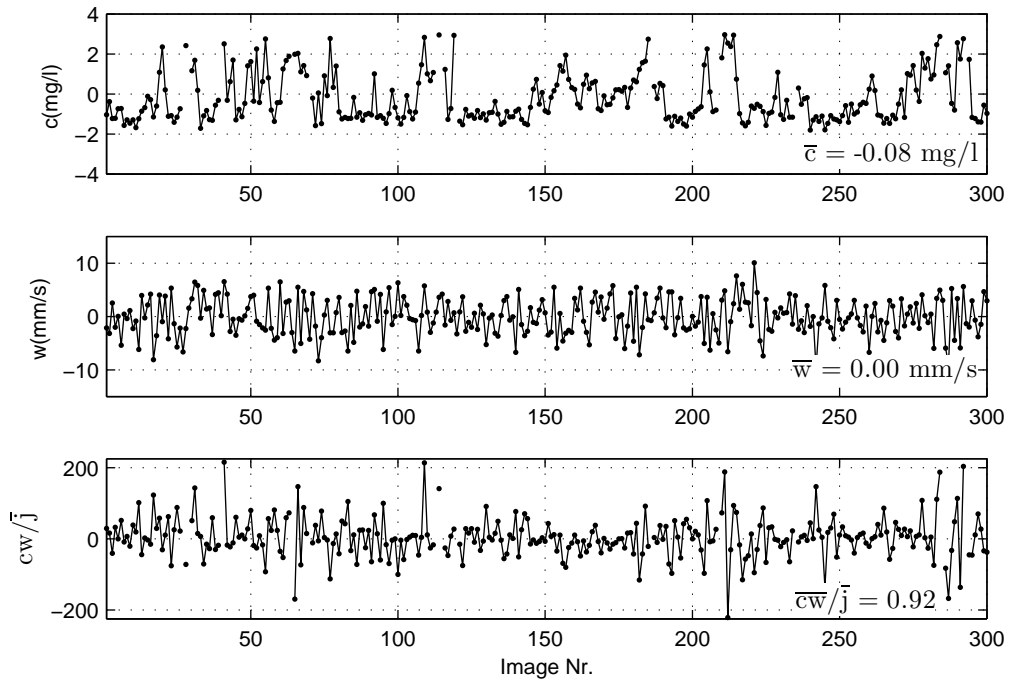


(a)  $z = 0.5$  mm

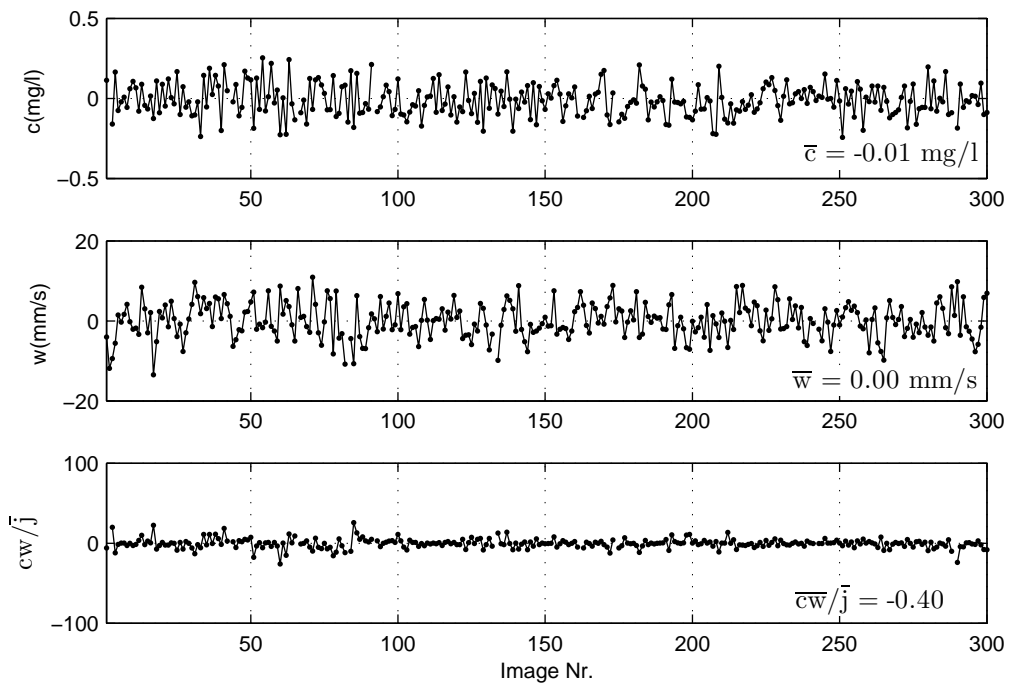


(b)  $z = 4.2$  mm

**Figure 5.26.** Time history of the simultaneously measured  $c$  and  $w$  and their normalized cross-correlation at selected points with  $Re_T = 260$  (CV1) (a)  $x = 253.7$  mm,  $z = 0.5$  mm (b)  $x = 253.7$  mm,  $z = 4.2$  mm



(a)  $z = 0.5$  mm



(b)  $z = 4.2$  mm

**Figure 5.27.** Time history of the simultaneously measured  $c$  and  $w$  and their normalized cross-correlation at selected points with  $Re_T = 780$  (CV5) (a)  $x = 253.7$  mm,  $z = 0.5$  mm (b)  $x = 253.7$  mm,  $z = 4.2$  mm

with the vertical velocity fluctuations  $w$ . From these instantaneous data, the fluxes can be classified into four quadrants :

1.  $w < 0, c < 0$  : Here, an upward (negative) fluctuation in  $w$  is associated with a negative concentration fluctuation resulting in a "downward flux caused by an upwelling eddy motion".
2.  $w > 0, c > 0$  : Here, a downward (positive) fluctuation in  $w$  is associated with a positive concentration fluctuation resulting in a "downward flux caused by a downwelling eddy motion".
3.  $w < 0, c > 0$  : Here, an upward (negative) fluctuation in  $w$  is associated with a positive concentration fluctuation resulting in a "upward flux caused by an upwelling eddy motion".
4.  $w > 0, c < 0$  : Here, a downward (positive) fluctuation in  $w$  is associated with a negative concentration fluctuation resulting in a "upward flux caused by a downwelling eddy motion".

Despite, the occurrence of upward fluxes, a downward (positive) net flux for the mean turbulent mass flux  $\overline{cw}$  that equals the mean flux  $\overline{j}$  across the interface should be expected.

A physical explanation of the positive fluxes (quadrant 1 and 2) and the negative fluxes (quadrant 3 and 4) has been discussed by Atmane & George (2002). For the present case, the positive fluxes are assimilated to the surface renewal events where portions of fluid with lower oxygen concentration ( $c < 0$ ) from the bulk are being transported towards the surface by upwelling eddy motions ( $w < 0$ ), stays long enough to allow a diffusion process to take place, and then these portions with yet higher oxygen concentration ( $c > 0$ ) return back to the bulk by downwelling eddy motions ( $w > 0$ ). When the diffusion time (at the surface or in the bulk) is too short for the fluid packages to exchange gases, the fluid packages get back to their initial positions without bringing or losing a significant amount of oxygen and its contribution to gas exchange is negative (upward flux).

### 5.5.2 Mean profile of turbulent mass flux

Chu & Jirka (1992) and Atmane & George (2002) attempted to measure the turbulent mass flux across the interface under similar turbulence conditions as the present study. Both Chu & Jirka (1992) and Atmane & George (2002), could not find any particular trend in the vertical  $\overline{cw}$  profiles. The reason might be the invasive measurement techniques which of course disturbed the actual mechanism of gas exchange within the limited boundary layer. Moreover, the measurements by Chu & Jirka (1992) did not perfectly coincide in space. In this study, the velocity and concentration fields could be measured simultaneously both in time and space with no interference from any sensor probes for the first

time. Indeed, a satisfactory results in revealing the contribution of the turbulent mass flux to the total mass flux could be obtained in the present study as discussed in the following.

The variation of the mean turbulent mass flux  $\overline{cw}$  with the depth is presented in Figure 5.28a. The profiles are obtained by temporally averaging and then spatially averaging the 900 instantaneous  $cw$  maps. The same plot is again given in Figure 5.28b, only here the depth is normalized with the measured boundary layer thickness  $\delta_e$ . The mean turbulent fluxes  $\overline{cw}$  are normalized by the total mean flux  $\overline{j}$  (as listed in Table 5.3) determined from the bulk measurements.

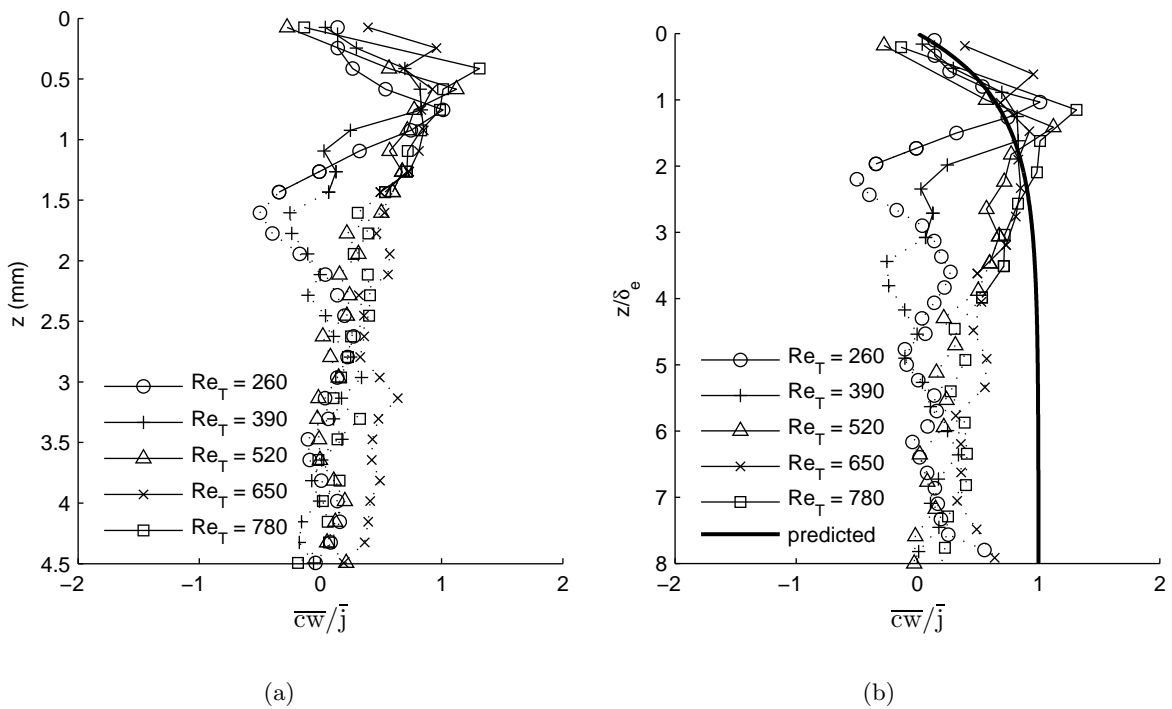


**Figure 5.28.** Variation of measured turbulent mass flux (a) with depth and (b) with normalized depth

In contrast to the results of Chu & Jirka (1992) and Atmane & George (2002), a particular trend can be inferred from the  $\overline{cw}$  profiles depicted in Figure 5.28. For all 5  $Re_T$ , the following description can be given. The normalized turbulent fluxes increase from around 0 at the interface to about 1 within approximately  $2\delta_e$ . This agrees with the fact that in the immediate vicinity of the water surface any turbulent transport should vanish and molecular diffusion is the dominant transfer mechanism. The measured turbulent flux is of the same order of the total mean flux determined from the bulk measurements ( $\overline{cw}/\overline{j} \approx 1$ ) and thus it could be shown that the contribution of the turbulent mass flux to the total gas flux is indeed significant.



Also shown in Figure 5.28b is the predicted turbulent flux distribution (indicated by the solid line) assuming a constant flux model in the surface region. The predicted profile is obtained by subtracting the molecular flux  $D\partial\bar{c}/\partial z$  from the total mean flux  $\bar{j}$  and  $\bar{c}$  is assumed to follow the exponential function proposed empirically by Chu & Jirka (1992) (Eq. 5.4).

In the surface region down to  $z/\delta_e \cong 2$ , the measured turbulent fluxes agrees well, both in trend and magnitude, with the predicted fluxes. With the exception for  $Re_T=260$  and  $390$ , the agreement is even good down to  $z/\delta_e \cong 3$ . This shows that the present measurement technique is indeed a reliable technique which successfully works within the very thin surface layer.

As it goes deeper into the bulk ( $z/\delta_e > 3$ ), the measured fluxes tend to decrease to zero. Of course, this should not be the case since pure turbulent flux (i.e.  $\overline{cw}/\bar{j} = 1$ ) should occur at all region below the surface layer as indicated by the the predicted fluxes which for  $z/\delta_e \geq 3$  remains constant at 1. The reason for this discrepancy seems to be the inaccuracy of the present measurement technique in the deeper bulk region, as far as the eddy-correlation method is concerned. In the almost fully mixed bulk region, the mean concentration fluctuations (i.e. root-mean square value of  $c$ ) tend to reach zero ( $c' \rightarrow 0$ ) while the mean velocity fluctuations reach large values ( $w' \rightarrow \infty$ ). The cross-product of the instantaneous fluctuations  $c$  and  $w$ , however, should still be something finite ( $cw \neq 0$ ). As described in Section 3.2.2, the present LIF illumination configuration is the optimal solution for the available laser power but it is not the most ideal configuration. With the present LIF illumination setup, the LIF accuracy becomes more obscure with further submergence into the bulk region. Thus, the detection of the minute fluctuations is impossible and so the accuracy of the present LIF technique in the bulk region might be too low for the eddy-correlation method. In Figure 5.28, the data points in the region where the results of the eddy-correlation are biased by the LIF inaccuracy are connected by dashed lines instead of solid lines.

## 5.6 Total mean flux

As mentioned previously, it is necessary to resolve in time and space both the molecular diffusive transport  $D\partial\bar{c}/\partial z$  and the turbulent mass transport  $\overline{cw}$  terms (see Eq. 2.5) in order to gain detailed fundamental understanding of the actual mechanism controlling the gas transfer process. The first term can be computed from the vertical concentration profiles  $\bar{c}(z)$  that was measured using the LIF technique (Figure 5.7) and the second term was directly measured using the eddy-correlation method. The results of the concentration profiles and the turbulent mass flux terms for the five different turbulent Reynolds

numbers have been discussed in Section 5.2.1 and 5.5.2 respectively. By combining these two information, the total mass flux can be obtained as shown in Figure 5.29.

The molecular diffusive transport term and the turbulent transport term are shown in Figure 5.29a and b, respectively. The sum of these two terms gives the total mean flux and is shown in Figure 5.29c. All values are normalized by the total mean flux  $\bar{j}$  (as listed in Table 5.3) determined from the bulk measurements. The profiles in Figure 5.29a clearly show that molecular diffusion is the dominant transfer mechanism in the immediate vicinity of the water surface and its contribution decreases with further submergence into the bulk.

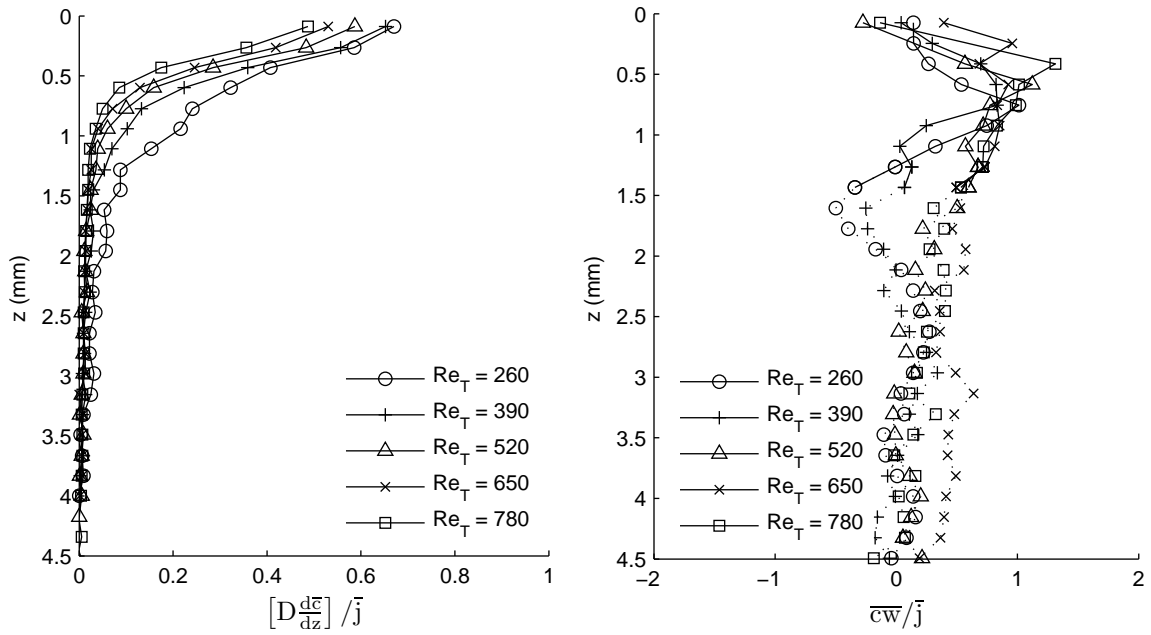
In the upper surface region, it could be shown in Figure 5.29c that the total mass flux measured using the eddy-correlation method agrees very well with the total flux  $\bar{j}$  determined from the bulk measurements (i.e.  $D\partial\bar{c}/\partial z + \overline{c\bar{w}} \approx \bar{j}$ ). This confirms that the present measurement technique enables direct quantification of the mass flux. As it goes deeper into the bulk, the total flux measured using the eddy-correlation method starts to deviate from the actual constant mass flux. The reason for the discrepancy is due to the poor accuracy of the measured  $\overline{c\bar{w}}$  in the deeper bulk region as has been discussed in Section 5.5.2. Again, the data points in the region where the results of the eddy-correlation are biased by the poor accuracy are connected by dashed lines instead of solid lines.

## 5.7 Spectra

It is interesting to estimate the power spectral density when studying turbulence properties. The power spectral density gives an indication of the energy distribution over various length or time scales. In this section, the near surface velocity spectra, concentration spectra and co-spectra of velocity and concentration fluctuations are discussed. Similar to the velocity spectral in the bulk region, the spectra are computed using the Welch method (see Section 4.4).

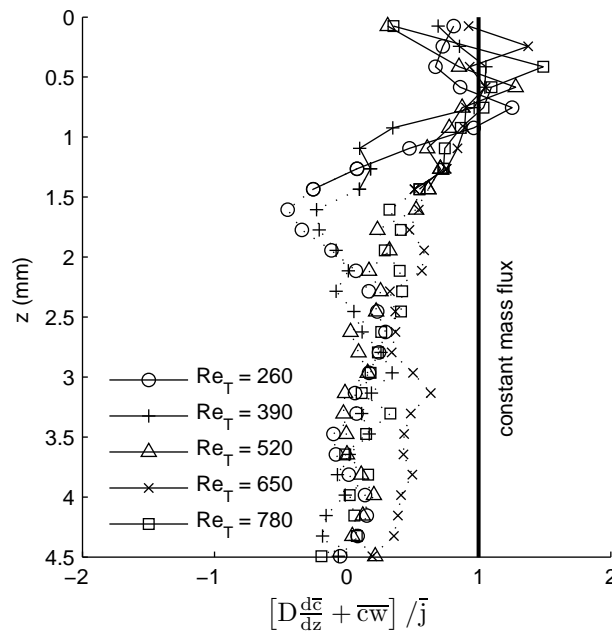
### 5.7.1 Spectra of near surface velocity fluctuation

The velocity spectra from the measurements performed near the interface are shown in Figures 5.30 to 5.34. The spectral density function of the horizontal and vertical velocity fluctuations  $u$  and  $w$  were given in Eqs. 4.14 and 4.15. In the figures, spectra at selected submergence levels  $z$  are shown. The spectra at each level were obtained in the same way as the spectra shown in Figures 4.10 and 4.11 (see Section 4.4). As mentioned in 4.4, the peaks at and around 1-2 Hz observed in the spectra of the velocity fluctuations are caused by the noise related to the grid oscillation frequencies and not to any turbulence production. In the figures, these biased regions are indicated by the dotted lines.



(a) measured diffusive transport term calculated from the vertical concentration profiles  $C(z)$  obtained using the LIF technique

(b) measured turbulent mass flux term obtained using the eddy-correlation method



(c) total mass flux obtained as the sum from (a) and (b)

**Figure 5.29.** Variation of measured molecular diffusive transport, turbulent mass flux and the resulting total mass flux with depth. All values are normalized with the absolute total mean flux  $\bar{j}$  (as listed in Table 5.3) determined from the bulk measurements.

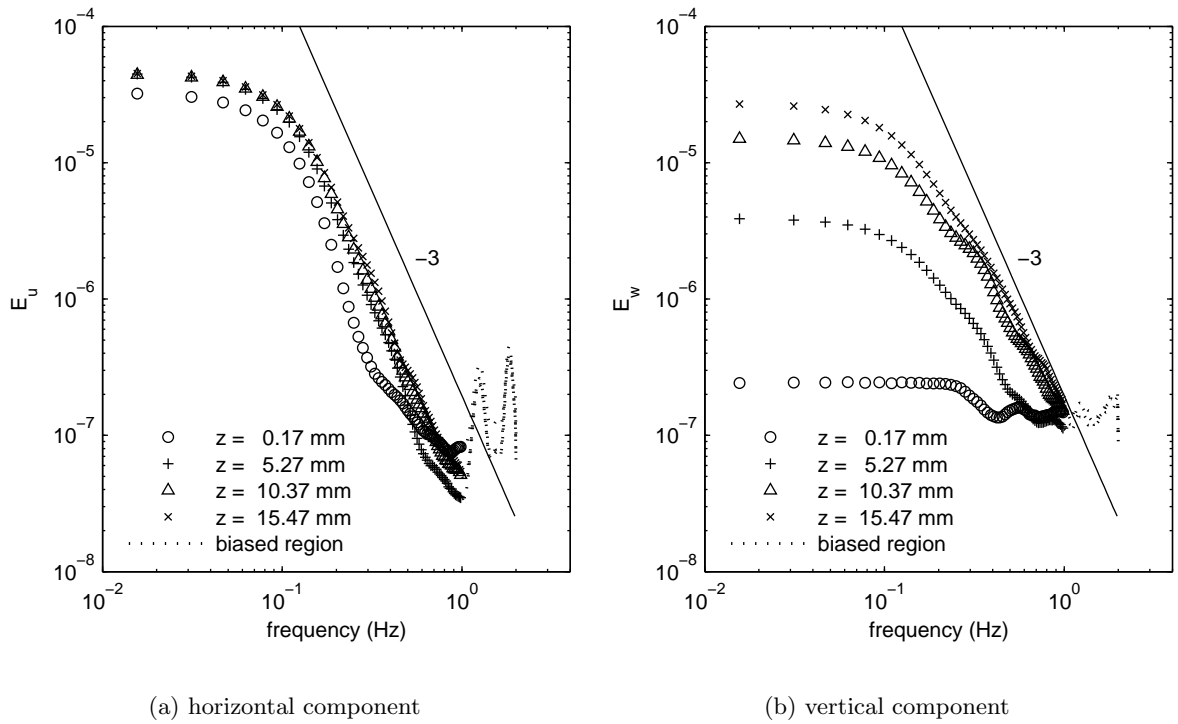


**Figure 5.30.** Spectra of near surface velocity fluctuation for  $Re_T = 260$ . (a) horizontal component; and (b) vertical component

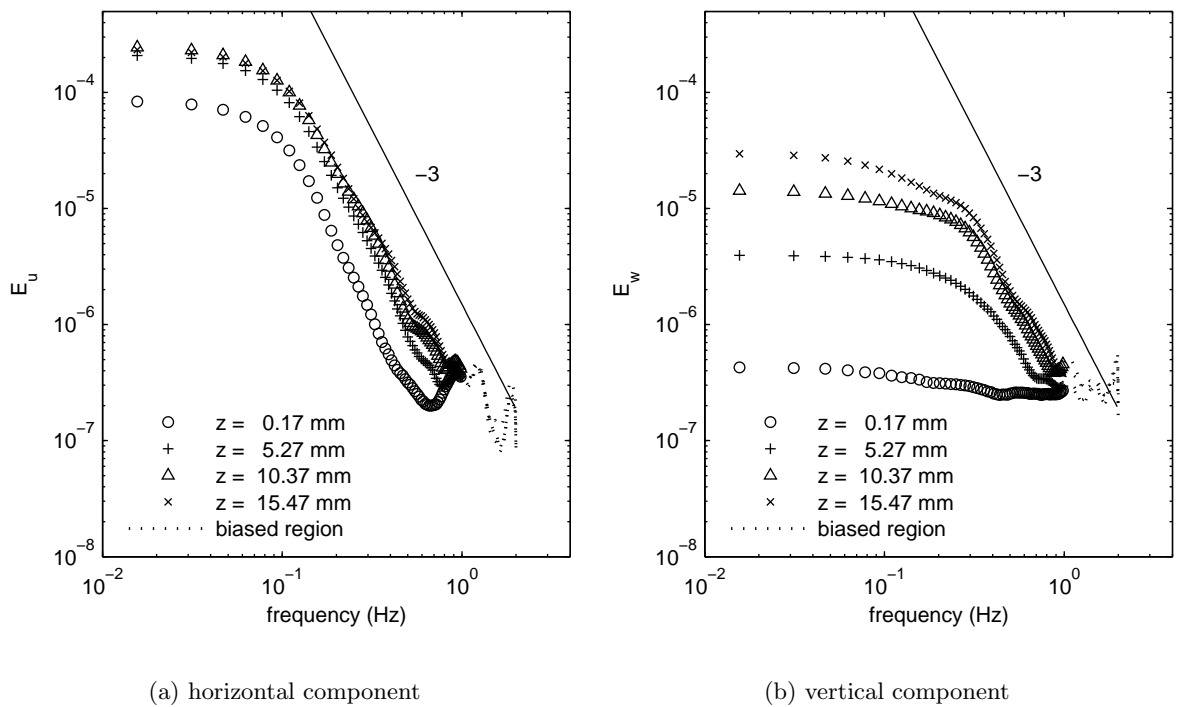


**Figure 5.31.** Spectra of near surface velocity fluctuation for  $Re_T = 390$ . (a) horizontal component; and (b) vertical component

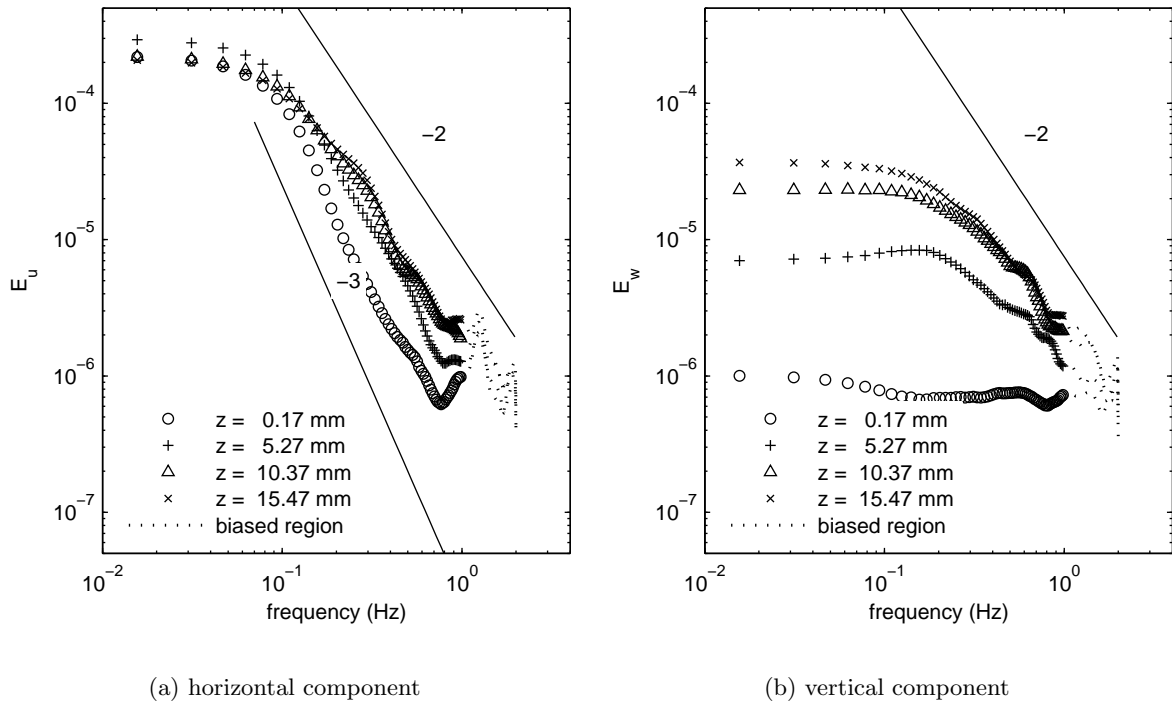


**Figure 5.32.** Spectra of near surface velocity fluctuation for  $Re_T = 520$ . (a) horizontal component; and (b) vertical component

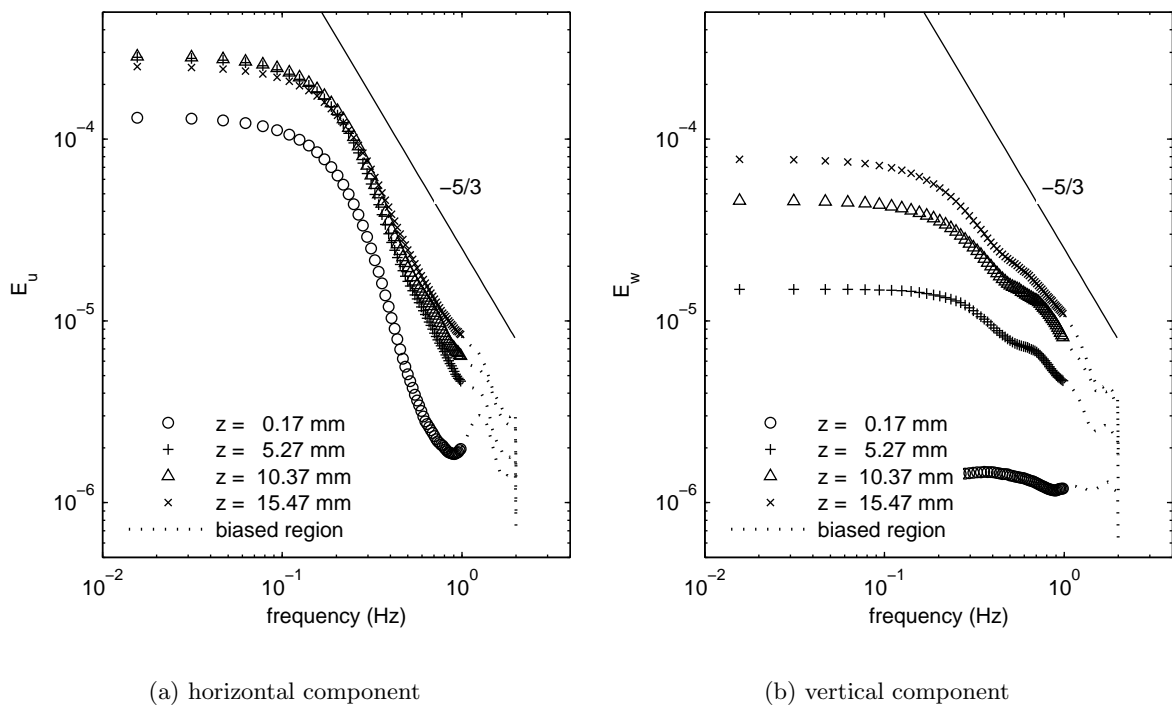


**Figure 5.33.** Spectra of near surface velocity fluctuation for  $Re_T = 650$ . (a) horizontal component; and (b) vertical component

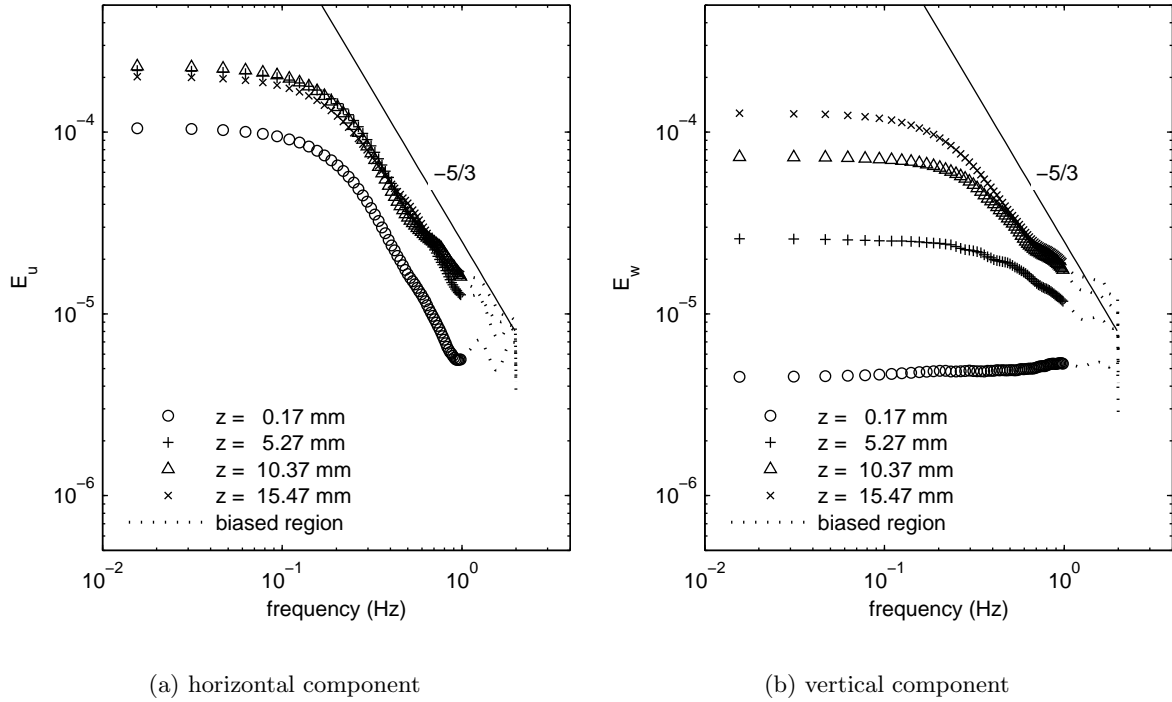


**Figure 5.34.** Spectra of near surface velocity fluctuation for  $Re_T = 780$ . (a) horizontal component; and (b) vertical component

Both the horizontal and vertical velocity spectra indicate that the turbulent energy increase with increasing submergence. The results are in line with the spectral analysis performed in the bulk region that has been discussed in Section 4.4. Compared to the velocity spectra in the bulk region (Figures 4.10 and 4.11), the spectra in the near surface region (Figures 5.30 and 5.34) are approximately a factor of  $10^2$  lower. This indicates that there is significant turbulence dissipation as the interface is approached. It can also be observed that the spectra in the bulk region (Figures 4.10 and 4.11) follow a slope of  $-5/3$ , while the spectra near the surface region (Figures 5.30 to 5.32) mostly follow a slope of  $-2$  or  $-3$ . The slope of  $-5/3$  is representative of the inertial subrange in three-dimensional turbulence, which is the case in the bulk region. However, this is not the case when the near surface region is approached. Here, the flow motion in the vertical direction is restricted and the flow becomes more two-dimensional. According to Batchelor (1969), the inertial subrange for two-dimensional turbulence flow is characterized by a proportionality to  $k^{-3}$  where  $k$  is the wavenumber. The  $-2$  slope may be related to the stretching of the turbulent eddies from 3D in the bulk to 2D as they approach the surface.

Part a and part b from Figures 5.30 to 5.34 depict the velocity fluctuation spectra of the horizontal and vertical components, respectively. Comparing the vertical velocity spectra with the horizontal spectra, one can observe the strong damping effect of the

water surface on the vertical fluctuation components. The turbulent energy of the vertical velocity fluctuations (Part b Figures 5.30 to 5.34) decreases rapidly towards the surface, within about 15 mm from the surface the energy decreases almost of the order of  $10^2$ . On the other hand, within the same submergence, the turbulent energy of the horizontal component stays at about the same order of magnitude. This shows that the vertical fluctuations components are inhibited by the surface, whereas the horizontal fluctuations may develop freely.

### 5.7.2 Spectra of concentration fluctuation

The concentration spectra  $E_c$  is estimated using the following relation

$$E_c(f) = \frac{1}{f_s} \int_{-\infty}^{+\infty} R_c(\tau) e^{-2\pi i f \tau / f_s} d\tau \quad (5.18)$$

with  $R_c$  denotes the auto-correlation of the concentration fluctuation and  $f_s$  is the sampling frequency (= 4 Hz in the present study).

The concentration spectra at selected submergence obtained for the different  $Re_T$  numbers are shown in Figures 5.35a to 5.35d. In contrast to the velocity spectra, the concentration spectra indicate that the concentration fluctuation decrease with submergence as expected.

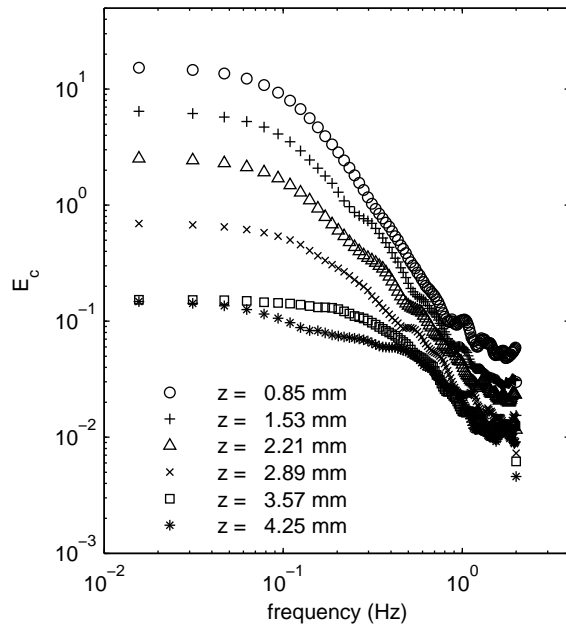
### 5.7.3 Co-spectra of velocity fluctuation and concentration fluctuation

The cross-spectral density function  $E_{cw}$  of the concentration fluctuation  $c$  and the vertical turbulent velocity  $w$  is related to the Fourier transformation of its cross-correlation function  $R_{cw}$

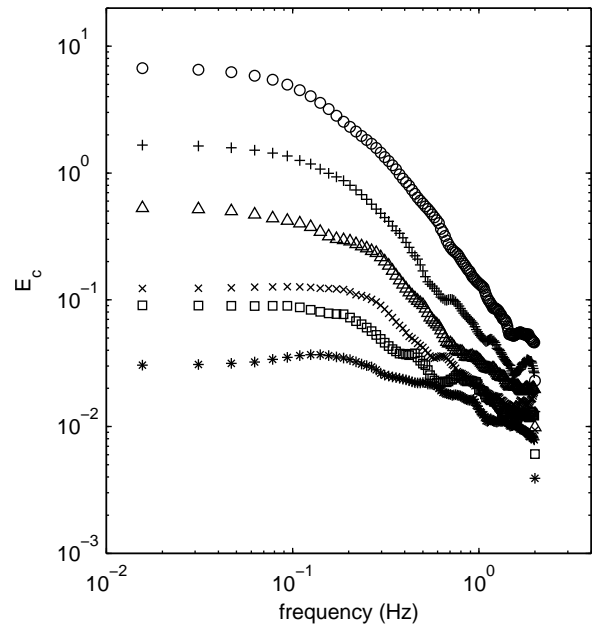
$$E_{cw}(f) = \frac{1}{f_s} \int_{-\infty}^{+\infty} R_{cw}(\tau) e^{-2\pi i f \tau / f_s} d\tau \quad (5.19)$$

The cross-spectral density illustrates how much the cross-product of the concentration fluctuation and the vertical velocity fluctuation (i.e. the turbulent mass flux) contributes to the gas transfer at certain frequency.

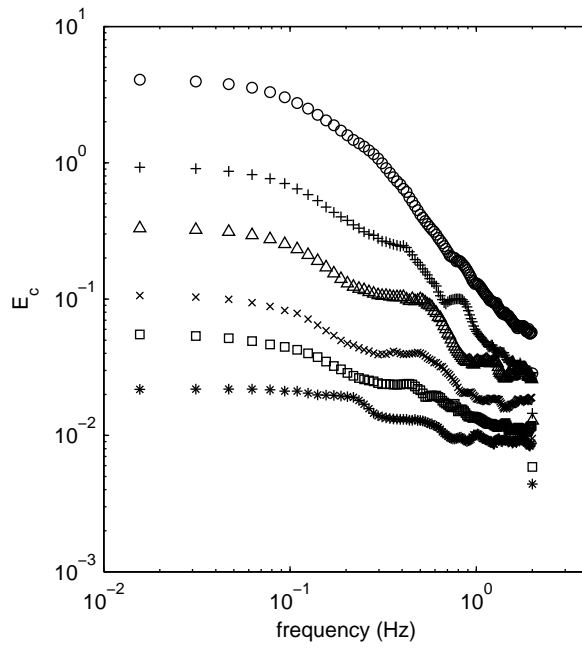
Chu & Jirka (1992) presented cross-spectral density in their paper. The co-spectra were unsatisfactory probably due to the measurement technique. They measured the velocity and concentration using a hot-film probe and a oxygen microprobe that were mounted on a rotating arm. The measurement points of the oxygen and velocity probe did not coincide exactly at one point and the data obtained for representing the spectra at certain submergence level were not measured simultaneously. These measurement problems were eliminated in the present study, however, the cross-spectra analysis here was limited to



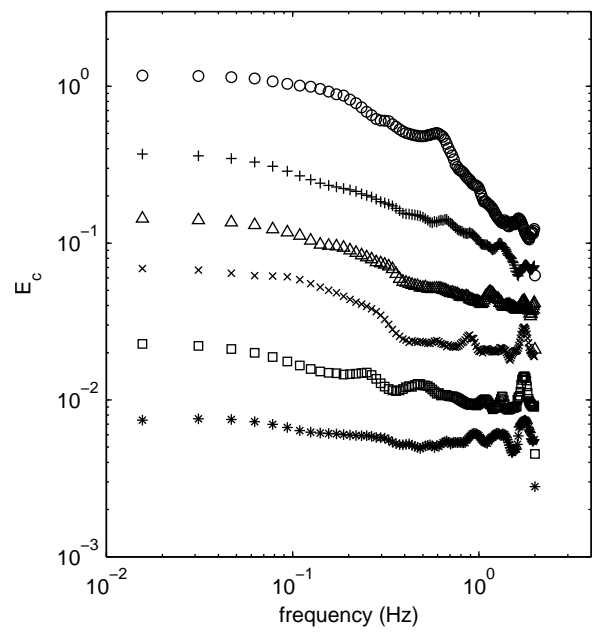
(a)  $Re_T = 260$



(b)  $Re_T = 380$



(c)  $Re_T = 520$



(d)  $Re_T = 780$

**Figure 5.35.** Spectra of concentration fluctuation  $c$



lower frequency range due to the restricted sampling frequency of 4 Hz. An attempt to interpret the co-spectra is given as follows.

The cross-spectral density functions  $E_{cw}$  at selected depth for the different  $Re_T$  numbers are shown in Figures 5.36a to 5.36d. In the deeper bulk region, the measured  $\overline{cw}$  are biased by the poor accuracy of the eddy-correlation method as discussed in Section 5.5.2. To differentiate the biased co-spectra from the reliable co-spectra, the biased co-spectra (i.e. the ones in the deeper region) are shaded light grey in the figures.

In all  $Re_T$  cases, the energy spectra decreases with deeper submergence. For the lower turbulence level measured ( $Re_T = 260$  and  $390$ ) depicted in Figure 5.36a and b, there is a decrease of energy from the lower frequencies (large eddy) to higher frequencies (small eddy). As mentioned in Section 4.4, the peaks at and around 1-2 Hz are caused by the noise related to the grid oscillation frequencies (indicated by the dashed lines). Ignoring the noise peaks, the co-spectra for  $Re_T = 260$  and  $390$  indicate that the gas flux is dominated by the large eddies. Such a clear trend could not be found in the co-spectra for the other cases with higher  $Re_T$  (Figures 5.36c to 5.36d). For the case with the highest  $Re_T = 780$ , there is a tendency that the higher frequencies (small eddy) are more dominant.

Chu & Jirka (1992) presented their co-spectra based on wave number and in normalized form so that direct comparison with the present results is difficult. Their spectral analysis was also unsatisfactory but they found an indication that spectra are relatively high at higher wave numbers (large eddies) so that they interpreted that the large eddies are more dominant in the gas transfer process. It should be noted that their measurement range ( $Re_T = 80$  to  $660$ ) was at the lower turbulence flow-regime, where according to Theofanus (1984) the large eddies dominate.

In order to observe more clearly how things are interacting over the present spectral range, the spectra of the vertical velocity fluctuations  $E_w$ , concentration fluctuations  $E_c$  and turbulent mass flux  $E_{cw}$  for all five  $Re_T$  at  $z/\delta_e \approx 1$  are summarized in Figure 5.37a, b and c, respectively. For all three spectra ( $E_w$ ,  $E_c$  and  $E_{cw}$ ), the figures clearly show that there is a decrease of energy as the turbulent Reynolds number  $Re_T$  decreases. In Figure 5.37c, it is shown that  $E_{cw}$  for the lower turbulence level measured ( $Re_T = 260$  and  $390$ ) behaves differently from  $E_{cw}$  for the other cases with higher  $Re_T$ . For the cases with  $Re_T < 390$ , the contribution of the turbulent mass flux  $cw$  associated with the lower frequencies (large eddies) are larger compared to that of the higher frequencies. On the other hand, there seems to be a tendency that the contribution of  $cw$  are larger in the higher frequency region for the other cases with higher  $Re_T$ . Again, this would suggest that the large eddies are more dominant in the gas transfer process for low  $Re_T$ , whereas the smaller eddies for high  $Re_T$ .

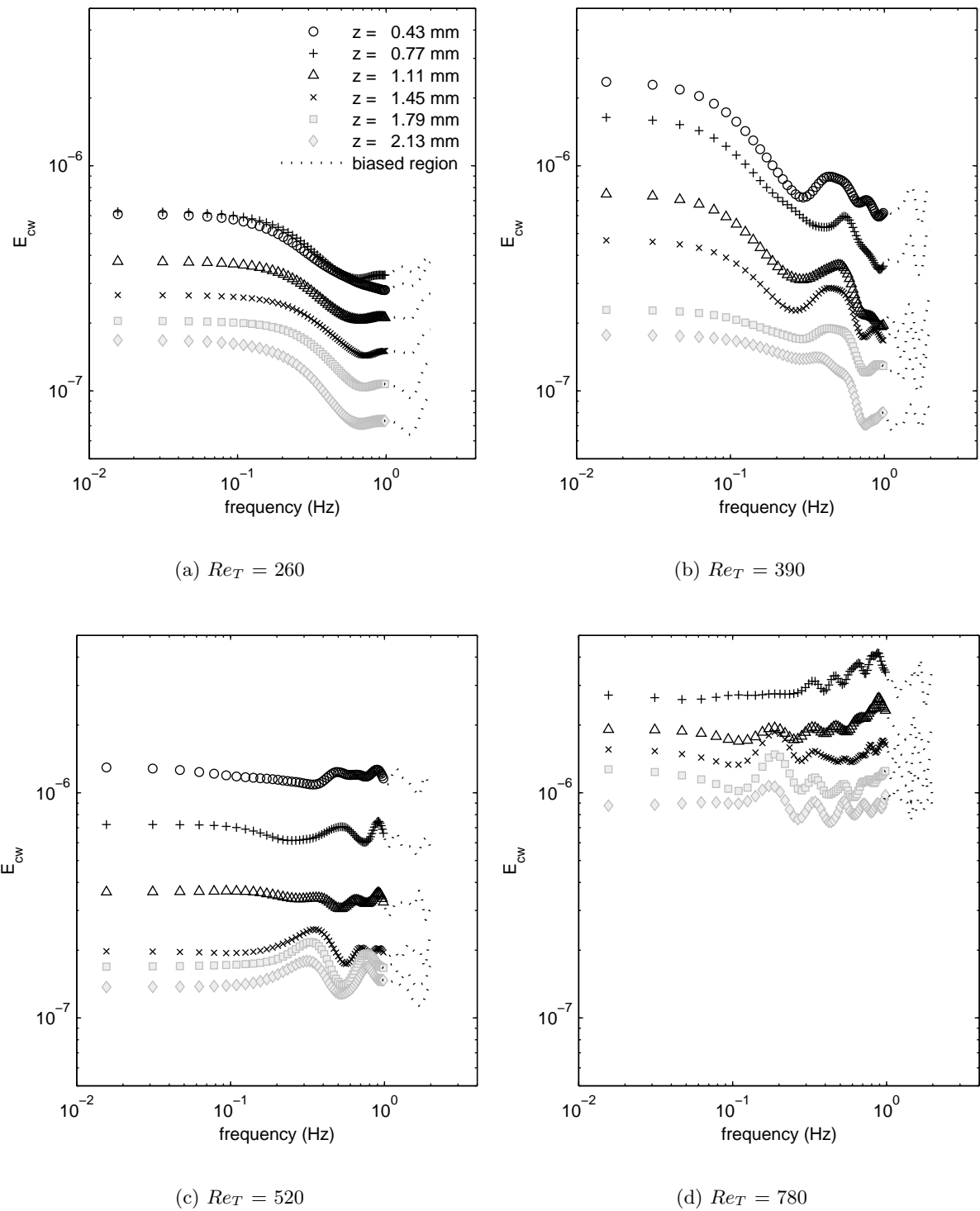
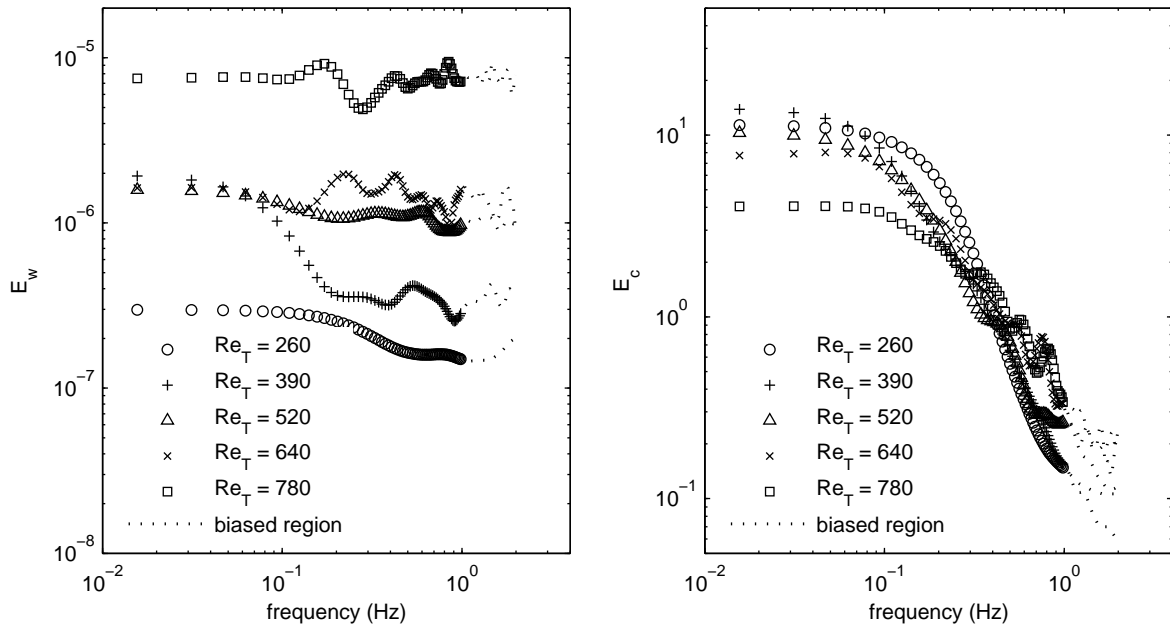
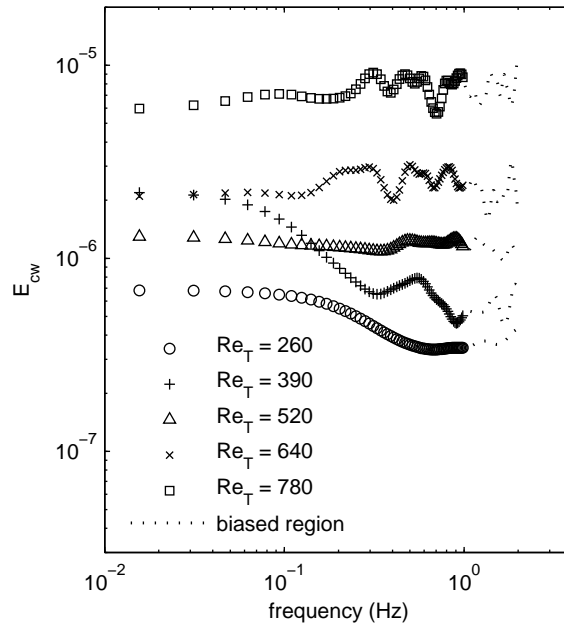


Figure 5.36. Spectra of turbulent mass flux  $cw$



(a) Spectra of vertical velocity fluctuations

(b) Spectra of concentration fluctuations



(c) Spectra of turbulent mass flux

**Figure 5.37.** Spectra of vertical velocity fluctuations, concentration fluctuations and turbulent mass flux at approximately  $z/\delta_e = 1$

## 5.8 Implications of the present results on mechanisms and models of gas transfer

Previous works that attempted to reveal the vertical turbulent mass flux  $\overline{cw}$  profiles directly below the interface under similar turbulence conditions as the present study ended up with unsatisfactory results. In contrast, the  $\overline{cw}$  profiles obtained in the present study clearly show a particular trend (Figure 5.28). With the information obtained by employing the simultaneous PIV-LIF technique, the mean turbulent mass flux term  $\overline{cw}$  and also the total mass flux across the air-water interface ( $D\partial\overline{c}/\partial z + \overline{cw}$ ) could be quantified directly for the first time. The apparent success in revealing these quantities shows that the present measurement technique successfully works within the very thin surface layer. It also suggests that the eddy-correlation (eddy-covariance) method can be considered as a reliable method for measuring the gas flux  $j$  across the interface directly given that appropriate measurement techniques are available. In the following, the implications of the present results on mechanisms and models of gas transfer are discussed.

### 5.8.1 Dominant eddy size

From the visual observations of the 2D instantaneous concentration maps, there is an indication that both eddy sizes play an important role in the gas transfer process. Further analysis was performed by presenting the mean concentration profiles in a normalized form  $((C - C_b)/(C_s - C_b))$  vs  $z/\delta_e$  as presented in Figure 5.17. The normalized profiles for all five measured turbulent Reynolds numbers ( $Re_T = 260$  to  $780$ ) fall between the two theoretical profiles predicted based on the surface renewal assumption and the small eddy assumption given by Jähne & Haussecker (1998). The major difference between the two theoretical profiles is that the profile predicted by the surface renewal model decreases much faster towards the concentration in the bulk region. The measured profiles clearly show the following tendency, as the turbulent Reynolds number increases, the decay of the concentration into the bulk is slower. The results indicate that the gas transfer is controlled by a spectrum of different eddy sizes. It seems that the gas transfer at different turbulence levels can be associated to a certain eddy size. At very high turbulence levels, the eddy sizes should be asymptotic to the Kolmogorov scales. Previous data from Chu & Jirka (1992) and Atmane & George (2002) agreed relatively well with the prediction given by the surface renewal model. It should be noted that their  $Re_T$  measurement range was mostly at the low turbulent flow-regime so that their results do not conflict with the present results. By fitting the data from Brown (1970) measured in an open channel, Theofanus (1984) obtained a quantitative relationship for his idea the so called two-flow regime model given in Eqs. 5.16 and 5.17. The relations were compared with the total

mean flux  $K_L$  obtained from the oxygen concentration measurements in the bulk (Figure 5.23). Besides the five  $K_L$  values obtained in the present study, the  $K_L$  values from Chu & Jirka (1992) and Sugihara & Tsumori (2005) are also included in the figure. The data generally follow the exponent dependency of -0.5 (large eddy model) and -0.25 (small eddy model) for  $Re_T < \approx 400$  and  $Re_T > \approx 400$ , respectively. The co-spectra of the velocity and concentration fluctuations (Figure 5.37c), which indicate how much the contribution of the turbulent mass flux to the total flux is, show that the co-spectra for the lower turbulence level measured ( $Re_T = 260$  and  $390$ ) behaves differently from the co-spectra for the other cases with higher  $Re_T$ . For the cases with  $Re_T < 390$ , the contribution of the turbulent mass flux  $cw$  associated with the lower frequencies (large eddies) are larger compared to that of the higher frequencies. Contrary, there seems to be a tendency that the contribution of  $cw$  are larger in the higher frequency region (small eddies) for the other cases with higher  $Re_T$ .

All these interrelated facts suggest that the gas transfer process is controlled by a spectrum of different eddy sizes and the gas transfer at different turbulence levels can be associated to certain eddy sizes. For very high turbulence levels the gas transfer should be asymptotic to the small eddy model, whereas for very low turbulence level to the large eddy model.

### 5.8.2 Contribution of the turbulent mass flux

The concave shape of the measured mean concentration profiles (Figure 5.7) indicate that the turbulent mass fluxes plays a role in the gas transfer process besides the molecular diffusion. Comparing the actual measured transfer velocity  $K_{L,t}$  with the estimated one based on the film model  $K_{L,\delta}$ , the value of  $K_{L,\delta}$  was always lower than  $K_{L,t}$ . The presence of turbulence obviously enhance the gas transfer process and its contribution might not be negligible. Here, the turbulent mass flux quantities were directly measured using the combined non-intrusive PIV-LIF technique. The profiles of the mean turbulent fluxes ( $\overline{cw}$ ) clearly show a particular trend for all five measured  $Re_T$  as shown in Figure 5.28. The contribution from the turbulent mass flux increases with further submergence from the interface and achieves a maximum value at around  $2\delta_e$ . The maximum value of the measured turbulent fluxes is of the same order of the total mean flux determined from the bulk measurements ( $\overline{cw}/\bar{j} \approx 1$ ) and thus it could be shown that the contribution of the turbulent mass flux to the total gas flux is indeed significant.

The fact that the contribution of the turbulent mass flux to the total mass flux is significant implies that the turbulent mass flux can not be neglected and should be taken into account when performing numerical models. These new results of turbulent mass

flux should aid as an excellent database in refining numerical models and developing more accurate models for the prediction of the transfer velocity.

## 6. Conclusions and Recommendations

### 6.1 Conclusions

The aim of this study is to gain improved fundamental understanding of the physical mechanisms that control the gas exchange process across the air-water interface. In particular, this study focuses on the oxygen absorption process in bottom-shear-induced turbulent environments (e.g. in natural streams under windless conditions). Currently, despite the intensive research efforts performed in the past, the actual physical mechanism controlling the gas transfer process is still unclear. The questions of the eddy size that contributes more to the gas transfer process as well as the contribution of the turbulent mass flux are still open. The improved knowledge of this process should aid further developments of more accurate models for the prediction of the transfer velocity. Therefore, detailed and reliable experimental data are required to address the open questions.

Performing detailed measurements near the interface is difficult due to the fact that for gases with low solubility (typical for gases that are environmentally important such as  $O_2$ ,  $N_2$ ,  $CO_2$ ,  $CO$ ), a boundary layer of ten to hundreds  $\mu m$  on the liquid side controls the gas transfer process. The application of intrusive measurement techniques disturbs the actual gas exchange process within the thin boundary layer. In this study, a combined PIV-LIF technique that enables simultaneous and spatially synoptic measurements of the two-dimensional velocity and concentration field was employed. These advanced techniques allowed for the first time direct quantification of the turbulent mass flux directly below the water surface with no interference from any sensor probes.

Before performing the gas transfer experiments in the grid-stirred tank, the turbulence characteristics generated by the oscillating grid was first evaluated. The evaluation was based on the flow-field measurements extending from near the grid up to 3 to 5 cm below the water surface with the aid of the PIV technique. The statistical turbulence characteristics obtained agreed well with previous works, i.e. the decay of the measured turbulence velocity follows the power law proposed by Hopfinger & Toly (1976) and the integral length scales increase linearly with distance from the grid. The spectral analysis indicate that the turbulence generated by the system is a full three-dimensional turbulent flow, at least in the bulk region. Consequently, it could be shown that the present grid-stirred tank system was a well-controlled system that could generate turbulence with

known reproducible scales and is therefore suitable for performing accurate gas transfer measurements.

The gas transfer measurements were performed with five varying turbulent Reynolds numbers  $Re_T$  ranging from 260 to 780. The gas transfer process in all series was induced by lowering the dissolved oxygen concentration of the water in the test tank. The results of the gas transfer measurements are summarized in the following.

The LIF-quenching method provided the possibility of visualizing planar concentration fields that was very useful in gaining more insight of the gas transfer mechanisms. Surface renewal events, in which large turbulent structures are peeling off portions of the surface layer with higher oxygen concentration and transporting these portions of fluid into the bulk region, could be visualized. In some sequences, small turbulence structure approaching the Kolmogorov scale were visible. The sequences show how the boundary layer is suppressed by turbulence structures impinging on the air-water interface leading to enhanced oxygen transfer rate. The visual observations suggest that the interaction of large and small structures is present, and it may play an important role in the transfer process.

The statistical results based on the concentration measurements can be summarized as follows. The mean boundary layer thickness decreases with higher turbulence intensities. The thickness is suppressed from about  $800 \mu\text{m}$  for  $Re_T = 260$  to  $300 \mu\text{m}$  for  $Re_T = 780$ . Excluding the case with  $Re_T = 260$ , the quantitative relationship between the outer diffusive sublayer and the boundary layer thickness proposed by Chu & Jirka (1992) agrees well for the present  $Re_T$  range. The normalized mean concentration profiles for all five measured turbulent Reynolds numbers ( $Re_T = 260$  to  $780$ ) fall between the two theoretical profiles based on the surface renewal assumption and the small eddy assumption given by Jähne & Haussecker (1998). The interpretation from the mean profiles support the idea proposed by Theofanus (1984) that the large eddies are dominant for low Reynolds numbers and the small eddies for high turbulent Reynolds numbers. The normalized  $c'$  profiles show that the fluctuations increase from smaller values near the interface to a maximum around the boundary layer thickness ( $z/\delta_e = 1$ ). The maximum peaks range between 0.15 to 0.2. After reaching a maximum, the  $c'$  values decrease with further submergence.

The statistical turbulence characteristics of the velocity near the interface show that the profiles agree well with the theoretical profile from Hunt & Graham, except in the region extremely near the water surface in which the measured profiles show the existence of a viscous boundary layer. The vertical fluctuations are better predicted by the Hunt & Graham theory as compared to the horizontal fluctuations. The deviation from the theory is due to the fact that the Hunt & Graham irrotational source theory does



not take into account several second order effects, including the existence of a viscous boundary layer.

Besides the simultaneous concentration and velocity measurements near the surface, oxygen concentration in the bulk were also performed in order to obtain the transfer velocity  $K_L$ . It was found that the transfer velocity calculated using the "film model" ( $K_{L,ze}$ ) is underestimated compared to the actually measured ( $K_{L,t}$ ) one. The presence of turbulence causes constant changes of the boundary layer thickness and also may transport portions of rich oxygen layers into the bulk which of course aid the gas transfer process. By adjusting the coefficients, the measured  $K_L$  values showed good agreement with the two flow-regime model proposed by Theofanus (1984). The large discrepancy between the coefficients that fitted best the present data and those suggested in previous works, could be due to the differences in the turbulent scales definitions between grid-stirred tank and open channel flow.

The simultaneous measurements of velocity and concentration allowed the quantification of the instantaneous fluxes. From these instantaneous data, upward (negative) and downward (positive) fluxes could be observed. A downward (positive) net flux for the mean turbulent mass flux  $\overline{c\bar{w}}$  should be expected and was indeed obtained as shown by the mean turbulent fluxes profiles. For the first time, a particular trend can be inferred from the measured  $\overline{c\bar{w}}$  profiles. The normalized turbulent fluxes increase from around 0 at the interface to about 1 within approximately  $2\delta_e$ . In the surface region down to  $z/\delta_e \cong 3$ , the measured turbulent fluxes agree well with the predicted fluxes. This shows that the present measurement technique is indeed a reliable technique which successfully works within the very thin surface layer. As it goes deeper into the bulk ( $z/\delta_e > 3$ ), the measured fluxes tend to decrease to zero, which should not be the case since pure turbulent flux should occur at all region below the surface layer. The reason seems to be the low accuracy of the present LIF technique in the deeper bulk region, as far as the eddy-correlation method is concerned. The measured turbulent flux is of the same order of the total mean flux determined from the bulk measurements ( $\overline{c\bar{w}}/\bar{j} \approx 1$ ) and thus it could be shown that the contribution of the turbulent mass flux to the total gas flux is indeed significant. These new experimental results is very useful for the refinement of numerical models.

The total mass flux obtained directly from the eddy-correlation measurements ( $D\partial\bar{c}/\partial z + \overline{c\bar{w}}$ ) was compared with the total flux determined from the bulk measurements ( $\bar{j}$ ). It could be shown that they were in very good agreement. This confirms that the present measurement technique enables direct quantification of the gas flux across the air-water interface.

Although, the spectral analysis was limited to a lower frequency range due to the restricted sampling frequency of 4 Hz, an attempt to interpret the spectra was still given. Both the horizontal and vertical velocity spectra clearly indicate that there is significant turbulence dissipation as the interface is approached. It can also be observed that the spectra in the bulk region follow a  $-5/3$  slope (representative of the inertial subrange in three-dimensional turbulence), while the spectra near the surface region mostly follow a  $-2$  slope (related to the stretching of the turbulent eddies from 3D in the bulk to 2D) or  $-3$  (the inertial subrange for two-dimensional turbulence flow). In contrast to the velocity spectra, the concentration spectra indicate that the concentration fluctuation decrease with submergence. The co-spectra in all five  $Re_T$  cases show that the energy spectra decreases with deeper submergence. It was observed that the co-spectra for the lower turbulence level measured ( $Re_T = 260$  and  $390$ ) behaves differently from the co-spectra for the other cases with higher  $Re_T$ . For  $Re_T$  lower than  $390$ , there is a decrease of energy from the lower frequencies (large eddy) to higher frequencies (small eddy), whereas for the cases with higher  $Re_T$ , there is a tendency that the contribution of  $cw$  are larger in the higher frequency region. Thus, the co-spectra indicate that the large eddies are more dominant in the gas transfer process for low  $Re_T$ , whereas the smaller eddies for high  $Re_T$ .

A discussion on the implications of the present results to the latest state of the art has been given. A general quantitative model that provides a precise prediction of the transfer velocity in different environmental conditions could not be obtained yet, but an improved fundamental knowledge of the actual mechanisms that controls the gas transfer process in a bottom-shear-induced turbulent environment was gained. From the interrelated interpretation of the obtained results, it could be shown that the gas transfer process is controlled by a spectrum of different eddy sizes and the gas transfer at different turbulence levels can be associated to certain eddy sizes. For very high turbulence levels the gas transfer should be asymptotic to the small eddy model, whereas for very low turbulence level to the large eddy model. The contribution of the turbulent mass flux to the total flux was shown to be significant. The vertical distribution of the mean turbulent fluxes could be quantified which is an essential database for the refinement of numerical models. These information should aid in developing more accurate models for the prediction of the transfer velocity which in practical engineering would help to improve the management of the quality of natural water resources as well as man-made reservoirs.

## 6.2 Recommendations for further studies

In this study, it has been shown that the contribution of the turbulent mass flux is significant to the total gas flux across the air-water interface. Therefore, future studies in the area of turbulence modelling should take into account the turbulent mass flux term  $cw$  when solving gas transfer problems. The new experimental results of  $cw$  obtained in the present study should be an excellent data base for refining detailed numerical modelling using Direct Numerical Simulation (DNS) or Large Eddy Simulation (LES).

The apparent success in revealing the turbulent mass flux quantities shows that the present measurement technique is a reliable method for the investigations of gas transfer processes across the air-water interface. Further studies should aim at adopting the present experimental setup and measurement technique to investigate the gas transfer process with other turbulence sources such as buoyant-convective-induced turbulence and surface-shear-induced turbulence. Implementing the present measurement technique with a much faster recording rate than the present one would be an advantage in order to cover the higher frequency domain so that more information could be obtained through the spectra analysis.

It would be interesting to adopt the present experimental setup and measurement technique to study the influence of varying degrees of surface contamination since the presence of surfactant also affects the gas transfer process. Another interesting task would be the implementation of the present method to study the heat transfer across the air-water interface.

# References

- Asher, W. E. & Pankow, J. (1986), 'The interaction of mechanically generated turbulence and interfacial films with a liquid phase controlled gas/liquid transport process', *Tellus: a bi-monthly journal of geophysics* **38B**, 305–318.
- Atmane, M. A. & George, J. (2002), 'Gas transfer across a zero-shear surface: a local approach', *Geophysical Monograph 127, Gas Transfer at Water Surfaces* pp. 255–259.
- Banerjee, S. (1990), 'Turbulence structure and transport mechanisms at interfaces', *Proc. 9th International Heat Transfer Conference* pp. 395–418.
- Banerjee, S., Rhodes, E. & Scott, D. S. (1968), 'Mass transfer to falling wavy liquid films in turbulent flow', *Industrial Engineering Chemicals Fundamentals* **7**, 22.
- Banner, M. & Peirson, W. L. (1995), 'An observational study of the aqueous surface layer structure beneath a wind-driven air-water interface', *Air-Water Gas Transfer, 3rd Int. Symp., Heidelberg, AEON Verlag*.
- Batchelor, G. (1969), 'Computation of the energy spectrum in homogeneous two-dimensional turbulence', *Physics of Fluids* **12**(12), 233–239.
- Broecker, W. S. & Peng, T.-H. (1982), 'Tracers in the sea', *Eldigio Press*.
- Brown, L. (1970), Oxygen transfer in open-channel flow, PhD thesis, University of Wisconsin.
- Brubaker, J. (1987), 'Similarity structure in the convective boundary layer of a lake', *Nature* **330**, 742–745.
- Brumley, B. (1984), 'Turbulence measurements near the free surface in stirred grid experiments', *Gas Transfer at Water Surfaces* pp. 83–92.
- Brumley, B. H. & Jirka, G. H. (1987), 'Near-surface turbulence in a grid-stirred tank', *Journal of Fluid Mechanics* (183), 236–263.
- Brumley, B. H. & Jirka, G. H. (1988), 'Air-water transfer of slightly soluble gases: turbulence interfacial processes and conceptual models', *Physico Chemical Hydrodynamics* **10**(3), 295–319.
- Brunk, B., Weber, S., Jensen, A., Jirka, G. & Lion, L. (1996), 'Modelling natural hydrodynamic systems with a differential-turbulence column', *Journal of Hydraulic Engineering* **122**(7), 373–380.
- Brutsaert, W. H. & Jirka, G. H. (1984), *Gas Transfer at Water Surfaces*, D. Reidel Publishing Co.
- Cheng, N. S. & Law, A. W.-K. (2001), 'Measurements of turbulence generated by oscillating grid', *Journal of Hydraulic Engineering* **127**, 201–208.
- Chu, C. & Jirka, G. (2003), 'Wind and stream flow induced reaeration', *Journal of Environmental Engineering* **129**(12), 1129–1136.
- Chu, C. R. (1990), 'Near surface turbulent velocity and oxygen concentration measurements in a grid-stirred tank', *MSc Thesis, Cornell University* p. 131.
- Chu, C. R. (1993), Experiments on gas transfer and turbulence structure in free surface flows with combined wind / bottom shear, PhD thesis, Cornell University.
- Chu, C. R. & Jirka, G. H. (1992), 'Turbulent gas flux measurements below the air-water interface of a grid-stirred tank', *International Journal of Heat Mass Transfer* **35**(8), 1957–1968.
- Churchill, M. (1961), 'Effect of water temperature on stream reaeration', *Journal of the Sanitary Engineering Division* **5**(87), 59–71.
- Cohen, Y. (1983), 'Mass transfer across a sheared wavy air-water interface', *International Journal of Heat and Mass Transfer* **26**, 1289–1297.
- Cromwell, T. (1960), 'Pycnoclines created by mixing in an aquarium tank', *Journal of Marine Research* **18**, 73.
- Danckwerts, P. V. (1951), 'Significance of liquid-film coefficients in gas absorption', *Industrial and Engineering Chemistry* **43**, 1460–1467.
- Davies, J. T. (1972), 'Turbulence phenomena', *Academic Press, N.Y.*

- Deadorff, J., Willis, G. & Lilly, D. (1969), 'Laboratory investigation of non-steady penetrative convection', *Journal of Fluid Mechanics* **35**(1), 7–31.
- Donelan, M. & Wanninkhof, R. (2002), 'Gas transfer at water surfaces-concepts and issues', *Geophysical Monograph 127, Gas Transfer at Water Surfaces* pp. 1–10.
- Duke, S. R. & Hanratty, T. J. (1995), 'Measurement of the concentration field resulting from oxygen absorption at a wavy air-water interface', *Air-Water Gas Transfer : 3rd International Symposium on Air-Water Gas Transfer* pp. 627–635.
- Eloubaidy, A. F. (1969), Wind waves and the reaeration coefficient in open channel flow, PhD thesis, Colorado State Univ. Fort Collins.
- Eloubaidy, A. F. & Plate, E. (1972), 'Wind shear turbulence and reaeration coefficient', *Journal of Hydraulics Division, ASCE* **98**(HY1), 153–170.
- Eugster, W., Kling, G., Jonas, T., McFadden, J., Wüest, A., MacIntyre, S. & Chapin, F. (2003), 'CO<sub>2</sub> exchange between air and water in an arctic alaskan and midlatitude swiss lake: Importance of convective mixing', *J. Geophysical Research* **108**(D12).
- Fortescue, G. E. & Pearson, J. R. (1967), 'On gas absorption into a turbulent liquid', *Chemical Engineering Science* **22**, 187–216.
- Francey, R. J. & Garratt, J. R. (1978), 'Eddy flux measurements over the ocean and related transfer coefficients', *Boundary Layer Meteorology* **14**, 153–166.
- Frexes, P., Jirka, G. H. & Brutsaert, W. (1984), 'Examination of recent field data on stream reaeration', *Journal Environmental Engineering, ASCE* **110**(6).
- George, J., Caussade, B. & Masbernat, L. (1995), 'Conceptual modelling of interfacial gas-liquid mass transfer', *Proceedings 3rd International Symposium on Air-Water Gas Transfer* pp. 69–76.
- Grisenti, M. & George, J. (1991), 'Hydrodynamics and mass transfer in a jet-agitated vessel', *Air-Water Mass Transfer: Selected Papers 2nd Int. Symp. Gas Transfer at Water Surfaces* .
- Gulliver, J. (1990), 'Introduction to air-water mass transfer', *Air-Water Mass Transfer : 2nd International Symposium on Air-Water Gas Transfer* pp. 1–7.
- Gulliver, J. S. & Halverson, M. J. (1989), 'Air-water gas transfer in open channels', *Water Resources Research* **25**(8), 1783–1793.
- Harriott, P. (1962), 'A random eddy modification of the penetration theory', *Chemical Engineering Science* **17**, 149–154.
- Herlina & Jirka, G. H. (2004), 'Application of lif to investigate gas transfer near the air-water interface in a grid-stirred tank', *Experiments in Fluids* **37**(3).
- Higbie, R. (1935), 'The rate of absorption of a pure gas into a still liquid during short periods of exposure', *AIChE Transactions* **31**, 365–390.
- Hopfinger, E. & Toly, J. (1976), 'Spatially decaying turbulence and its relation to mixing across density interfaces', *Journal of Fluid Mechanics* **78**, 155–175.
- Hunt, J. C. R. (1984), 'Turbulent structure and turbulent diffusion near gas-liquid interfaces', *Gas Transfer at Water Surfaces* pp. 67–82.
- Hunt, J. C. R. & Graham, J. M. R. (1978), 'Free-stream turbulence near plane boundaries', *Journal of Fluid Mechanics* **84**, 209–235.
- Imberger, J. (1985), 'The diurnal mixed layer', *Limnol. Oceanogr.* **30**, 737–770.
- Jähne, B. & Haussecker, H. (1998), 'Air-water gas exchange', *Annual Review of Fluid Mechanics* **30**, 443–468.
- Jähne, B., Münnich, K. O., Bösinger, R., Dutzi, A., Huber, W. & Libner, P. (1987), 'On the parameters influencing air-water gas exchange', *Journal Geophysical Research* **92C2**, 1937–1949.
- Jähne, B., Münnich, K. O. & Siegenthaler, U. (1979), 'Measurement of gas exchange and momentum transfer in a circular wind-water tunnel', *Tellus* **31**, 321–329.
- Jirka, G. H. (1991), 'Gas transfer at the air/water interface', *Proceedings International Symposium on Environmental Hydraulics* .
- Jirka, G. H. (1994), 'Gasaustausch an der grenzfläche zwischen luft und wasser', *Österreichische Ingenieur- und Architekten-Zeitschrift* **139**, 407–417.
- Jirka, G. H. & Brutsaert, W. (1984), 'Measurements of wind effects in water-side controlled gas exchange in natural rivers', *Gas Transfer at Water Surfaces, 1st Int. Symposium Ithaca Reidel Publishing Co* .
- Jirka, G. H. & Chu, C.-R. (1993), 'Surface gas transfer and turbulence structure in combined wind/ bottom shear flow regimes', *Proceedings International Conference on Hydrosience and Engineering* .

- Jirka, G. H. & Ho, A. H. W. (1990), 'Measurements of gas concentration fluctuations at water surface', *Journal of Hydraulic Engineering* **116**(6), 835–847.
- Jonas, T., Stips, A., Eugster, W. & Wüest, A. (2003), 'Observations of a quasi shear-free lacustrine convective boundary layer : Stratification and its implications on turbulence', *J. Geophysical Research* **108**(C10).
- Jones, E. P. & Smith, S. D. (1977), 'A first measurement of sea-air co<sub>2</sub> flux by eddy correlation', *J. Geophysical Research* **82**, 5990–5992.
- Kastaros, K., Liu, W., Businger, J. & Tillman, J. (1977), 'Heat transfer and thermal structure in the interfacial boundary layer measured in an open tank of water in turbulent free convection', *Journal of Fluid Mechanics* **83**, 311–335.
- Kerman, B. R. (1984), 'A model of interfacial gas transfer for all well-roughened sea', *Journal of Geophysical Research* **89D**, 1439–1446.
- Kitaigorodskii, S. A. & (1984), 'On the fluid dynamical theory of turbulent gas transfer across an air-sea interface in the presence of breaking wind-waves', *Journal of Physical Oceanography* **4**, 960–972.
- Kumar, S., Gupta, R. & Banerjee, S. (1998), 'An experimental investigation of the characteristics of free-surface turbulence in channel flow', *Physics of fluids* **10**(2), 437–456.
- Kunugi, T. & Satake, S.-i. (2002), 'Direct numerical simulation of turbulent free surface flow with carbon-dioxide gas absorption', *Geophysical Monograph 127, Gas Transfer at Water Surfaces* pp. 77–82.
- Lamont, J. C. & Scott, D. S. (1970), 'An eddy cell model of mass transfer into the surface of a turbulent liquid', *AIChE Journal* **16**, 513–519.
- Lau, Y. (1975), 'An experimental investigation of reaeration in open channel flow', *Prog. Water Technol.* **7**(3/4), 519.
- Law, A. W. K. & Herlina (2002), 'An experimental study on turbulent circular wall jets', *Journal of Hydraulic Engineering* **128**(2), 161–174.
- Law, A. W. K. & Wang, H. W. (2000), 'Measurements of mixing processes using combined piv and plif', *Journal of Experimental Thermal and Fluid Sciences* **22**(3-4), 213–229.
- Lee, M. (2002), 'Visualization of oxygen transfer across the air-water interface using a fluorescence oxygen visualization method', *Water Research* **36**, 2140–2146.
- Lee, Y. (1977), Microprobe method for studying gas-liquid oxygen transfer in various surfactant systems, PhD thesis, Purdue University.
- Lewis, W. K. & Whitman, W. (1924), 'Principles of gas absorption', *Industrial and Engineering Chemistry* **16**.
- Liss, P. S. (1983), 'Gas transfer and geochemical implications', *Air-Sea Exchange of Gases and Particles* .
- Liss, P. S. & Slater, P. G. (1974), 'Flux of gases across the air-sea interface', *Nature* **247**, 181–184.
- Lyn, D. (1997), 'A piv study of an oscillating grid flow', *Experimental and Numerical Flow Visualization and Laser Anemometry, American Society of Mechanical Engineers, Fluids Engineering Division, ASME, New York* **13**.
- MacIntyre, S., Flynn, K., Jellison, R. & Romero, J. (1999), 'Boundary mixing and nutrient fluxes in mono lake, california', *Limnology and Oceanography* **44**, 512–529.
- Marple Jr., S. (1987), *Digital Spectral Analysis*, Prentice-Hall.
- Mattingly, G. E. (1977), 'Experimental study of wind effects on reaeration', *J. Hydraulics Div. ASCE* **103**(3), 311–323.
- McCready, M., Vassiliadou, E. & Hanratty, T. (1986), 'Computer-simulation of turbulent mass-transfer at a mobile interface', *AIChE Journal: Chemical Engineering Research and Development* **32**(7), 1108–1115.
- McDougal, T. (1979), 'Measurements of turbulence in a zero-mean-shear mixed layer', *Journal of Fluid Mechanics* **94**, 409–431.
- McGillis, W. R., Edson, J. B., Hare, J. E. & Fairall, C. W. (2001), 'Direct covariance air-sea co<sub>2</sub> fluxes', *J. Geophysical Research* **106**(8), 16729–16746.
- McKenna, S. P. & McGillis, W. (2002), 'Surface divergence and air-water gas transfer', *Geophysical Monograph 127, Gas Transfer at Water Surfaces* pp. 129–134.
- Merlivat, L. & Memery, L. (1983), 'Gas exchange across air-water interface: experimental results and modeling of bubble contribution to transfer', *Journal of Geophysical Research* **88C**, 707–724.
- Moog, D. B. & Jirka, G. H. (1995a), 'Macro-roughness effects on stream reaeration', *Air-Water Gas Transfer* pp. 89–99.
- Moog, D. B. & Jirka, G. H. (1995b), 'Tilting wind-water tunnel', *Air-Water Gas Transfer* pp. 495–498.

- Moog, D. B. & Jirka, G. H. (1998), 'Analysis of reaeration equations using mean multiplicative error', *Journal Environmental Engineering* **124**, 104–110.
- Moog, D. B. & Jirka, G. H. (1999b), 'Stream reaeration in non-uniform channel flow: Macro roughness enhancement', *Journal Hydraulic Engineering* **125**(1), 11–16.
- Moog, D. B. & Jirka, G. H. (2002), 'Air-water gas transfer in uniform flows with large gravel-bed roughness', *Geophysical Monograph 127, Gas Transfer at Water Surfaces* pp. 371–376.
- Münsterer, T. (1996), 'LIF investigation of the mechanisms controlling air-water mass transfer at a free interface', *PhD. Thesis, Universität Heidelberg*.
- Münsterer, T. & Jähne, B. (1998), 'LIF measurement of concentration profiles in the aqueous mass boundary layer', *Experiments in Fluids* **25**, 190–196.
- Münsterer, T., Mayer, H. & Jähne, B. (1995), 'Dual-tracer measurements of concentration profiles in the aqueous mass boundary layer', *Air-Water Gas Transfer : 3rd International Symposium on Air-Water Gas Transfer* pp. 637–648.
- Nakayama, T. (2000), 'Turbulence and coherent structures across air-water interface and relationship with gas transfer', *PhD Dissertation; Kyoto University*.
- Nezu, I. & Nakagawa, H. (1993), *Turbulence in Open Channel Flows*, Balkema, Rotterdam.
- O'Connor, D. & Dobbins, W. (1956), 'The mechanism of reaeration in natural streams', *Journal of Sanitary Engineering, ASCE* **82**(SA6), 1115–1140.
- O'Connor, D. J. (1983), 'Wind effects on gas-liquid transfer coefficients', *Journal of Environmental Engineering* **109**, 731–752.
- Orlins, J. & Gulliver, J. (2002), 'Measurements of free surface turbulence', *Geophysical Monograph 127, Gas Transfer at Water Surfaces* pp. 247–253.
- Peirson, W. L. & (1997), 'Measurement of surface velocities and shear at a wavy air-water inter-face using particle image veloci-metry', *Experiments in Fluids* **23**, 427–437.
- Plate, E. J. & Friedrich, R. (1984), 'Reaeration of open channel flow', *Gas Transfer at Air-Water Interfaces* pp. 333–346.
- Prinos, P., Atmane, M. & George, J. (1995), 'Gas flux measurements and modelling below an air-water interface', *Proceedings 3rd International Symposium on Air-Water Gas Transfer* pp. 49–57.
- Raffel, M., Willert, C. & Kompenhans, J. (1998), *Particle Image Velocimetry*, Springer Verlag, Berlin.
- Rashidi, M., Hetsroni, G. & Banerjee, S. (1991), 'Mechanisms of heat and mass transport at gas-liquid interfaces', *Int. J. Heat and Mass Transfer* **34**(7), 1799–810.
- Roy, A., Buffin-Bélanger, T., Lamarre, H. & Kirkbride, A. (2004), 'Size, shape and dynamics of large-scale turbulent flow structures in a gravel-bed river', *J. Fluid Mech.* **500**, 1–27.
- Sander, J., Simon, A., Jonas, T. & Wüest, A. (2000), 'Surface turbulence in natural waters: A comparison of large eddy simula-tions with microstructure observations', *Journal of Geophysical Research* **105**(1), 1195–1208.
- Schladow, S., Lee, M., Hürzeler, B. & Kelly, P. (2002), 'Oxygen transfer across the air-water interface by natural convection in lakes', *Limnology and Oceanography* **47**(5), 1394–1404.
- Shay, T. & Gregg, M. (1984), 'Turbulence in an oceanic convective mixed layer', *Nature* **310**(5975), 282–285.
- Shay, T. J. & Gregg, M. (1986), 'Convectively driven turbulent mixing in the upper ocean', *J. Physical Oceanog-raphy* **16**(11), 1777–1798.
- Soloviev, A. & Schlüssel, P. (1994), 'Parameterization of the cool skin of the ocean and of the air-ocean gas transfer on the basis of modeling surface renewal', *Journal of Physical Oceanography* **24**(6), 1339–1346.
- Son, J. & Hanratty, T. (1967), 'Limiting relation for the eddy diffusivity close to the a wall', *AIChE Journal* **13**, 689.
- Sugihara, Y. & Tsumori, H. (2005), 'Surface-renewal eddies at the air-water interface in oscillating-grid turbu-lence', *Environmental Hydraulics and Sustainable Water Management-Lee and Lam(eds)* pp. 199–205.
- Takehara, K. & Etoh, G. (2002), 'A direct visualization method of co2 gas transfer at water surface driven by wind waves', *Geophysical Monograph 127, Gas Transfer at Water Surfaces* pp. 89–95.
- Tamburrino, A. & Gulliver, J. (2002), 'Free-surface turbulence and mass transfer in a channel flow', *AIChE Journal* **48**(12), 2732–2743.
- Tamburrino, A. & Soval, F. (1999), 'Computation of the gas transfer coefficient across an air-water interface using synthetically generated data', *Proceedings XXVIII IAHR Congress Graz*.
- Tennekes, H. & Lumley, J. (1972), *A First Course in Turbulence*, MIT Press, Cambridge.

- Thackston, E. L. & Krenkel, P. A. (1969), 'Reaeration prediction in natural streams', *J. Sanitary Engrg. Div. Proc. ASCE* **95(SA1)**, 65–93.
- Theofanus, T. G. (1984), 'Conceptual models of gas exchange', *Gas transfer at air-water surfaces. Reidel*. pp. 271–281.
- Theofanus, T. G., Houze, R. N. & Brumfield, L. K. (1976), 'Turbulent mass transfer at free, gas liquid interfaces with applications to open channel, bubble and jet flows', *International Journal of Heat and Mass Transfer* **19**.
- Thompson, S. M. & Turner, J. S. (1975), 'Mixing across an interface due to turbulence generated by an oscillating grid', *Journal of Fluid Mechanics* **67**, 349–368.
- Turner, J. S. (1968), 'The influence of molecular diffusivity on turbulent entrainment across a density interface', *Journal of Fluid Mechanics* **23**, 639.
- Vaughan, W. M. & Weber, G. (1970), 'Oxygen quenching of pyrenebutyric acid fluorescence in water, a dynamic probe of the microenvironment.', *Biochemistry* **9**, 464–473.
- Weitbrecht, V. (2004), 'Influence of dead-water zones on the dispersive mass transport in rivers', *Doctoral Thesis, Institute for Hydromechanics, University Press ISBN 3-937300-07-4*.
- Weitbrecht, V., Kühn, G. & Jirka, G. H. (2002), 'Large scale piv-measurements at the surface of shallow water flows', *Flow Measurement and Instrumentation* **13**, 237–245.
- Welch, P. (1967), 'The use of fast fourier transform for the estimation of power spectra method based on time averaging over short modified periodograms', *IEEE Trans. Electroacoust.* **AU-15**, 70–73.
- Westerweel, J. (2000), 'Theoretical analysis of the measurement precision in particle image velocimetry', *Experiments in Fluids* **29**(7), 3–12.
- Wolff, L. M. & Hanratty, T. J. (1994), 'Instantaneous concentration profiles of oxygen accompanying absorption in a stratified flow', *Experiments in Fluids* **16**, 385–392.
- Wolff, L. M., Liu, Z. C. & Hanratty, T. J. (1990), 'A fluorescence technique to measure concentration gradients near an interface', *Proceedings 2nd International Symposium on Gas Transfer at Water Surfaces* pp. 210–218.
- Woodrow, P. T. & Duke, S. R. (2001), 'Laser-induced fluorescence studies of oxygen transfer across unshered flat and wavy air-water interfaces', *Industrial and Engineering Chemistry Research* **40**, 1985–1995.
- Woodrow, P. T. & Duke, S. R. (2002), 'LIF measurements of oxygen concentration gradients along flat and wavy air-water interfaces', *Geophysical Monograph 127, Gas Transfer at Water Surfaces* pp. 83–88.
- Yotsukura, N., Stedfast, D. A. & Jirka, G. H. (1984), 'An assessment of steady state propane gas tracer method for reaeration', *The Chenango River New York US Geological Survey Water Resources Investigations Report 84* p. 4368.



# Lebenslauf

## Persönliches

Name: Herlina  
Geburtsdatum: 8. März 1975  
Geburtsort: Frankfurt  
Nationalität: Indonesisch  
Familienstand: verheiratet, Mutter von ein Sohn und eine Tochter

## Schule, Ausbildung und Beruf

1981-1983: Grundschule Uhlandschule in Frankfurt  
1983-1984: Grundschule SDN VI Teladan in Tangerang, Indonesien  
1984-1987: Grundschule SDN Cipete Utara 03 Pagi in Jakarta, Indonesien  
1987-1990: Mittelschule SMPN 68 in Jakarta, Indonesien  
1990-1993: Oberschule SMAN 34 in Jakarta, Indonesien  
1993-1997: Studium des Bauingenieurwesens an der University of Indonesia in Jakarta, Indonesien mit dem Abschluss Sarjana Teknik (Bachelor of Engineering)  
03/1998 - 05/1998: Ingenieur im Bereich Wasserbau am Ingenieurbüro PT. Tata Guna Patria Engineering Consultant, Jakarta  
06/1998 - 06/2000: Master Studium des Bauingenieurwesens an der Nanyang Technological University in Singapore, Fachrichtung Environmental and Water Resources Engineering mit dem Abschluss Master of Engineering  
seit 10/2000: Wissenschaftliche Angestellte am Institut für Hydromechanik der Universität Karlsruhe